Introduction and application of a new blind source separation method for extended sources in X-ray astronomy

Adrien Picquenot

université
PARIS-SACLAY

Introduction and application of a new blind source separation method for extended sources in X-ray astronomy

Thèse de doctorat de l'Université Paris-Saclay

École doctorale n° 127 : Astronomie et Astrophysique d'Ile-de-France (AAIF)
Spécialité de doctorat: Astronomie et Astrophysique
Unité de recherche: Université Paris-Saclay, CNRS, CEA, Astrophysique, Instrumentation et Modélisation de Paris-Saclay, 91191, Gif-sur-Yvette, France
Référent: Faculté des sciences d'Orsay

Thèse présentée et soutenue à Gif sur Yvette le 24 septembre 2020, par

Adrien PICQUENOT

Composition du jury:

Monique Arnaud Chercheuse CEA, Laboratoire AIM, CEA, Université Paris-Saclay	Présidente
Fabrizio Bocchino INAF, directeur de l'Observatoire de Palerme	Rapporteur
Régis Terrier Directeur de recherche, CNRS, Laboratoire APC, Université de Paris	Rapporteur
David Mary Directeur de recherche, CNRS, Observatoire de Nice	Examinateur
Jacco Vink Professeur, Université d'Amsterdam	Examinateur
Fabio Acero Chargé de recherche CNRS, Laboratoire AIM, CEA, Université Paris-Saclay	Directeur
Jérôme Bobin Chercheur CEA, Laboratoire AIM / DEDIP, CEA, Université Paris-Saclay	Invité

Thèse de doctorat

NNT: 2020UPASP028

” Look ! Up in the sky ! It’s a star ! It’s a planet ! It’s Supernova ! ”

Tycho Brahe, 1572

Synthèse

Certaines sources étendues, telles que les vestiges de supernovae, présentent en rayons X une remarquable diversité de morphologie que les téléscopes de spectro-imagerie actuels, qui produisent des données tridimensionnelles contenant deux dimensions spatiales et une spectrale, parviennent à détecter avec un exceptionnel niveau de précision. Cependant, les outils d'analyse actuellement utilisés dans l'étude des phénomènes astrophysiques à haute énergie peinent à exploiter pleinement le potentiel de ces données : les méthodes d'analyse standard se concentrent sur l'information spectrale sans exploiter la multiplicité des morphologies ni les corrélations existant entre les dimensions spatiales et spectrales ; pour cette raison, leurs capacités sont souvent limitées, et les mesures de paramètres physiques peuvent être largement contaminées par d'autres composantes.

Dans cette thèse, nous explorons une nouvelle méthode de séparation de source exploitant pleinement les informations spatiales et spectrales contenues dans les données X, et leur corrélation. Cette méthode est basée sur l'algorithme GMCA (pour Generalized Morphological Components Analysis), initialement développé dans le but d'extraire une image du CMB des données de *Planck*. Puisqu'il s'agit de la première application de cet algorithme à des données X, nous commençons par présenter son fonctionnement et les principes mathématiques sur lesquels il repose, puis nous étudions ses performances sur des modèles de vestiges de supernovae. Nous présentons également l'algorithme pGMCA, une nouvelle version de GMCA prenant en considération la nature poissonienne de nos données, et développée par la même équipe durant cette thèse. Nous nous penchons ensuite sur la vaste question de la quantification des erreurs pour des estimateurs non-linéaires, question clé à laquelle il n'existe pas encore de réponse universellement applicable. Enfin, nous appliquons notre méthode à l'étude de trois problèmes physiques relatifs à des sources étendues en rayons X.

La première application concerne les asymétries dans la distribution des éléments lourds du vestige Cassiopeia A. De récentes simulations ayant montré la possibilité pour des asymétries présente lors de l'explosion d'être encore visibles après plusieurs siècles, il apparaît qu'une meilleure connaissance des asymétries au sein des vestiges de supernovae peut aider à mieux comprendre les mécanismes initiaux. En particulier, la quantification des asymmétries et la comparaison des distributions des différents éléments chimiques ainsi que la direction dans laquelle ils sont éjectés nous permettent de contraindre certains mécanismes, tels que l'éjection de l'étoile à neutron dans une direction opposée au gros de l'éjecta. Notre deuxième application concerne les filaments visibles dans l'émission synchrotron de plusieurs vestiges de supernovae en rayons X, dont Cassiopeia A, manifestation d'électrons accélérés à très haute énergie au niveau du choc. Les modèles principaux divergeant sur la dépendance en énergie de la largeur de ces filaments, nous tâchons de comparer les largeurs de filaments choisis sur des images produites par GMCA du synchrotron de Cassiopeia A à différentes énergies. Enfin, nous appliquons notre méthode à un autre type de source étendue : l'amas de galaxies Perseus. Nous y cherchons la contrepartie X des structures filamentaires visibles en optique. Avec 20 ans d'archives à revisiter des satellites *Chandra* et *XMM-Newton* et la complexité croissante des télescopes à micro-calorimètres X à venir, le développement de nouvelles techniques d'analyses peut jouer un rôle crucial afin d'exploiter au mieux les informations scientifiques contenues dans ces données. Cette thèse en montre quelques exemples, et se propose d'ouvrir la voie à l'utilisation des algorithmes GMCA et pGMCA dans l'étude des sources étendues en rayons X, riche en perspectives.

Acknowledgements

First of all, I would deeply like to thank Fabio Acero for the amazing subject he offered me, and for his caring, efficient and enthusiast mentoring. And, of course, for being such a wonderful person with whom I have shared much more than a working relationship. Thanks again for introducing me to some of your numerous side projects ; Science, Beauty or whatever concepts we attach to human knowledge, need people as curious and passionate as you are.

Thanks to Jérôme Bobin for the amazing tool you developed, and for your support throughout the thesis. You taught me a lot, and invariably answered aptly to my questions. It was always a pleasure meeting you on purpose, or by accident at the cafeteria. Our discussions could lead to many and many a year of research.

I would also like to thank people at the CEA who have always been supportive and patient enough to explain me the basics of high energy astrophysics. Jean Ballet, for his patience and his enlightened proof readings, whose sharp insights sometimes kill the vibes, but always lead to more beneficial approaches for science. Gabriel Pratt, for his kindness, his advice, and his native English speaker proof readings. Pierre Maggi, of course, ye olde office mate, for his several, kind and accurate proof readings, and for all the good moments we spent together. I would never have imagined going to an Iggy Pop concert with " some guy from work ", and that it would actually please me.

Thanks also to the other PhD students or trainees I was lucky enough to meet during my stay at the CEA : Antoine, Floriane, Francesco, Imane, Lisa, Luca, Morgan, Quentin, Raph, Rebecca, Théo, Vicky, Victor and Virginia. You really had some influence on making the almost daily journey to Saclay a little bit less nightmarish.

By the way, I would really like not to thank Saclay for being that far from Paris.

My work-related acknowledgements would not be complete without a special mention of my Marxist friends from the Saclasheat Team. Congratulations guys (and girl), the Machine was shaken by our constant rants ! And more importantly, you made me enjoy these lunch breaks in the canteen at the end of the world.

And eventually, thanks to this weird thing we call reality, for showing just enough consistency for us to entertain ourselves with some cool models and theories.

Let us also take advantage of the occasion to thank all the people I like, love, that have mattered in my life. After all, I don't write acknowledgements on a daily basis.

My family, of course, my friends, and the others. There's more to life than searching for stuff in the sky, and I am greatly surrounded enough to enjoy every bit of it. Well, not every bit, but rot is part of the fruit, innit ? And, in the end, the people I love constitute a significant portion of the gorgeous parts.

Special big up to the boyz from the 51. These were amazing years, and here is another end to it. These are truly the last days.

CONTENTS

LIST OF FIGURES

CHAPTER 1

GENERAL INTRODUCTION

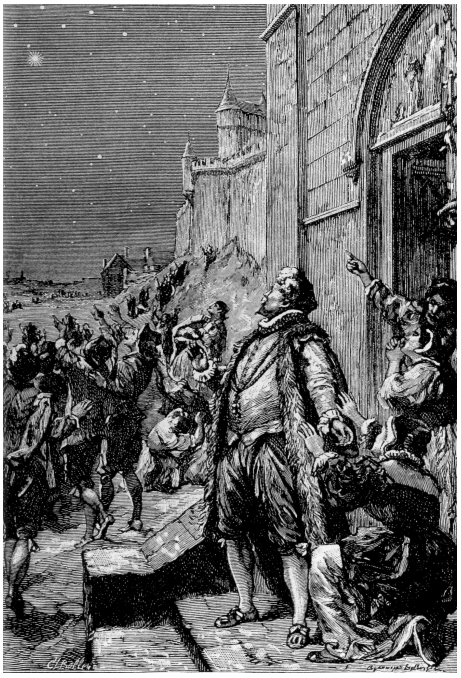

FIGURE 1.1: Tycho Brahe observing a " stella nova ", the supernova SN1572. Engraving appearing in the Historical book " Astronomie Populaire " by Camille Flammarion (Paris, 1884).

His eyes plunged into the deep black sky, Tycho Brahe noticed a luminous spot he had never seen before. " Gosh ! he marveled, what in heaven is this wizardry ? " He squinted, reducing his eyes to a thin slit and trying to focus. Neither the heady scent of the lilies nor the solemn call of the midnight owls could distract him from his observation, for he was absorbed in a tempest of contradictory thoughts storming his brains. " Could this ever be ?... ", he wondered out loud, and without even concluding his thought, he jumped to his feet and ran through his laboratory, desperately searching for some parchments and ink. " I must take notes, he mumbled, lest this all ends up as in a dream ! " He found what he needed and limped hurriedly back to his balcony. " Thank God, it is still here ! " he cried out, and immediately started to scribble. " This is going right down in History ! " he exclaimed happily, fully aware of his newly assigned task and willing to devote himself completely to its fulfillment. " God has made me His humble servant, and I shall be worthy ! " For hours and hours he took measures and scribbled unremittingly, without noticing the night fading out and the sky lightening leisurely. When he could no longer see what he thought as a new star, it was already day.

1.1 Supernovae

Supernovae have played a major role in the history of astronomy and astrophysics. Tycho Brahe in 1572 and Johannes Kepler in 1604 were the first occidental astronomers of our era to notice what they interpreted as a new star appearing for a limited duration in the sky, calling the phenomenon " stella nova " (see Figure 1.1 and 1.2).

We can find mentions of similar events in other cultures : Arabic, Korean or Chinese manuscript mention phenomena we can now interpret as supernovae. The ancient records show a real concern for precision in their description and their centuries long registers, informing us on the importance that was given to the observation

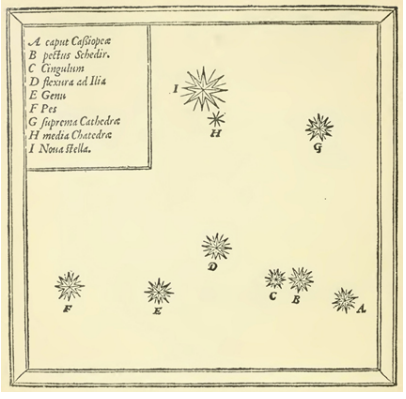

FIGURE 1.2: Star map of the constellation Cassiopeia showing the position of SN1572 (labelled I). Taken from Tycho Brahe's *De nova stella.*

of the sky, mainly for religious or divinatory reasons. In old Chinese manuscripts, no less than a few dozens of supernovae are related, the oldest dating back to 1500 B.C.

However, the events observed by Tycho Brahe and Johannes Kepler were those that played the most important role among all historically known supernovae. They happened in a time of change in the mentality of erudites, who were keen to accord a closer attention to the physical understanding of natural events than to their metaphysical meaning. Opposing other observers arguing that the " stella nova " he observed was something happening in the Earth's atmosphere, Tycho Brahe measured the parallax of the object, and noted that it did not move, showing it had to lie far away. Galileo later used this as an argument against the Aristotelian view of the immutable heavens residing beyond the moon. In that way, the " stella novae " contributed to the philosophical change that gave birth to our modern occidental science, supporting the idea that the sky was not a flawless, unmoving and divine entity but a part of nature that could be studied and described as such.

1.1.1 Classification

As it turned out, the new stars observed by Tycho Brahe and Johannes Kepler were actually exploding dying stars. The phenomenon, now called " supernova ", is a transient astronomical event releasing an extraordinary amount of energy of about 10^{53} erg, most of it being released in the form of neutrinos ; about 1% in kinetic energy transfers to the ejecta and about 0.01% is converted into electro-magnetic radiation. It is visible in the optical domain before fading over several weeks or months. In 1941, Rudolph Minkovski introduced a classification that is still in use. Initially, it was based only on the spectrum, now it uses the light curves and the absorption lines of different chemical elements appearing in their spectra. It does not take into account the nature of their progenitor or their mechanisms of explosion, that were not known at that time.

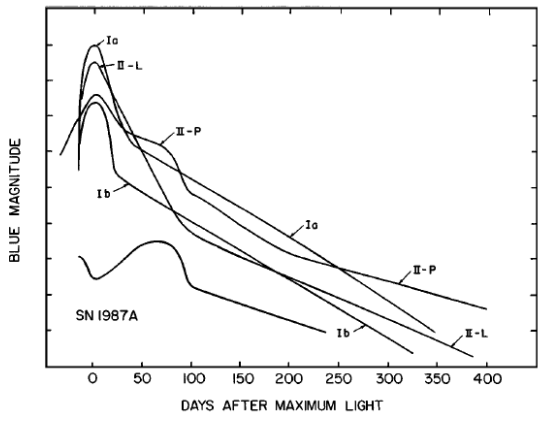

FIGURE 1.3: Schematic light curves for supernovae of Types Ia, Ib, II-L, II-P, and SN 1987A. The curve for supernovae Ib includes SNe Ic as well, and represents an average. For supernovae II-L, supernovae 1979C and 1980K are used, but these might be unusually luminous. From Wheeler & Harkness (1990).

This classification separates Type I supernovae showing no hydrogen lines in their spectra from the Type II, that show hydrogen. Type Ia supernovae present a singly ionized silicon line at 615 nm, while Type Ib and c show no silicon absorption feature, or a weak one. The separation between these two subtypes relies upon the presence or not of helium in the spectra : Type Ib shows a non-ionized helium line at 587.6 nm while Type Ic supernovae show no helium line, or a weak one.

Type II supernovae can also be separated into subtypes based on the morphology of their lightcurves. Some of them show hydrogen in the beginning, but over a period of weeks or months are dominated by helium lines, resembling Type Ib supernovae : they are classified as Type IIb. Most of the Type II supernovae have broad emission lines ; those that have narrow features in their spectra are classified as Type IIn. Among the other ones, the supernovae whose lightcurve reaches a plateau are labelled Type II-P while the ones that do not show a distinct plateau are called Type II-L. See Figure 1.3 for a presentation of the typical lightcurves of each supernova types.

Some supernovae do not fit correctly in any of these categories. Some additional supernovae types have been defined to described them, but generally, they are simply labelled as " peculiar ".

This supernovae classification has been criticized and mainly holds for historical reasons. It does not take into account the nature of the progenitor or the explosion mechanisms at stake, and the detection of an increasing number of peculiar supernovae show that the current types are not relevant to describe every supernovae. Also, imposing a discrete classification on an imperfectly understood phenomenon can be misguiding and distort following interpretations. For these reasons, even if detection programmes still use this classification, recent papers mainly classify supernovae in two categories reflecting better the underlying physics of the explosion mechanisms : core-collapse supernovae and thermonuclear supernovae.

1.1.2 Thermonuclear supernovae

Type Ia supernovae represent about 30% of all supernovae in our Galaxy (see Ptuskin et al., 2010), and have a progenitor type and mechanisms of explosion different from the Type Ib, Type Ic and Type II supernovae. They occur in binary systems, where a white dwarf accretes matter until it can no longer support its own weight. This accretion of matter can be the result of two scenarii.

In the single degenerate scenario, the white dwarf forms a binary system with a more massive star. Gas from the companion star is stripped to form an accretion disc around the white dwarf.

In the double degenerate scenario, the binary system is composed of two white dwarves. Their orbit decaying, they merge ; if the mass of the resulting star is sufficient, it will explode. We still do not have a precise idea of the relative quantity of single and double degenerate scenarii.

The temperature in the core increases with the mass, which results in a convection period. At some point, an ignition occurs, whose mechanism is still unknown. Simulations seem to indicate that there needs to be some asymmetries in the distribution to spark the ignition. The burning is then propagating through a thin combustion wave. Current Deflagration-to-Detonation Transition models (DDT) assume the combustion wave propagates as a deflagration due to micro-physical transport processes, releasing energy by reactions in the burning zone. Conduction and diffusion lead to heating of the fuel ahead of this zone so that it also reaches conditions for burning (see Röpke, 2017). The propagation then evolves into a detonation, where the shock wave progresses by compressing and heating fuel material so that

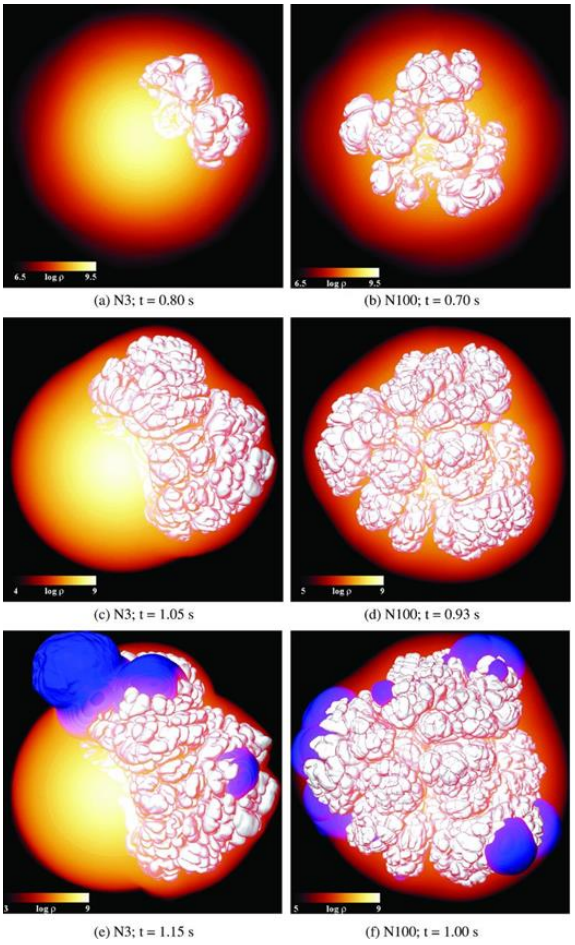

FIGURE 1.4: Two simulations of a Deflagration to Detonation Transition in a Type Ia, presenting two ignition setups. On the left, the setups include three ignition kernels (N3). On the right, they include a hundred ignition kernels (N100). The top row shows the rising plumes of the deflagration level set (white) during the Rayleigh-Taylor-unstable stage of the deflagration phase embedded in a volume rendering of the density (in g.cm^{-3}). The middle row shows the density and deflagration level-set structure at the time the first DDT occurs. The bottom row shows the subsequent spreading of the detonation level set (blue) from the DDT initiation sites. The small number of ignition kernels necessarily leads to a highly asymmetric seed configuration of the RT-unstable deflagration plumes, which can be noticed in the N3 case. From Seitenzahl et al. (2013).

it starts to burn, releasing, in turn, the energy to further support the shock wave. The temperature increase enhances the reaction rates, releasing energy that also raises the reaction rate. Unlike deflagrations, the propagation is not determined by microphysical transport processes but by hydrodynamical effects, leading to a faster, supersonic propagation (see Röpke, 2017).

However, the reason for this spontaneous transition of the burning mode from a subsonic deflagration to a supersonic detonation in an unconfined medium is still unknown. Zel'dovich et al. (1970) proposes a model requiring a preconditioning of the fuel material with hot spots that would endure autoignition. This configuration may lead to a runaway of the reactions with a phase velocity sufficient to evolve into a detonation wave. It has been speculated that sufficiently strong turbulences in the deflagration burning could create these hot spots, but it is difficult to identify such regions in simulations. Therefore, several simulations artificially prescribe these spots or trigger the transition to detonation once the deflagration flame reaches a certain density threshold (see Figure 1.4). Simulations presented in Poludnenko et al. (2011) propose another transition model, in which hot spots are not necessary. An overpressure rises in the thin combustion wave, increasing the pressure which compresses and heats up the combustion wave. This increases the propagation speed, leading to further fuel compression and giving birth to a strong shock within the thin combustion wave, creating in turn the conditions in which a detonation can arise.

Within a few seconds after the beginning of the detonation, carbon and oxygen fuse to produce heavier elements and the star violently explodes, releasing an energy of 10^{51} erg and producing a shock wave in which matter from the progenitor is ejected at about $30,000$ km.s^{-1}.

1.1.3 Core-collapse supernovae

Type Ib and c and Type II supernovae are the results of massive stars of more than $8\ M_{\odot}$ undergoing core collapse when the pressure induced by nuclear fusion can no longer counter the effects of gravity. The core collapses into a neutron star (or a black hole for the heaviest progenitors) and the outer layers of the star are ejected.

It has been proven that the bounce of the forming neutron star, or proto-neutron star, was not sufficient to produce the shock wave ejecting the outer layers of the progenitor. A popular theory to explain the explosion mechanisms is the heating by the expelled neutrinos of the outer layers. After the matter collapses and bounces on the proto-neutron star, the shock is stalled. The neutrinos then heat up the ejecta, enough to revive the shock. The presence of oscillating and sloshing instabilities makes this mechanism more efficient by bringing closer to the proto-neutron star parts of the shock front, simplifying the heating. Some simulations have shown this mechanism could transfer enough energy to the outer layers to initiate the shock ; however, it may not be sufficient to explain the most energetic supernovae. Magnetohydrodynamic mechanisms, in particular in rapidly spinning stars, can also play a role by extracting energy from the highly magnetized neutron star to violently expel the outer layers of the progenitor (see Janka, 2012, for a discussion about possible explosion mechanisms).

Observations show that the newly created neutron star is ejected with a certain velocity from the center of explosion. The kick mechanisms necessary to initiate this ejection are not perfectly understood yet, but the proposed models usually need to assess the existence of asymmetries in the original explosion. An asymmetric initiation of the explosion can indeed impart a kick to the neutron star due to linear momentum conservation (" gravitational tug-boat mechanism " ; see Figure 1.5). An asymmetric expulsion of gas would also conduce to hydrodynamical interactions between the proto-neutron star and the ejecta, which would be coupled with an anisotropic gravitational pull of the ejecta on the proto-neutron star, inducing a kick. An

anisotropic neutrino emission has also been considered as a potential neutron star kick mechanism. In any case, asymmetries seem to be a key element to understand fully the core-collapse explosion mechanisms and the observed neutron star kick.

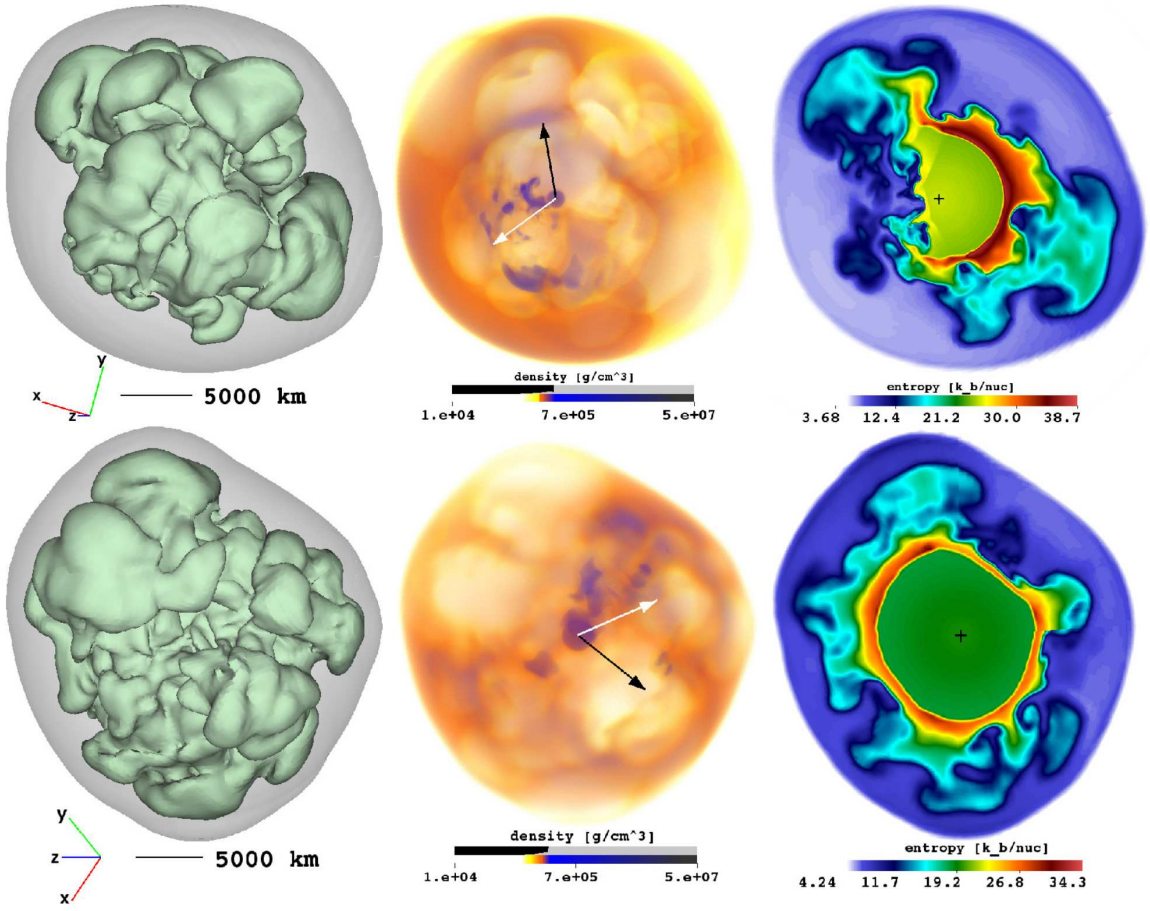

FIGURE 1.5: Entropy-isosurfaces (left) of the SN shock (grey) and of the high-entropy bubbles (green), ray-casting images of the density (middle), and entropy distribution in a cross-sectional plane (right) for two models of core-collapse supernova simulations at about 1.3 s and 1.4 s after core bounce. The viewing directions are normal to the plane spanned by the neutron star kick and spin vectors of each model, which also defines the plane for the entropy slices. The SN shock has an average radius of 13,000 km and 14,000 km for each model, respectively (a length of 5000 km is given by yardsticks below the left images). The kick and spin directions are indicated by the white and black arrows, respectively, in the middle figures. The neutron star locations are marked by black crosses in the right plots. The images in the middle correspond roughly to the projections of the density distribution on the observational planes. Dilute bubble regions are light-colored in white and yellow, while dense clumps appear more intense in reddish and bluish hues. The purple circular areas around the neutron star represent the dense inner region of the essentially spherically symmetric neutrino-driven wind. The wind is visible in green in the right images and is bounded by the aspherical wind-termination shock. The neutron star is clearly displaced from the geometrical center of the expanding shock in the direction of the kick vector pointing to the lower left for the model on top. The neutron star in model on the bottom has a much smaller kick velocity, and does not show any clear displacement but remains located roughly at the center of the expanding ejecta shell. From Wongwathanarat et al. (2013).

Summary :

- A supernova is the explosion of a star that we call its " progenitor ".
- There are two main types of supernovae : the Type Ia, or thermonuclear supernovae, and the core-collapse supernovae.
- Thermonuclear supernovae are the results of white dwarves accreting from a companion star in a binary system, either by accreting gas from a stellar companion (single degenerate scenario) or by merging with another white dwarf (double degenerate scenario). Reaching a certain mass ignites a thermonuclear reaction leading to the explosion.
- Core-collapse supernovae are caused by massive stars ($> 8\ M_{\odot}$) in which the pressure induced by nuclear fusion can no longer counter the effects of gravity. The core forms a neutron star or a black hole, and the outer layers are ejected.
- For both supernovae types, some key elements are still missing to understand fully the explosion mechanisms. In both cases, the presence of instabilities and asymmetries in the explosion seems to be a key ingredient.

1.2 Supernovae remnants

Whatever the supernova type, the explosion ends up expelling stellar material at velocities of about $30,000$ km.s^{-1}. Ahead of these ejecta, a powerful shock wave forms that heats up the interstellar medium to temperatures up to million degrees temperatures. The shock wave is progressively slowed down by the interstellar medium, but it continues its expansion for several thousands years. These objects are called supernovae remnants (SNRs).

Heated material from the ejecta or the shocked interstellar medium emit electro-magnetic radiations long after the end of the explosion. Through these radiations, the SNRs can be observed. A gas heated at 10^7 K will have its thermal emission peaking in the X-ray band, making the X-rays an appropriate domain to observe SNR. They are also visible in radio and gamma-rays through the radiation of the particles they accelerate.

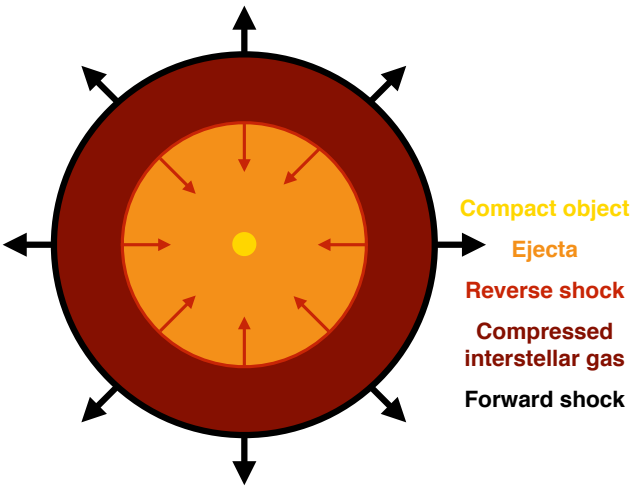

FIGURE 1.6: Scheme presenting the structure of a SNR. The compact object, present only in core-collapse supernovae, is either the neutron star or the black hole formed by the collapse of the progenitor's core.

Most SNRs can be seen in X-rays or gamma-rays, but some of them can also be detected in the optical domain.

1.2.1 Supernovae remnants stages

The evolution of a SNR over time can be divided into three phases. During the first one, the SNR is in free expansion. The front of the expansion is formed from the shock wave heating up the interstellar medium to approximately 10^7 K and expanding in the forward direction. The contact of the interstellar material causes a second shock to form, directed in the reverse direction (see Figure 1.6). This reverse shock goes back through the ejecta, heating it up. The forward shock pushes the interstellar medium into an expansive shell whose expansion velocity is constant. This phase can last for a few hundred years, until the mass of the interstellar material swept up by the shock exceeds the phase of the ejected material.

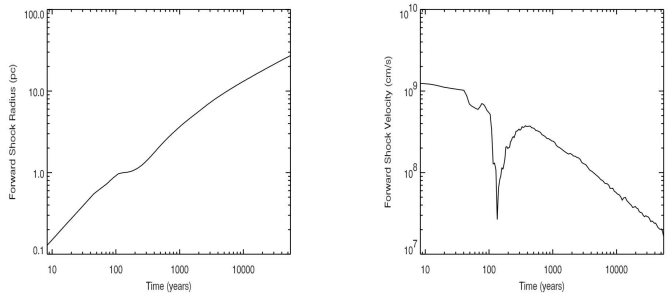

FIGURE 1.7: Radius (left) and velocity (right) during the evolution of a SNR in a wind-blown cavity, surrounded by a dense, swept-up shell. From Dwarkadas (2007).

The second one is the Sedov phase, during which the ejecta begins to decelerate, its velocity evolving in proportion to $t^{-3/2}$, t being the age of the SNR (see Figure 1.7). During this phase, Rayleigh-Taylor instabilities arise once the mass of the swept up interstellar medium approaches that of the ejected material, mixing the ejecta with the shocked gas from the interstellar medium. This phase lasts for a period spanning from a few thousands years to about $20,000$ years.

The last phase, or radiative phase, begins after the shell has cooled down to a temperature of less than 10^6 K. Electrons start recombining with the heavier atoms, making the shell radiate energy more efficiently. This results in cooling down the shell faster, making it thiner and denser. The more the shell cools down, the more atoms can recombine ; hence, the shell slims down and the SNR radiates most of its energy as optical light. The velocity then decreases in proportion to t^{-3} and the expansion of the shell stops. This period lasts for a few hundred of thousands years. After millions of years, the SNR will be completely diluted into the interstellar medium thanks to the Rayleigh-Taylor instabilities forcing the mixing of the SNR material.

1.2.2 Acceleration in SNRs and cosmic rays

With 10^{51} erg released in kinetic energy during the explosion, SNRs are ideal sites to accelerate particles and are thought to be the main source of galactic cosmic rays. The ion acceleration can be very efficient to transfer kinetic energy, especially in shocks parallel or quasi-parallel to the background magnetic field : about 10% to 20% of the bulk flow energy is channeled in energetic particles (Caprioli & Spitkovsky, 2014a). These particles induce a turbulent amplification of the magnetic field around the shock that will in turn contribute to accelerate particles from the interstellar medium. This magnetic field possesses inhomogeneities that are enhanced by the particles themselves. Thus, a moving particle entering the shock front will be accelerated through the diffusive shock acceleration mechanism : the particle arriving upstream and going downstream through the shock will encounter a moving change in the magnetic field that will reflect it again through the shock. The process can repeat itself several times, the particle gaining energy such that $\frac{\Delta E}{E} = \frac{\Delta V}{c}$ at each crossing until it finally escapes. See Figure 1.8 for a presentation of a simulation of this phenomenon.

Through this process, particles from the interstellar medium can be accelerated by SNRs. Recent observations and simulations have proven that at least a part of the cosmic rays we can observe are produced this way. However, there are still questions about the acceleration and liberation mechanisms and about the most energetic galactic cosmic rays (more than 10^{15} eV) that the current simulations fail to reproduce.

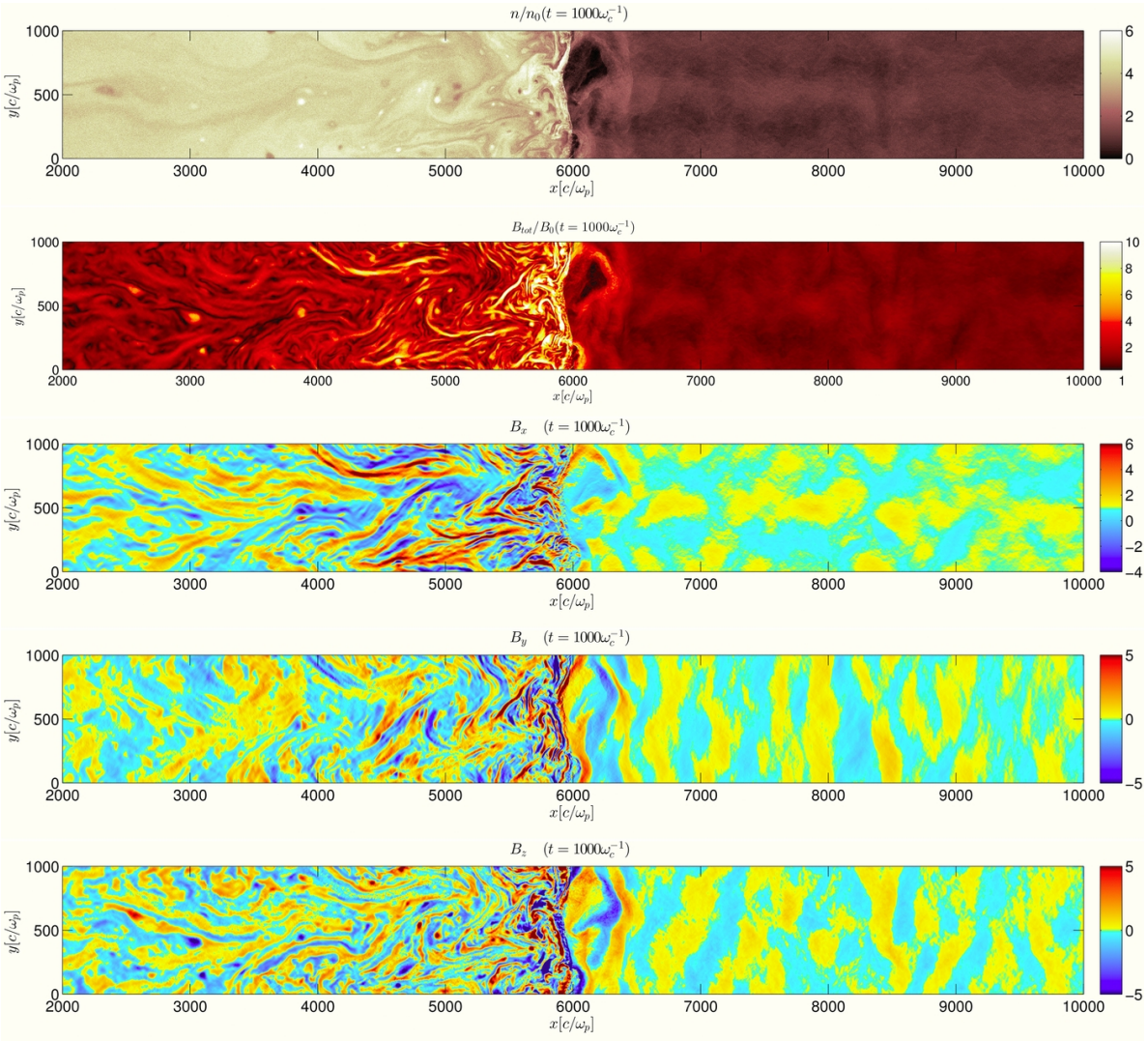

FIGURE 1.8: Relevant physical quantities for a parallel shock. From top to bottom : ion density, modulus and three components of the magnetic field, in units of their respective initial values. We can see the turbulent magnetic field generated by the accelerated ions. Caprioli & Spitkovsky (2014b).

Nevertheless, SNRs appear to be essential in our understanding of cosmic rays, and a better knowledge of the acceleration mechanisms would make us know if there needs to be any other sources to account for the existence of the most energetic cosmic rays.

1.2.3 Asymmetries in supernovae remnants

Expelled at a spectacular speed from the center of explosion, the shock rapidly expands to form a large astronomical object of a typical size of several parsecs after a few centuries. This large size allows us to obtain precise images of the remnants even at kpc distances and thus study their morphology.

In particular, the study of asymmetries in SNRs, either on their global shape materialized by the front shock or on the repartition of each individual elements, may bring some information about the mechanisms of explosion at stakes in the original supernova. Although the asymmetries of the surrounding medium crossed by the forward shock also have a clear impact that is difficult to decorrelate from hypothetical asymmetries

in the explosion, some observations and simulations concur to assert their existence. Jet-like structures that have been observed in several core-collapse SNRs are for example thought to be the direct consequence of their explosion mechanism. Orlando et al. (2016) has explored the evolution of the asymmetries in Cassiopeia A thanks to simulations beginning from the immediate aftermath of the supernova and presenting the 3D interactions of the remnant with the interstellar medium. Similar simulations presenting the evolution of a Type Ia SNR over a period spanning from one year after the explosion to several centuries afterwards have been made by Ferrand et al. (2019), showing that asymmetries present in the original supernova can still be observed after centuries. These results show how the observation of asymmetries in SNRs can help constraining and understanding the explosion mechanisms in supernovae.

Summary :

- In supernovae remnants (SNRs), the front shock still expands after centuries, heating up the interstellar medium.
- Another shock wave is produced, directed towards the center of the explosion, heating up the ejecta, the matter expelled from the progenitor.
- A strong magnetic field develops around the shock. It can trap particles, while the shock accelerates them until they are released. At least a part of the galactic cosmic rays we can observe are produced by this phenomenon.
- Some asymmetries in the explosion in supernovae can still be observed after centuries in SNRs. An extensive study of asymmetries in SNRs could help understanding the mechanisms of explosion in supernovae.

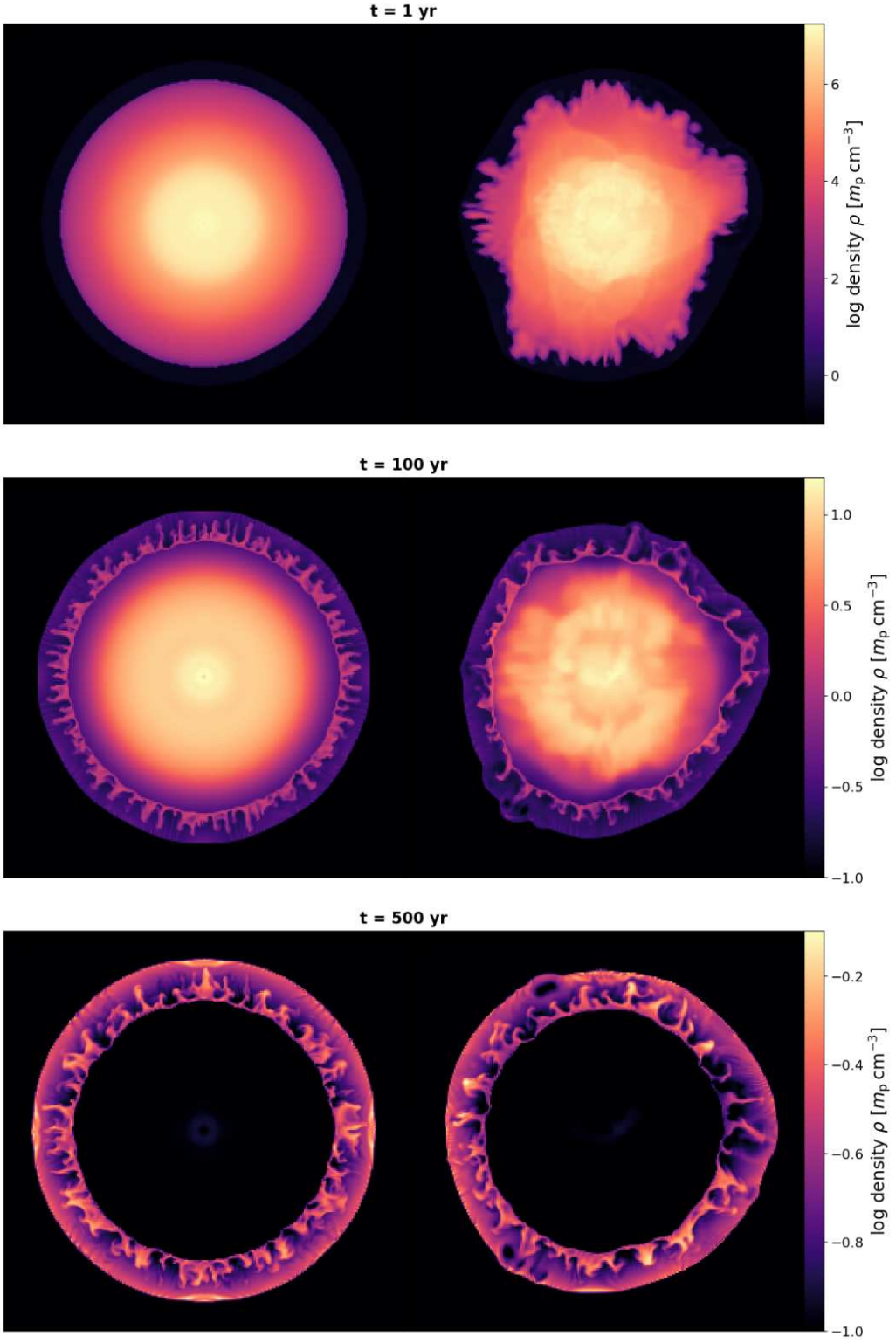

FIGURE 1.9: Slices of the mass density at t = 1 yr (top), 100 yr (middle), and 500 yr (bottom) of the evolution of two simulations of SNRs. The left side shows the case of spherically symmetric ejecta (effectively 1D initial conditions), while the right side shows the case of asymmetric ejecta (fully 3D initial conditions). Note that the color scale is logarithmic and that its upper value is adjusted over time so that all frames have similar contrast (the density in the inner ejecta decreases by several orders of magnitude over this period). From Ferrand et al. (2019).

1.3 Supernovae remnants in X-rays

SNRs can still be detected long after the end of the explosion itself, because the hot gas and the accelerated particles still radiate in a large range of wavelengths (see Figure 1.10). In this thesis, we will focus on the observation of SNRs in X-rays ; hence, we will describe the different types of emission in this domain and the current instruments allowing us to observe them.

1.3.1 Continuum emissions

There are five mechanisms that can produce continuum X-ray emission in SNRs, two non-thermal (the synchrotron emission and the comptonization), and three thermal (the bremsstrahllung, the free-bound emission and the two-photon emission). These radiations are continuous, because they are caused by a variation of velocity of electrons, and the population of electrons can reach a continuous range of energies.

The first mechanism, the synchrotron radiation, is linked to the magnetic field and to the particles it accelerates. It is emitted when an electron interacts with the magnetic field that will cause the electron to change its direction by exerting a force perpendicular to its original direction. The electron will then be accelerated, and radiate electromagnetic energy. This radiation can range over the entire electromagnetic spectrum, including X-rays in young SNRs.

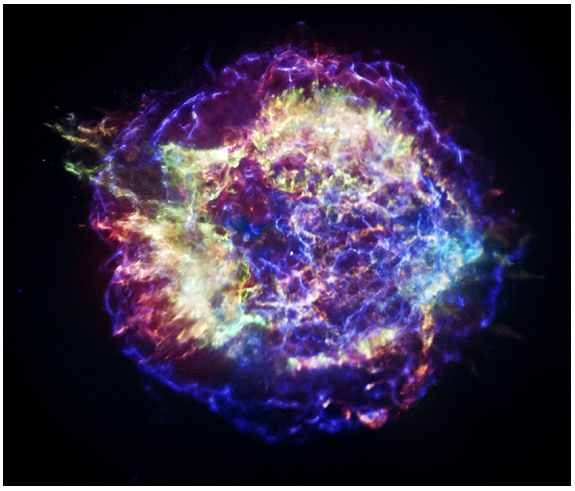

FIGURE 1.10: Cassiopeia A in X-rays as seen by the *Chandra X-Ray Observatory*. The synchrotron emission is in blue, other colors correspond to thermal emissions.

The comptonization happens when a photon collides with an electron. If the photon gives energy to the electron, accelerating it, the effect is named " Compton scattering ". If the electron gives energy to the photon, the effect is named " Inverse Compton scattering ".

The thermal bremsstrahlung occurs when an electron passes close to a ion in a hot gas, the strong electric forces causing its deceleration and a change in its trajectory. The electron will lose kinetic energy, which will be converted into radiation. In a gas with a temperature of some millions of degrees Kelvin as in SNRs, the radiation will peak in the X-ray band.

The free-bound emission arises when an electron is captured into one of the atomic shells. Free-bound emission mainly looks like a bremsstrahlung because it is not quantised and follows a Maxwell-Boltzmann distribution. In photo-ionized or overionized plasmas, it can possess line-resembling features called radiative-recombination continua.

Two-photon emission results from electrons in meta-stable states. If they are not de-excited by a collision, which is likely in rarified plasmas of SNRs, it can de-excite by emitting two photons.

In SNRs, the gas heated by the explosion, either from the ejecta or the interstellar medium, reaches temperatures at which most of its thermal emissions in X-rays will be caused by thermal Bremsstrahlung and line emissions. However, the parameters characterizing the different thermal emissions are not easy to retrieve as the plasmas formed by the hot emitting gas are often out of ionization equilibrium, because with the

low densities involved, not enough time has passed for enough collisions to happen in order to reach an equilibrium.

The presence of highly energetic electrons and the strong magnetic field can also be important sources of X-rays in SNRs through the synchrotron radiation. As it is located at the forward shock, these emissions give useful information about the location of the forward shock and insights about the acceleration mechanism taking place.

1.3.2 Line emissions

Another type of features that are emitted in X-rays in SNRs is the line emission associated with the different elements of the ejecta or of the heated interstellar medium. These emissions result from collisional excitation of ions, often through an electron-ion collision, and radiate at a precise energy characteristic of the emitting element and of its ionization state.

In plasmas that have not reach their ionization equilibrium, there can be inner shell ionization. In this process an electron from an inner shell can be removed while higher atomic levels are still filled. The ion can then de-excite without radiation by filling the hole or adjust radiatively, which is called fluorescence. The likelihood for a radiative transition, the fluorescence yield, is higher for atoms with larger nuclear charge. Because of its high fluorescence yield and high abundance, the Fe K-shell emission can be observed at all ionization states of iron if the electron temperature is high enough. For that reason, the iron line emission is an important diagnostic tool to evaluate the state of an SNR plasma through its average electron temperature and ionization age $n_e t$. By combining information from the continuum and line emissions in X-rays we can measure properties of the plasma such as the electron temperature, the ionization states and the abundances of the different elements, from oxygen to iron (see Figure 1.11).

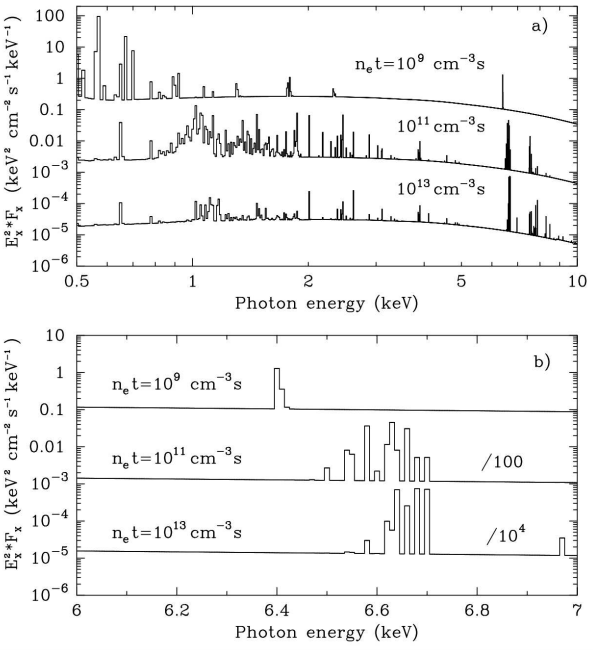

FIGURE 1.11: Thermal X-ray theoretical emissions between 0.5 and 10 keV (panel a) and around the Fe K line complex (panel b) of an optically thin transient plasma with solar abundances and electron temperature $Te = 3 * 10^7$K, for three values of the ionization parameter. For $n_e t = 10^{13}$ cm^{-3}.s, the plasma has reached the ionization equilibrium. From Tatischeff, V. (2003).

In general, being able to retrieve maps corresponding to every line emissions gives fruitful information about the spatial distribution of each element. This way, we can link their behaviors to their individual properties for a better understanding of the evolution of the original progenitor's layers after the explosion. We can also have an insight on the asymmetries in the ejecta for each individual element, which could help to understand the explosion mechanisms.

1.3.3 Spectro-imaging instruments in X-rays

FIGURE 1.12: Artist's impression of the *Chandra X-Ray Observatory*.

X-rays being absorbed by Earth's atmosphere, the telescopes to detect them have to be carried by satellites orbiting above it. Unlike optical telescopes, X-ray telescopes possess almost cylindrical mirrors presenting a low grazing angle in order to reflect photons that would otherwise pass through them. The X-ray detectors capture photons individually, so that for each one four measures are taken : its spatial coordinates x and y, its energy E and the time of detection t. Hence, we call these instruments spectro-imaging instruments, and the data they capture takes the form of an hypercube (x, y, E, t). As SNR are not evolving fast enough for the time of detection to be an important factor, we will consider the data to be of the form of a cube (x, y, E).

The two main spectro-imaging instruments currently in activity are onboard *Chandra*, launched by NASA in 1999 and *XMM-Newton* launched by ESA the same year (see Figures 1.12 and 1.13). *Chandra* has the best angular resolution : 0.5 arcseconds, against approximately 6 arcseconds for *XMM-Newton*, resulting in sharper images. However, *XMM-Newton* has a larger field of view, and its collecting area is substansially bigger than that of *Chandra* ($2,000$ cm^2 against 400 cm^2 at 1 keV). They both have a similar spectral resolution (see an example of *Chandra* spectrum in Figure 1.14, right).

FIGURE 1.13: Artist's impression of the *XMM-Newton* spacecraft.

The images and spectra obtained by these instruments on large astronomical objects like the SNRs are astounding, but their high quality data is not fully exploited by the data analysis methods currently in use in this field : most of the information is often lost by considering only the spectral dimension, even if the spatial and spectral dimensions are intrinsically entangled. With the development of the future generation of X-ray space telescopes, among which *Athena* is the most advanced, the need of developing new tools appears even more urging. The spatial resolution of *Athena* will be better than that of *XMM-Newton*, while its spectral resolution of 2.5 eV will be outstandingly better than that of its predecessors thanks to the micro-calorimeter technology allowing to measure with great precision the energy deposited by each X-ray photon (Barret et al., 2020). The arrival of such a new spectro-imaging instrument could bring an amazing quantity of new data to evaluate and improve our current knowledge on high energy astrophysics. However, we will need to develop better data analysis methods than those currently in use to fully exploit the potential of the new generation of spectro-imaging instruments.

1.3.4 Traditional data analysis methods in X-rays

Current data analysis methods in use in supernova remnant studies rarely involve a separation on the entangled components. They mostly consist in defining areas of interest in the data set flattened as an image, and extracting the spectra from these areas (see Figure 1.14 for an illustration). They are then processed

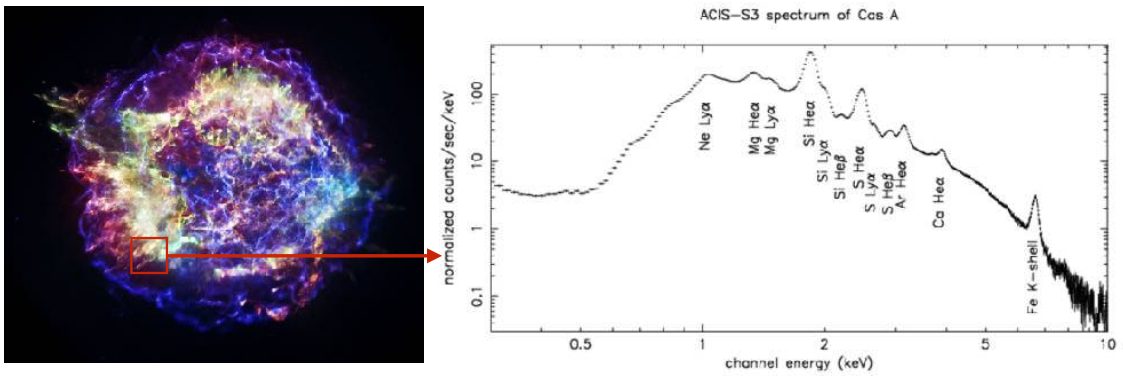

FIGURE 1.14: On the left, the same image as in Figure 1.10. On the right, Cassiopeia A's spectrum in X-rays as seen by the *Chandra X-Ray Observatory*[1]. The area surrounded by a red box figures an area of extraction for the spectrum, but does not correspond to the actual spectrum presented here. It has been added for illustrative purposes only.

through a software such as *Xspec*, where physical models chosen by the user are fitted in order to retrieve physical parameters such as the temperature, the abundance, the metallicity... As the user has to define the fitted models, a certain amount of prior physical information is needed. The different physical components also remain entangled as this kind of methods only produce a set of parameters, possibly from different components, without separating these components. When applied on a sufficient number of areas mapping the total remnant, maps of the parameters can be produced, but doing them is highly time consuming and the resulting images are poorly detailed. The total information contained in the (x, y, E) original data cube is not used, as the whole information is retrieved only on the spectra, and the areas of extraction are considered individually, thus neglecting the high correlation between them.

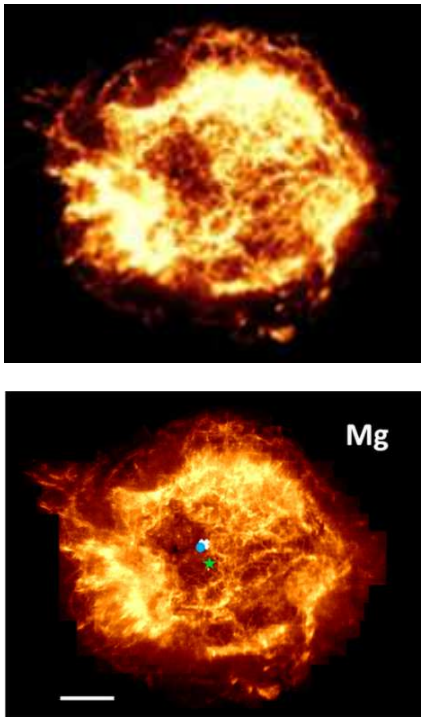

FIGURE 1.15: The Mg emission structure in Cassiopeia as retrieved with traditional data analysis methods. On top, extract from Figure 9 of Lopez et al. (2011). On the bottom, extract from Figure 2 of Holland-Ashford et al. (2020).

We see in Lopez et al. (2011) an example of component separation. In order to conduct this study, images of the different line emission structures in chosen SNRs was needed. They were obtained by integrating the data around the peak of each line emission, thus producing images of the emission structures still strongly polluted by other components such as the synchrotron continuum (see Figure 1.15). Other traditional methods involving component separation usually involve the use of *Xspec* on chosen areas to separate components in the spectra, and produce maps of the areas showing where each component is mainly present. As for the parameters map obtained in a similar way, the results are poorly detailed and do not exploit fully the information from the original data. The resulting images are also difficult to use, as the pixel values do not represent number of counts (see for example Holland-Ashford et al., 2020, see Figure 1.15)

The aim of this thesis is to explore a new data analysis method for component separation using both the spectral and spatial dimensions in order to exploit as much as possible the information contained in the X-ray data. In a first part, we will present the mathematical objects needed to develop our method. We will then explain the method, test it and propose a way to retrieve error bars attached to the results. In a second part, we

will show some applications of our method on real data, proving its usefulness to actually obtain results that could not have been obtained otherwise. Our first application will be on asymmetries in the SNR Cassiopeia A, in an attempt to map the repartition of the different line emissions and quantify their relative asymmetries, thus providing new information on a key topic in SNRs studies. Our second application will focus on the synchrotron rims that can be seen in X-rays in some SNRs. We will investigate the dependency of their widths with energy. The last application will be an attempt to test our method on another kind of extended sources in X-rays : the Perseus galaxy cluster. More specifically, we will search for an X-ray counterpart to the filaments visible in the Hα emission.

Summary :

- SNRs can be visible in X-rays. The matter heated up by the front or the forward shocks is hot enough for the thermal emission to peak in X-rays. Some non-thermal radiation processes also emit in X-rays.
- Among the thermal emissions in X-rays, the thermal bremsstrahlung and the line emissions are the most important. The line emissions characterize the chemical element by which they were emitted, thus allowing to map the presence of a certain element in a SNR by considering the sources of its line emission.
- Among the non-thermal emissions in X-rays, the synchrotron emission is the most important. It is caused by the accelerated particles radiating in an amplified magnetic field at the shock, allowing us to study the properties of accelerated electrons and the acceleration mechanism.
- X-ray telescopes such as *Chandra* and *XMM-Newton* contain spectro-imaging instruments producing data cubes composed of two spatial and a spectral dimension.
- Current data analysis methods in use in high energy astrophysics do not fully exploit the wealth of the existing and future spectro-imaging instruments. We intend in this thesis to provide a new data analysis method using both the spectral and spatial dimensions in order to exploit as much as possible the information contained in the X-ray data cubes.

[1] http://hea-www.harvard.edu/ChandraSNR/sample_spectrum.html

Part I

Methodology

CHAPTER 2

WAVELETS

Wavelets constitute a wide and rich mathematical fields particularly flourishing nowadays, with many applications on a large variety of subjects. A proper presentation of the formalism necessary to define and use wavelets in 2D on images going far beyond the scope of this thesis, we will only introduce them through their original one dimensional definition. The passage to two dimensions will not be presented in general, but only applied on the specific algorithm we will use later, the " à trous " algorithm.

2.1 Wavelets in one dimension

In this thesis, we will only use a two-dimensional kind of wavelets. However, it is far easier to understand the principle and the properties of the wavelet transforms by studying their original definition in one dimension. In this Section, we will introduce the continuous wavelet transforms in one dimension and their discretization to adapt them for actual computation.

2.1.1 Continuous wavelet transforms in one dimension

A wavelet is a square-integrable function of zero mean. Basically, a wavelet transform consists in a mother wavelet ψ and the child wavelets $\psi_{a,b}$ obtained through scaling and translation of ψ :

$$\psi_{a,b}(t) = \frac{1}{\sqrt{a}}\psi\left(\frac{t-b}{a}\right) \tag{2.1}$$

where a is a positive real defining the scale and b is a real number defining the shift. See Figure 2.1 for a classical example of mother wavelet.

It is possible to project a function $f \in L^2(\mathbb{R})$ onto the subspace of scale a :

$$f_a(t) = \int_{\mathbb{R}} WT_\psi\{f\}(a,b) \cdot \psi_{a,b}(t)db \tag{2.2}$$

where the wavelet coefficients $WT_\psi\{f\}(a,b)$ are defined as :

$$WT_\psi\{f\}(a,b) = \langle f, \psi_{a,b}\rangle = \int_{\mathbb{R}} f(t)\psi_{a,b}(t)dt \tag{2.3}$$

It can be rewritten as a convolution product, by defining :

$$\overline{\psi}_a(t) = \frac{1}{\sqrt{a}}\psi\left(\frac{-t}{a}\right) \tag{2.4}$$

Leading to :

$$WT_\psi\{f\}(a,b) = \int_{\mathbb{R}} f(t)\overline{\psi}_a(t-b)dt = f \star \overline{\psi}_a(u) \tag{2.5}$$

Wavelet transforms can measure the time evolution of frequency transients. The decay of $WT_\psi\{f\}(a,b)$ when the scale a goes to zero characterizes the regularity of f in the neighborhood of b (see Figure 2.2). In the regions where f is regular, the wavelet coefficients rapidly decay to zero. Hence, the wavelet transforms give information about the details of f at different scales : each scale is sensitive to the variations in frequency of this certain scale. This specificity will prove particularly useful when generalized to two-dimensional images.

Wavelet transforms preserve the information and can be inverted : $f = WT_\psi^{-1}\{WT_\psi\{f\}\}$.

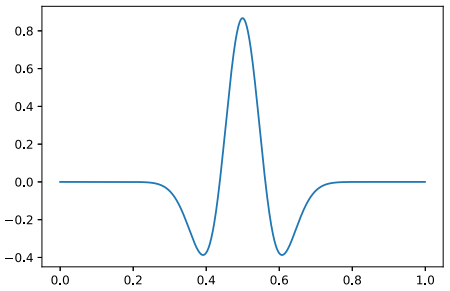

FIGURE 2.1: A classical example of a mother wavelet, the " Mexican hat ".

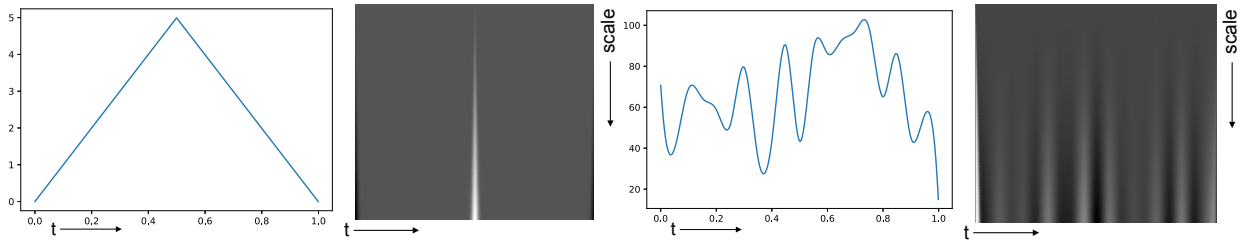

FIGURE 2.2: Two examples of functions and their wavelets transform for scales 1 to 10 obtained with the Mexican hat wavelet. The scale increases from top to bottom. Color bars were not added for clarity : the dominant grey corresponds to 0, lighter shades are positive and darker negative. We can see the wavelet coefficients are non-zero only where the original function's variating, i.e. where the, and only the concerned scales are sensitive to the variations. In the first example, the variation being infinitely small, it is apparent at every scale : even by zooming infinitely around the point of discontinuity of the derivative, this variation can still be seen. However, in the second example, the variations are smoother : if we zoom enough, the slope will appear to be constant. For that reason, the wavelet coefficients of the second example are only sensitive to the variations of certain scales : fast variations are already visible with coefficients of small scale, while slower variations only appear for largest scales.

2.1.2 Discrete wavelet transforms

Actual computations are made on discrete signals, so it appears necessary to discretize the wavelet transforms.

Let $f(t)$ be a continuous time signal uniformly sampled in N intervals over $[0,1]$. We note $f[n] = f(n)$ the signal of size $1/N$ on the n-th interval. By choosing a wavelet whose support is included in $[-K/2, K/2]$ we can define, for $2 \leq a^j \leq NK^{-1}$ a discrete wavelet scaled by a^j :

$$\psi_j[n] = \frac{1}{\sqrt{a^j}}\psi\left(\frac{n}{a^j}\right) \tag{2.6}$$

The discrete wavelet we obtain has Ka^j non-zero values on $[-N/2, N/2]$. The scale a^j must be larger than 2 to avoid the sampling interval being larger than the wavelet support.

The discrete wavelet coefficients can thus be defined :

$$w_\psi\{f\}(n, a^j) = \sum_{m=0}^{N-1} f[m]\psi_j[m-n] = f \star \overline{\psi}_j[n] \tag{2.7}$$

where $\overline{\psi}_j[n] = \psi_j[-n]$.

Summary :

- The wavelet transforms of a one-dimensional function give information about the regularity of this function at different scales.
- It is possible to discretize the wavelet transforms by considering only a discrete set of scales.

2.2 A particular case of two-dimensional wavelets

In this Section we will present the particular case of the starlet transform, that we will use later in the thesis. The passage from one to two dimensions in this particular case is made through the " à trous " algorithm that we will first describe.

2.2.1 The " à trous " algorithm

The " à trous " algorithm is based on a dyadic discrete transform, which means that we choose a equal to 2. The main idea of the algorithm is to build an undecimated wavelet transform : it keeps the set of coefficients w_j of the same size as the original signal for each scale, making it redundant (see Starck et al., 1998).

The " à trous " algorithm builds a sequence of approximations of an N-sized signal f_0 at increasingly larger scales $\{f_1, \cdots, f_J\}$. Each approximation is obtained from the previous one through a convolution with a mother wavelet filter $\bar{h}^{(j)}$ at scale $j+1$:

$$f_{j+1}[n] = (h^{(j)} \star f_j)[n] \tag{2.8}$$

the first approximation f_1 being a direct application of the filter $\bar{h}^{(0)}$ on the signal f_0.

According to the " à trous " algorithm, consecutive filters $h^{(j)}$ are obtained by adding zeroes between the nonzero filter elements so as to dilate the filter by a factor 2 from scale to scale.

The set of wavelet coefficients w_{j+1} at scale $j+1$ are then defined as the difference between consecutive large-scale approximations :

$$w_{j+1}[n] = f_j[n] - f_{j+1}[n] \tag{2.9}$$

Note that the details at scale $j+1$ are obtained by subtracting the smoothed approximation f_{j+1} from the approximation f_j. This way, only the structures that disappeared in the smoothing at scale $j+1$ are kept in w_{j+1}.

This eventually yields a decomposition of the signal f_0 into $W = \{w_1, ..., w_J, f_J\}$. The last set of coefficients f_J contains all the information that was left over by the precedent scales coefficients. It is named the " coarse scale ".

The reconstruction of the initial signal f_0 is then obtained by a simple coaddition of all wavelet scales and the final smooth subband :

$$f_0[n] = f_J[n] + \sum_{j=1}^{J} w_j[n] \tag{2.10}$$

This algorithm can easily be generalized to two-dimensional images, as we will see with the starlet transform.

2.2.2 The starlet transform

The starlet transform is a special case of bi-dimensional wavelets, which has been specifically designed to efficiently represent isotropic structures in images. Therefore, this particular case of wavelets has been proved to be well-adapted to analyze astrophysical images.

The starlet transform uses a two-dimensional version of the " à trous " algorithm. Here, we note c_0 the original image of size $N * N$. The approximations at increasingly larger scales are noted $\{c_1, \cdots, c_J\}$ and obtained thus :

$$c_{j+1}[k,l] = (h^{(j)} \star c_j)[k,l], \tag{2.11}$$

where the filter $h^{(0)}$ is defined as :

$$h^{(0)} = \frac{1}{256} \begin{pmatrix} 1 & 4 & 6 & 4 & 1 \\ 4 & 16 & 24 & 16 & 4 \\ 6 & 24 & 36 & 24 & 6 \\ 4 & 16 & 24 & 16 & 4 \\ 1 & 4 & 6 & 4 & 1 \end{pmatrix} \tag{2.12}$$

and the consecutive filters $h^{(j)}$ are obtained by adding zeroes between the nonzero filter elements, just as in the precedent Section (see Starck et al., 2015).

The wavelet coefficients at scale $j+1$ are then defined as the difference between consecutive large-scale approximations :

$$w_{j+1}[k,l] = c_j[k,l] - c_{j+1}[k,l] \tag{2.13}$$

This eventually yields a decomposition of the image c_0 into $W = \{w_1, ..., w_J, c_J\}$, where c_J is the " coarse scale ".

The reconstruction of the initial image c_0 is once again obtained by a simple coaddition of all wavelet scales and the final smooth subband :

$$c_0[k,l] = c_J[k,l] + \sum_{j=1}^{J} w_j[k,l] \tag{2.14}$$

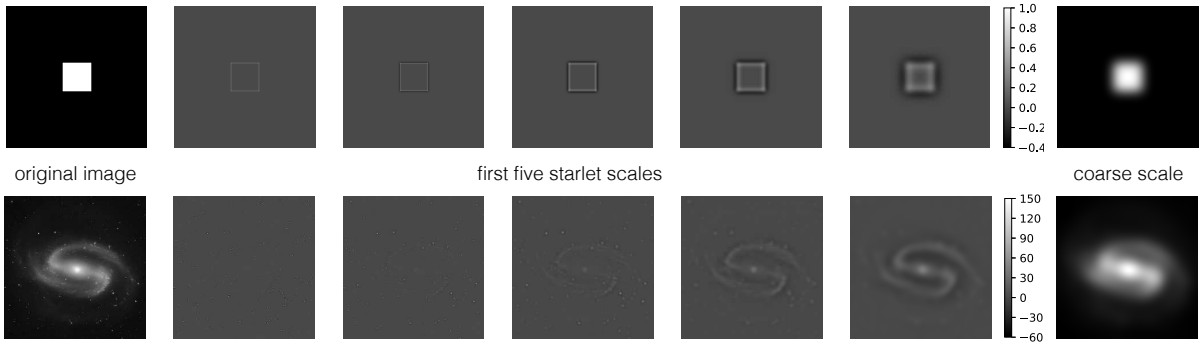

FIGURE 2.3: An image of a square and an astrophysical image and their starlet transforms in six scales. The colorbar is the same for the first five starlet scales. It highlights the fact that most wavelet coefficients are zero.

Summary :

- The starlet transform has been designed to efficiently represent isotropic structures in images.
- It transforms an image into a set of images of the same size, each representing details of a certain scale. The last image is named the " coarse scale " and contains all the information that was left over in the other scales.

2.3 Sparsity

One of the most interesting properties of two-dimensional wavelet transforms is their sparsity : most of the information is contained in a few coefficients (see Mallat, 2008).

Figure 2.3 shows that most of the coefficients in the three first scales of the four scales starlet transform of a square are zeros, for these scales only focus on the details of the image, here the edges. Hence, a few coefficients are sufficient to contain most of the useful information of the image, while the coarse scale (the last scale) contains what is left.

Thus, the scales before the coarse one contain mainly information about the different features in the image. The last one, from which details such as edges have been removed, consists in a blurred version of the original image and is useful to reconstruct it. For that reason, the sparsity of wavelets transforms is an essential

property that makes at the same time the information contained in a restrained number of coefficients and separates it into different subsets. The way details of different sizes are taken into account depends on the chosen wavelet. A “ well chosen ” wavelet regarding a certain image would be one sensitive to the details of different kinds and shapes in the image.

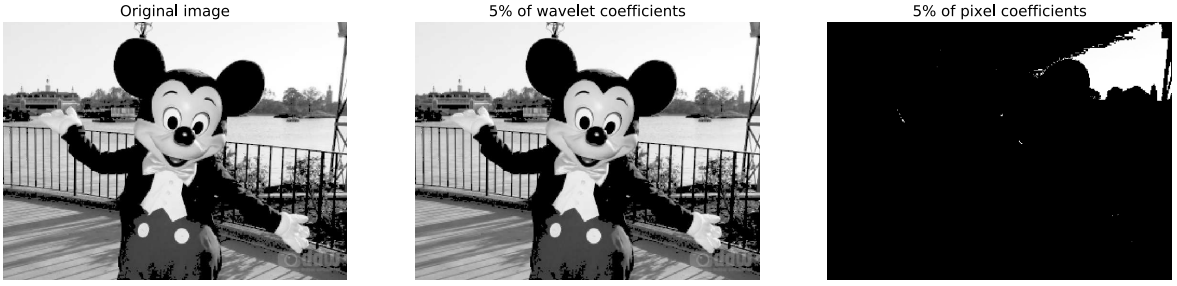

FIGURE 2.4: An image compared with its reconstruction using only the brightest 5% of all wavelet coefficients and using only the brightest 5% of pixel coefficients.

A good example of the usefulness of this sparsity can be found in the fact that the *JPEG 2000* image compression standard is using wavelet transforms to keep only the most important coefficients without losing too much in quality. Figure 2.4 shows that well chosen wavelet transform can be used to obtain an accurate compression of an image using only the brightest 5% of its coefficients.

Summary :

- Wavelet transforms can give sparse representations of an image : most of the information is contained within a few coefficients.
- The wavelet coefficients of a certain scale contain only information about this specific scale.
- The last scale, or “ coarse scale ”, contains the information that was left over in the other scales. It consists in a blurred version of the original image, from which details such as edges have been removed.
- A “ well chosen ” wavelet is sensitive to the details of different kinds and shapes in the image. The starlet transform is designed to efficiently represent isotropic structures in images, so it is well-adapted to analyze astrophysical images that may contain structures of highly different shapes.

2.4 An application of wavelet transforms : inpainting

Inpainting is a process whose aim is to restore damaged or missing parts of an image. Historically, the term designed the methods used to reconstruct deteriorated parts of an artwork. It implied the intervention of an art conservator using their knowledge to determine the mediums and techniques to employ to best fit the original piece and accurately fill the missing parts.

With the development of digitalization, the term evolved to englobe image processing methods automatizing the reconstruction of missing and damaged parts of a digital image. These methods use the information contained in the zones surrounding the parts to replace in order to recreate an estimation of these parts.

Inpainting methods can be seen as interpolation methods in two dimensions : they reconstruct missing parts of an image using the information contained in the surroundings.

Wavelet transforms can be used in inpainting methods : the implementation we describe here is from Cai et al. (2008), but there are numerous examples of similar inpainting methods (e.g Shen et al., 2016; Fadili et al., 2007b). The sparse representation wavelet transforms give of a given image allows to develop an iterative algorithm reconstructing the missing parts Δ of an image defined on a set Ω. If we name f the original complete image on Ω and g the observed image, corrupted on Δ, our aim is to obtain an approximation $\tilde{f}$ of f such as $\tilde{f} = g$ on the good parts $\Omega \backslash \Delta$ and $\tilde{f}$ as close as possible to f on the missing parts Δ.

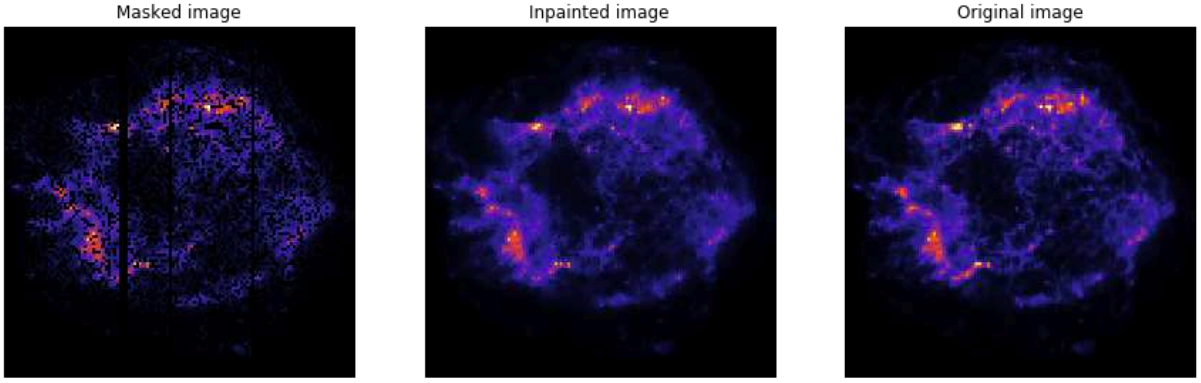

FIGURE 2.5: An example of a masked image reconstructed using a wavelet transforms based inpainting method.

To do so, we can start with an initial guess $\tilde{f}_0$ and iteratively redefine $\tilde{f}_n$ such as :

- $\tilde{f}_{n+1} = g$ on the good parts $\Omega \backslash \Delta$
- $\tilde{f}_{n+1} = WT_\psi^{-1}\{\mathcal{T}(WT_\psi\{f_n\})\}$ on the missing parts Δ

where WT_ψ is a well chosen wavelet transform representing f sparsely and $\mathcal{T}$ a threshold operator. This operator plays two important roles : it removes noise from the image and it disturbs the coefficients $WT_\psi\{f_n\}$ so that the information contained in the $\Omega \backslash \Delta$ region can permeate in the Δ region from an iteration to another. The sparsity also ensures the thresholding not to be too destructive. Figure 2.5 shows an example of a result obtained thanks to an inpainting method using wavelet transforms.

Summary :

- Wavelet transforms can be used in inpainting methods, the sparsity they provide in their representation being useful to reconstruct missing parts of an image.

CHAPTER 3

GMCA

3.1 Blind source separation methods

Separating a set of components mixed in a data set without prior information is known in signal processing as a blind source separation (BSS) problem (see Comon & Jutten, 2010). There are plenty of fields and plenty of data types that present BSS problems. A simple example can be found in music processing : with only a single audio file of a song, how can we extract the voice of the singer from the instruments ? The nature of the data and the reason why you want to extract a part of it may change, the algorithms that could successfully do it may be different from a case to another, but the main principle of BSS problems is still the same : extracting mixed sources from a data set.

In astrophysics, extracting components from a set of observed data can be helpful to study each component individually, thus leading to a better understanding of them. In the context of X-ray studies in particular, the input is a data cube (E, x, y), where E is the spectral dimension and x and y are spatial dimensions. Thus, BSS methods can be used on X-ray data to disentangle emitting components spatially and spectrally to provide morphological and spectral information without imposing any prior physical model that would constraint the results.

BSS methods do not rely on any physical model as they do not need any prior information to extract components from a data set, apart from the assumption that given an appropriate criterion, the components will be different enough to be disentangled. They only rely on the data itself, trying to exploit to the maximum the information therein. There are different ways to retrieve this information, the Independent Component Analysis (ICA) for example, intoduced by Comon (1994), postulates that the sources to disentangle are statistically independent : they should not share simillar structures one with another. Another way to do so, is to look at the original data in a mathematical space where the sources will be sufficiently different from one another. The concept of sparsity helps to determine what kind of space could be suitable : a sparse signal is a signal in which most of the coefficients are zero. Thus, two sparse signals will be easier to disentangle as their signatures will not be correlated. For example, to separate periodic signals in a unidimensional data set, it is much easier to work in the Fourier space, where such sources will be entirely determined by a few coefficients (see Figure 3.1). This idea of a sparse BSS was introduced by Zibulevsky & Pearlmutter (2001), and constitutes the basis of our method.

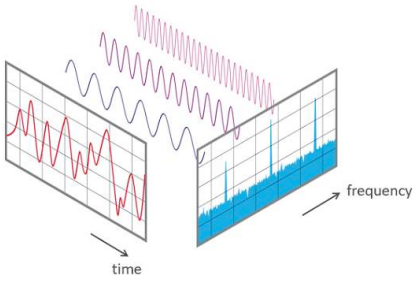

FIGURE 3.1: To disentangle mixed periodic signals from a one dimensional data set, it is simpler to consider the Fourrier transform of the data.

Summary :

- Blind source separation (BSS) methods aim to disentangle components in a data set without any prior information.
- They classically rely on a sparse mathematical representation of the input data set.
- In the context of X-ray studies, the input is a data cube (E, x, y).

3.2 Introduction to GMCA

In this thesis we introduce a new method to disentangle spectral components from X-ray data of extended sources. Our method is based on an algorithm that uses the ability of wavelets to provide a sparse representation for astrophysical images to find a solution to BSS problems. This algorithm, the Generalized Morphological Components Analysis (GMCA), was first developed by Bobin et al. (2015), and has recently been applied to *Planck* survey data to separate the image of the Cosmic Microwave Background (CMB) from the foregrounds (Bobin et al., 2016).

Planck data consist in (E, x, y) cubes, exactly like in X-rays, and separating the CMB from the foregrounds is a similar problem as extracting emitting components from X-ray data. For that reason, applying GMCA to X-ray data would be logical to solve BSS problems in X-rays. However, this application is non-trivial. While in *Planck* the data are obtained in nine fixed frequencies, X-ray photons can be binned into an arbitrarily large number of energy bins ; the X-ray photon count is drastically lower at high energies, and has higher dynamic range. In addition, X-ray data have Poisson noise whereas the GMCA method assumes an additive Gaussian noise. This last issue is the most problematic one, and will be further addressed in the following of this thesis.

Summary :

- GMCA is a BSS algorithm first developed to extract the CMB from the foregrounds in *Planck* data.
- *Planck* and X-ray data being similar, GMCA could be applied on X-ray data cubes.
- Some differences make it non-trivial : the higher number of energy bins, the drastically lower photon count at high energies and the higher dynamic range in X-ray as compared to *Planck* data.

3.3 Description of the method

The input of GMCA is a data cube (E, x, y). In the absence of prior physical information, the nature of the data is irrelevant, as long as it is a cube of that kind : it can be radio data, X-ray data or anything else, the algorithm will treat it in the same way. GMCA needs to consider this 2D-1D data cube as the product

between an image and a spectrum. This is a strong hypothesis, but it is consistent with the nature of our data.

The main concept of GMCA is to take into account the morphological particularities of each component in order to disentangle them. Apart from the (E, x, y) data cube, the only input needed is the number n of components to retrieve, which is user-defined. To optimize the disentangling process, the signal is projected into a space where it will have a sparse representation. Thus, two components that are sufficiently different spatially will have few coefficients in common, allowing us to separate them more easily. In the case of images, the equivalent of the Fourier space would be a correctly chosen wavelet transform, that would concentrate most of the image information into a few coefficients (see Section 2.3).

Summary :

- GMCA is a BSS algorithm taking a data cube (E, x, y) as an input.
- It does not need any prior physical information. It only needs an input data cube and the number n of components to retrieve, that is user-defined.
- It uses the sparsity of a correctly chosen wavelet transform to take into account the morphological particularities of each component to disentangle.

3.4 Mathematical formalism

Here we will use the undecimated starlet transform (see Starck et al., 2007, and Section 2.2.2) which is well suited for astronomical purposes. Each wavelet scale contains information about structures of a specific size, which allows us to isolate more easily the morphological features of each component. In order to minimize cross-correlations between components, the two largest wavelet scales are not used, because in these scales morphological features are harder to differentiate.

For a data cube of dimension (E, x, y), we apply a wavelet transform with J scales on the images of each energy slice, J being chosen so that a there is a sufficient number of wavelet scales to separate details of different scales. The " à trous " algorithm giving information on details of a typical size of 2^j at the j-th scale, J must also be chosen so that 2^J does not exceed the sizes of x and y. We also remove the two largest scales, where the structure are too large for a proper discrimination between components. Hence, we obtain an array X of dimension $(E, x, y, J-2)$. We note that the wavelet transform is applied only on images, and that there is no constraint on the sparsity of the spectra. The aim of GMCA is to solve the following problem :

$$X = AS + N = \sum_{i=1}^{n} A_i S_i + N \tag{3.1}$$

where n is the predefined number of components, the A_i are vectors of size E, in our case related to the spectral information (the spectra of our mixed components), the S_i are the sources represented in wavelets, of dimension (x, y, J) and related to the spatial information (the images in wavelets of our mixed

components), and N is a Gaussian noise. The product here for a given i is the multiplication of every coefficient of A_i by every coefficient of S_i. The components to retrieve are assumed to be modeled as the product of an image (S_i in the wavelet space) and a spectrum (A_i). Thus, the retrieved components are approximations of the actual components with the same spectrum on each point of the image. This problem being an ill-posed inverse problem, as both A and S are unknown, one needs a constraint to solve it.

The GMCA algorithm relies on the assumption that, once the image has been translated into wavelet space, each constituent can be sparsely represented, thus making the component separation easier.

GMCA solves the inverse problem by imposing a sparsity constraint : it maximizes the sparsity of the images of each source in the wavelet domain. The problem being actually solved by GMCA is thus the following optimization problem :

$$\min_{A,S} \sum_{i=1}^{n} \lambda_i \|S_i\|_p + \|X - AS\|_F^2 \tag{3.2}$$

where λ_i are regularization coefficients equivalent to thresholds that aim at rejecting noise samples, and prove essential to provide robustness with respect to noise. They are chosen thanks to an estimation of the noise level in the sources based on the Median Absolute Deviation (MAD)[1] method, and progressively decrease towards the final user selected signal to noise level. More precisely, the λ_i are calculated at each step thanks to a weight matrix W (see the pseudo-code in the Part II of Bobin et al., 2015). $\|.\|_F$ is the Frobenius norm defined by $\|Y\|_F^2$ =Trace(YY^T) and $\|.\|_p$ is a l_p norm, with $p = 0$ or $p = 1$. The l_1 norm is defined by $\|Y\|_1 = \sum_{i,j} |Y_{i,j}|$ and $\|Y\|_0$ counts the number of non-zero entries in Y. The l_0 norm is the most adapted to evaluate the sparsity of signals, but it is not convex. The l_1 norm being convex and close to the l_0 norm, it can be used as well, the convexity being an advantage for the optimization problem. The first term of this equation is a sparsity constraint term and the second is a data-fidelity term.

More precisely, GMCA is an iterative algorithm repeating the following two steps :

- Step 1 : Estimation of S for fixed A, by simultaneously minimizing $\|X - AS\|_F$ and the term enforcing sparsity in the Wavelet domain ;
- Step 2 : Estimation of A for fixed S by minimizing $\|X - AS\|_F$.

Summary :

- The GMCA algorithm relies on a linear mixing model : the original data cube is supposed to be a sum of images S_i multiplied by spectra A_i, plus some Gaussian noise. Each component to retrieve is completely described by S_i and A_i.
- The different S_i and A_i are iteratively retrieved by constraining the sparsity of the starlet transforms of the images S_i, enforcing the morphological diversity.

[1] For a univariate data set $X_1, X_2, ..., X_n$, the MAD is defined as : $MAD = median(|X_i - median(X_1, X_2, ..., X_n)|)$

3.5 Application of the method

When GMCA was applied to *Planck* data, its original purpose, the CMB spectrum was fixed to its theoretical shape. Giving a known spectrum as additional information fixes a column in A, making the algorithm work in what is termed a *semi-blind* mode. However, if the theoretical spectrum is not previously known, the algorithm can also work in a completely *blind* mode. With our toy model example described in the next Chapter, we will test both of these modes.

The only input needed is the number n of components to retrieve. Any prior knowledge of the data can help to choose n wisely, as the expected number of components visible in the energy band on which GMCA is applied. In addition, this algorithm is running fast (a few minutes to extract sources from a 200*200*300 single core personal computer), so we highly recommend trying different values of n and checking if the outputs may have a physical relevance : as we will see in Section 4.2, GMCA does not produce images of spurious structures.

The outputs of GMCA are an array of dimension (n_E, n) containing the spectral information of the components, and an array of dimension (n, n_x, n_y) containing the spatial information of the components. In order to obtain n normalized cubes of dimension (E, x, y) we multiply each spectrum by its associated image. By collapsing these cubes along the E axis, images of the retrieved sources can be obtained, and by collapsing them along the x and y axis we can obtain their spectra. The spectra can subsequently be used in `Xspec` or a similar analysis tool in order to fit physical models and retrieve physical parameters (see Section 4.3).

Summary :

- GMCA has a *semi-blind* mode in which a spectrum can be fixed, if previously known.
- It is a fast-running algorithm.
- The outputs of GMCA are an array of dimension (n_E, n) containing the spectral information of the components, and an array of dimension (n, n_x, n_y), where the number n of components to retrieve is user-defined.

3.6 Questions raised by the application of GMCA

There are a few questions that the use of the GMCA algorithm on real data raise. The first, and most obvious one, being : how can we know that the output results are physically significant, while there is no prior physical information needed ?

The number n of components to retrieve, that is user-defined, also appears to present a technical issue : how can we choose n in the most accurate way ?

Lastly, GMCA being a non-linear algorithm, there is no trivial way to retrieve errors or confidence ranges associated to its results. How could we obtain them ? In addition to the intrinsic values of an estimation of the errors, they would be necessary to use analysis tools such as `Xspec` on the retrieved components.

In the first part of this thesis, we will examine these questions and propose elements of response.

Summary :

- How can we know that the output results are physically significant, while there is no prior physical information needed ? See Section 4.7.
- How can we choose the number of components to retrieve in the most accurate way ? See Section 4.7.
- How could we obtain errors or confidence ranges ? See Chapter 6.

CHAPTER 4

METHOD PERFORMANCES

The GMCA algorithm was originally developed to be applied on *Planck* radio data. Even if the cubic nature of these data is similar to that of X-ray data cubes produced by *Chandra* or *XMM-Newton*, we need to estimate the performances of the method before applying it on real data and interpreting the results. As there is not any theoretical proof of the convergence nor any a priori knowledge about the reliability of the results (Bobin et al., 2015), we test empirically the algorithm on toy models specifically designed to resemble SNRs real X-ray data. This chapter presents the study published in Picquenot et al. (2019).

4.1 Toy model Definition

To test the performance of GMCA in disentangling components in X-ray data, we designed toy models inspired by real X-ray observations of SNRs. We chose to simulate a SNR similar to Cassiopeia A, one of the best-studied SNR, that has benefited from deep megasecond observations.

Our toy models consist of a data cube composed of the sum of individual components to which we add Poisson noise. Each component comprises an image multiplied by a spectrum (see Figure 4.1). The images were obtained by applying GMCA to real *Chandra* data from Cassiopeia A (see Section 4.6), and smoothing the output to mitigate the noise. For now, the relevance of these images is not important : we only want to ascertain if, when the components are known, GMCA is able to disentangle them when mixed together. The spectra we use are the theoretical spectra folded through the *Chandra* instrument response ; the energy binning is 43.8 eV (three times the native energy channel width), and the pixel size is 1.8 arcsec (four times the native pixel size). We also add a constant image associated with the instrumental background[1] to better simulate observed data. We do not add a cosmic X-ray background, because this background being isotropic at the scale of Cassiopeia A, its spatial template would be a constant image. Thus the addition of a cosmic X-ray background and the instrumental background would only end up being one component, with a slightly different spectrum. Finally, we generate Poisson noise. In this study we begin by focusing on two

	Description	Parameters
Model 1	Power Law + Gaussian	$\Gamma = 2.0$ $E_c = 6.58$ keV $\sigma = 80$ eV
Model 2	Power Law + Apec	$\Gamma = 2.0$ $kT = 2$ keV
Model 3	Power Law + Two Gaussians	$\Gamma = 2.0$ $E_{c1} = 6.55$ keV $E_{c2} = 6.64$ keV $\sigma = 0$ eV
Model 4	Power Law + Two Apecs	$\Gamma = 2.0$ $kT_1 = 2$ keV $kT_2 = 0.5$ keV

TABLE 4.1: Description of the toy models. For all models, $N_{\rm H}$ is set to $N_{\rm H} = 0.5 \times 10^{22}$ cm^{-2}. For the thermal model (*apec)*, the ionization timescale is set to $\tau = 1 \times 10^{10}$cm^{-3}s and the abundances to solar values.

[1]Derived from closed/stowed observations available at : http://cxc.harvard.edu/ciao/download/caldb.html

typical observational scenarii (see Table 4.1) : synchrotron continuum emission entangled with line emission (Model 1), and synchrotron continuum emission entangled with thermal emission (Model 2). In both models, we set the synchrotron emission as one with the highest total number of counts.

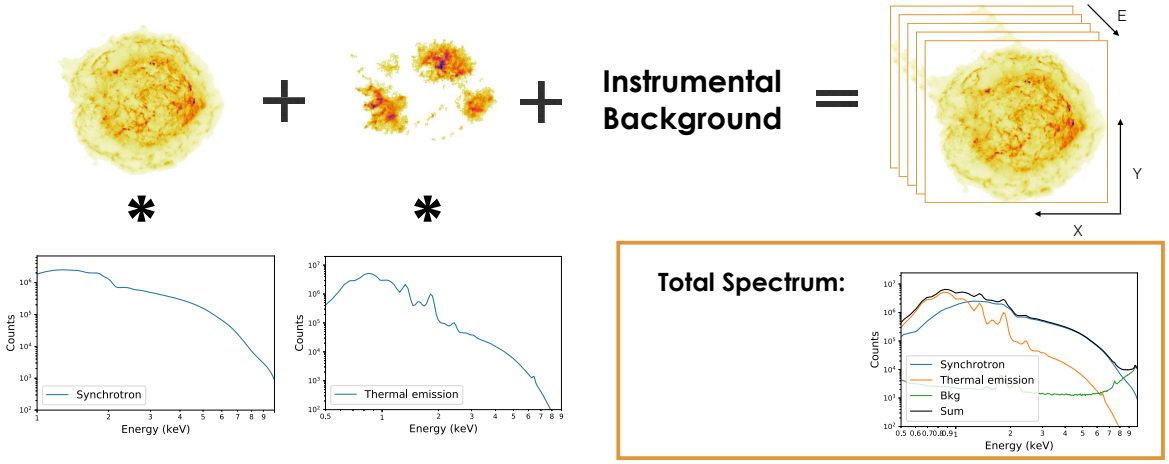

FIGURE 4.1: A presentation of our toy model, consisting in the sum of images multiplied by theoretical spectra. The spatial distribution of the instrumental background is uniform.

Models	Model 1	Model 2	Model 3	Model 4
Comp.	E_c	kT	E_{c1}	kT_2
Ratios	6.2 - 7 keV	0.5 - 8 keV	6.4 - 7 keV	0.5 - 4 keV
13.35	4.20	2.39	4.36	1.67
8.90	2.80	1.59	2.91	1.11
5.93	1.86	1.06	1.93	0.74
3.95	1.24	0.71	1.29	0.50
2.64	0.83	0.47	0.86	0.33
1.76	0.55	0.31	0.57	0.22
1.17	0.37	0.21	0.38	0.15
0.78	0.25	0.14	0.26	0.098
0.52	0.16	0.093	0.17	0.065
0.35	0.11	0.062	0.11	0.043
0.23	0.073	0.041	0.076	0.029
0.15	0.049	0.028	0.050	0.019
0.10	0.032	0.018	0.033	0.013
0.069	0.0022	0.012	0.022	0.0086
0.046	0.0014	0.0082	0.015	0.0057

TABLE 4.2: Equivalence between the ratios Max(Fe or Thermal emission)/Synchrotron and the physically more significant flux ratios for our four toy models. The components are named after their main characteristic (E_c for the gaussians, kT for the thermal emissions), as they are listed in Table 4.1. The energy ranges listed below each component are those on which the ratios are calculated.

The results of our method depend on the relative level of Poisson noise, hence of the total number of counts in the signal. This parameter is thus chosen in order to reflect the reality of the data we get from spectro-imaging instruments. Hence we set the count rate of the synchrotron and line or thermal emission to be of the order of that observed in Cassiopeia A. We then simulated two datasets, corresponding to a 1 Ms or a 100 ks observation with the *Chandra* ACIS-S instrument.

The ratio between the strength of the main component compared to that of the secondary component is also an essential factor. For Model 1, we define this as the Fe Line/Synchrotron ratio at 6.58 keV (the peak of the Gaussian) ; for Model 2, it is defined as the Thermal emission/Synchrotron ratio at 0.85 keV. We progressively decrease the contrast of the second component relative to that of the synchrotron emission following 15 ratios.

For both toy models we tested the same ratios. Table 4.2 presents a conversion table between these ratios and the Fe Line/Synchrotron flux ratios between 6.2 and 7 keV, or the Thermal emission/Synchrotron ratio in the $0.5 - 8$ keV band.

Summary :

- To test the performances of GMCA, we designed toy models inspired by real X-ray observations of SNRs.
- Our first toy model is a synchrotron emission associated to a line emission, with instrumental background and Poisson noise. We generate 15 versions of this toy model with the normalization of the gaussian line varying while the synchrotron emission keeps the same normalization.
- Our second toy model is a synchrotron emission associated to a thermal emission, with instrumental background and Poisson noise. We generate 15 versions of this toy model with the normalization of the thermal emission varying while the synchrotron emission keeps the same normalization.

4.2 Reconstructed image fidelity

To assess the accuracy of the results of GMCA, we compared both the similarities between the input and the output images, and the reliability of the spectral parameters fitted. For the image benchmarks, we used the Structural Similarity Index (SSIM, see Wang et al., 2004), which measures the perceived similarities between two images by incorporating the idea that close pixels have strong interdependencies, instead of solely measuring absolute differences. It is appropriate for us as we are interested in evaluating how much the ouput images look like the input ones " to the naked eye ". This index takes the form of a number between 0 and 1, 1 being a perfect resemblance and 0 indicating perfect dissimilarity, and is computed by comparing the images on various windows in order to take into account the structural similarities. In our case, below an SSIM of 0.75 we can consider that the source has not been retrieved, the remaining correlations being linked to the similarities between the synchrotron image, the Fe image and the Poisson noise associated to them.

For each line/continuum emission ratio we then performed a Monte-Carlo simulation of a hundred different Poisson realizations to test the robustness of the algorithm. We compared the results of GMCA in pure blind mode with that of GMCA in semi-blind mode, with the

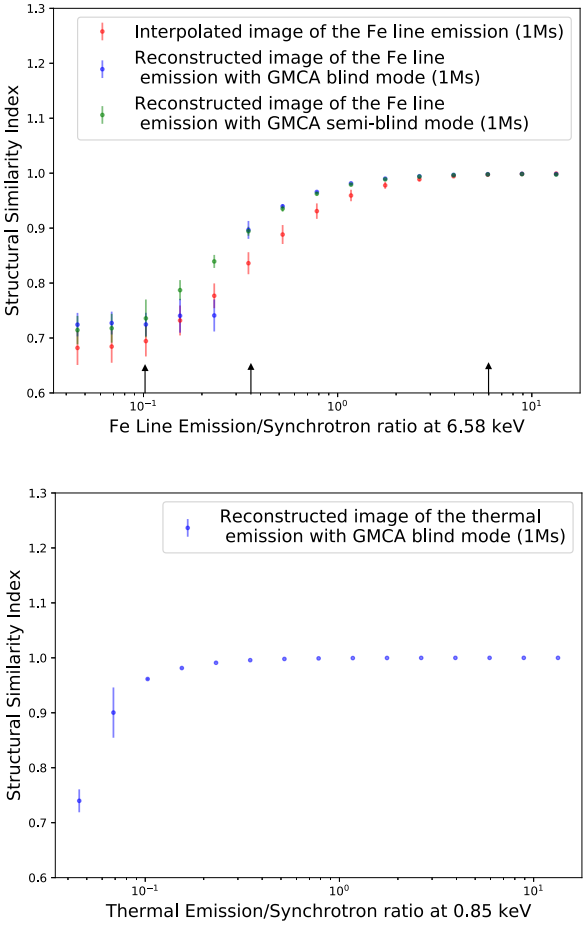

FIGURE 4.2: SSIM coefficients of the input and output images found by GMCA for a total number of counts corresponding to a 1 Ms observation. The points are the average of all Monte-Carlo realizations at a particular ratio, and the error bars the standard deviations of these realizations. On top, a comparison of the image quality obtained in retrieving the Fe structure in our first toy model for different ratios Line emission/Synchrotron, between an interpolation method, a GMCA in blind mode and a GMCA in semi-blind mode. Some images corresponding to the ratios indicated by arrows are shown in Figure 4.4 On the bottom, the image quality of the thermal emission structure retrieved for different ratios by a GMCA in blind mode.

theoretical shape of the Fe line fixed. We also compared these results to that of an interpolation method between 6.1 and 7.1 keV (Figures 4.2, top and 4.3, top show the results for the simulated 1Ms and 100 ks observations, respectively). This method consists of estimating the underlying synchrotron spectrum between 6.1 and 7.1 keV by interpolating it. The synchrotron image is then determined by integration (for example between 5 and 6 keV, where the Fe is absent) and the synchrotron cube is obtained by multiplying this image and the interpolated spectrum. Then, we subtract the aforementioned cube. The synchrotron-subtracted remaining cube then constitutes an estimation of the Fe structure.

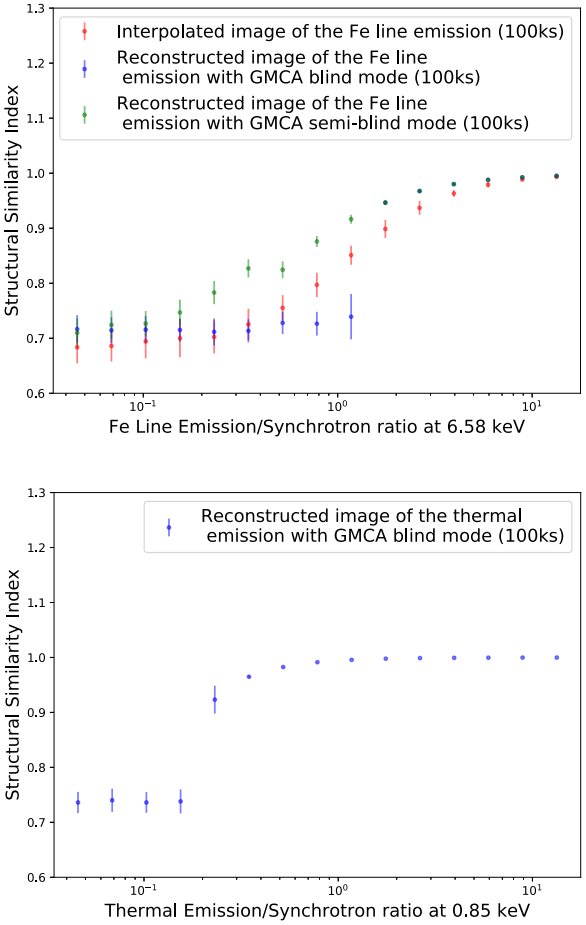

FIGURE 4.3: SSIM coefficients of the input and output images found by GMCA for a total number of counts corresponding to a 100 ks observation. The points are the average of all Monte-Carlo realizations at a particular ratio, and the error bars the standard deviations of these realizations. On top, a comparison of the image quality obtained in retrieving the Fe structure in our first toy model for different ratios Line emission/Synchrotron, between an interpolation method, a GMCA in blind mode and a GMCA in semi-blind mode. On the bottom, the image quality of the thermal emission structure retrieved for different ratios by a GMCA in blind mode.

For both simulated exposures, we see that Fe Line/Synchrotron ratios images given by GMCA have slightly better SSIM coefficients to those obtained with an interpolation method. However, a sudden drop in GMCA results points out the moment when the algorithm in blind mode is no longer able to find the Fe structures. The descent is smoother with a fixed spectrum (semi-blind mode) because the algorithm is given more information to search for potential sources, but as the number of counts in the iron line decreases the noise increases. In blind mode, GMCA retrieves an image of the Fe spatial structure when it is up to 2.9 times weaker than the synchrotron in the case of a total number of counts corresponding to a 1 Ms observation (9 times weaker in flux), and up to 1.8 times higher than the synchrotron for 100 ks (1.8 times weaker in flux).

GMCA in blind mode does not benefit from the information that the Fe line is contained between 6.1 and 7.1 keV, still gives great results. Furthermore, the interpolation method cannot be used on components whose spectra are extended on an energy range that is too wide, as we will see with our second toy model. Also, we will see in Section 4.6 that with real data, what looks like a Gaussian can contain some hidden information that a GMCA in blind mode will be able to retrieve, but an interpolation can only find the Gaussian as a whole.

The fact that GMCA gives good images until it is suddenly unable to find anything but noise suggests that the algorithm can be trusted : in this particular test the Fe distribution is found or is not, but the algorithm never gives images of spurious, over-interpreted structures (see Figure 4.4 for an example of images becoming noisier as the component becomes fainter). In our test case, when we increase the number of sources, the first two remain the synchrotron and Fe structure, the rest are only noise. As our data are Poissonian, the noise component has a shape similar to that of the main component, here the synchrotron, with large fluctuations.

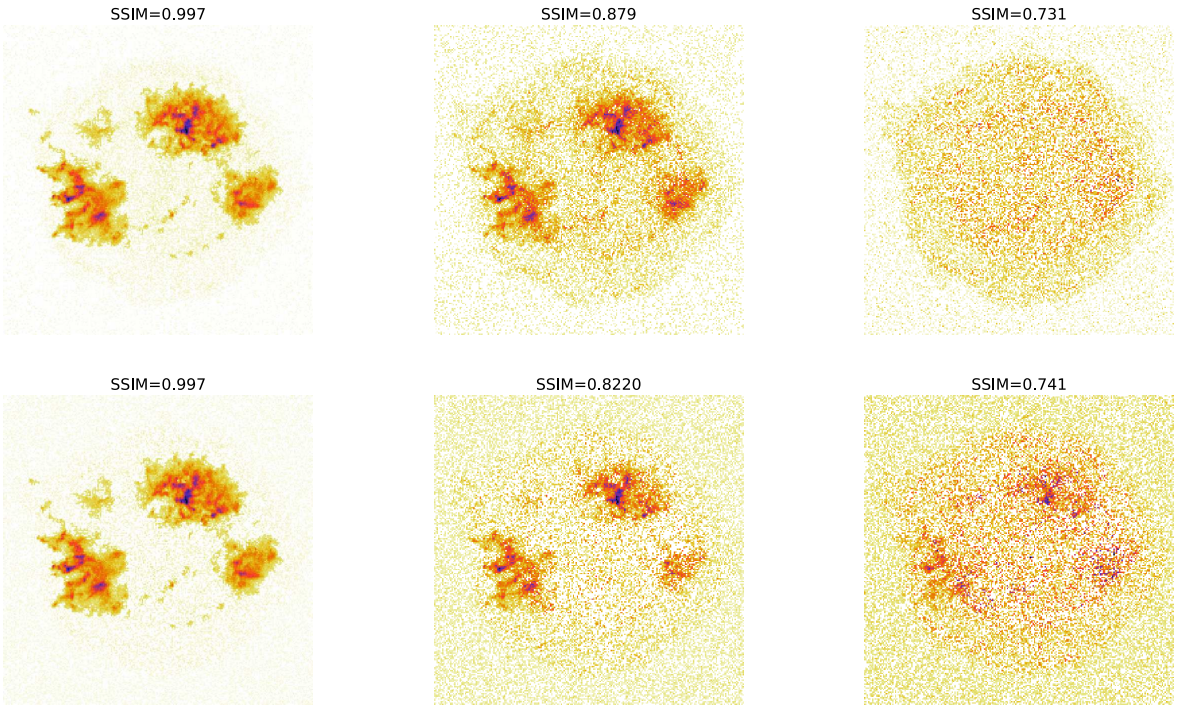

FIGURE 4.4: Images of the Fe spatial structures in our first toy model as found by GMCA without fixing the Fe spectral shape (on top) and by an interpolation method (below) for the three ratios Fe Line/Synchrotron marked by arrows in Figure 4.2). The SSIM coefficients are written on top of the images. Coefficients under 0.75 describe images where the Fe structures are not recognizable, but the SSIM is still high because of the similarities between intrinsic Fe and synchrotron distributions. The color scale is in square root.

We proceeded in the same way with our second toy model, featuring a synchrotron continuum emission and a thermal emission (see Figure 4.2, bottom panel for the simulated 1Ms observation and Figure 4.3, bottom panel for the 100 ks one). Here, the comparison with an interpolation method is impossible, for the thermal spectrum cannot be subtracted from the synchrotron with a simple interpolation. GMCA in semi-blind mode does not make sense either, because with real data it would be impossible to know the shape of a thermal emission a priori. With a total number of counts corresponding to a 1 Ms observation, GMCA in blind mode applied from 0.5 to 10 keV is able to retrieve an image of the thermal emission spatial structure when this component is up to 14.6 times weaker than the synchrotron (83.3 times weaker in flux). With a total number of counts corresponding to a 100 ks observation, it could retrieve an image up to 4.3 times weaker than the synchrotron (13.7 times weaker in flux). The thermal emission in our second toy model can be retrieved with smaller ratios than the Fe line because it is non-negligible on a wider energy range, providing more counts to the algorithm.

We can note that the instrumental background was not retrieved, in any cases, and that it did not leak on any other component. This is due to the fact that the two largest wavelet scales being eliminated, the instrumental background, associated with a constant image, was automatically suppressed with it.

Summary :

- For both toy models, GMCA retrieves accurate images even for low Fe Line/Synchrotron or Thermal/Synchrotron ratios.
- GMCA gives good images until it is suddenly unable to find anything but noise, suggesting that the algorithm can be trusted : in these tests the original distribution is found or is not, but the algorithm never gives images of spurious, over-interpreted structures.

4.3 Spectral fidelity

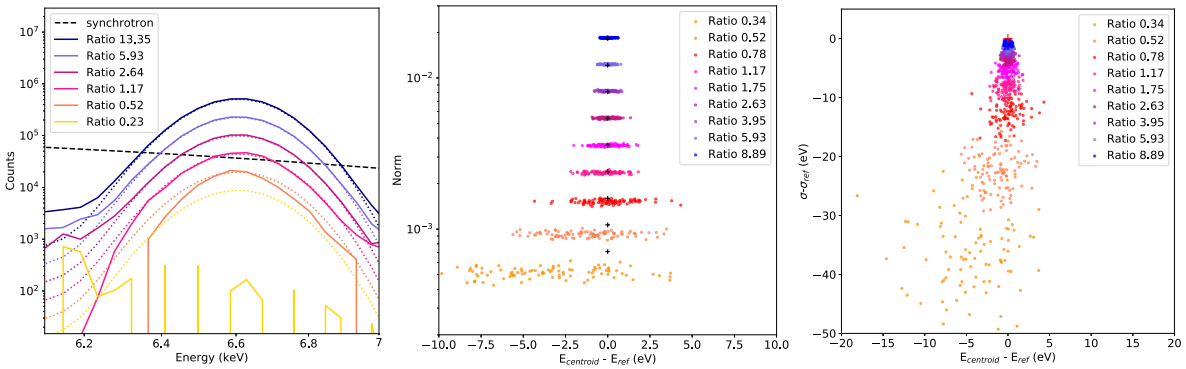

FIGURE 4.5: On the left, spectra retrieved by GMCA for different ratios Fe Line/Synchrotron in our first toy model with a total number of counts corresponding to a 1 Ms observation. In solid lines, the retrieved spectra. In dotted lines, the theoretical spectra. The synchrotron spectrum is displayed as an indication of the relative strengths. The two other plots represent parameters of the Fe K component retrieved by GMCA for a hundred realizations of each out of nine different ratios Fe Line/Synchrotron with a total number of counts corresponding to a 1 Ms observation. In the center, the retrieved E_c and norm. On the right, the retrieved E_c and σ. In both cases, the theoretical results are represented by crosses.

For every Fe Line/Synchrotron ratio for which the Fe K distribution is found by GMCA in blind mode, the retrieved spectrum is comparable to the input spectrum with some noise appearing as the Fe component becomes fainter (see Figure 4.5, left panel). Apart from a slight overestimation of the wings, the retrieved spectra are accurate and their normalizations well estimated.

In order to estimate more precisely the spectral accuracy of the method, we fitted the recovered spectra in the X-ray spectral fitting package `Xspec` [2] and compared the parameters thus obtained with a fit of the original data without GMCA processing directly in `Xspec`. Fitting the retrieved spectra requires to estimate the errors for every spectral bin. In spite of the fact that our input data are Poissonian, we cannot assume that the results given by GMCA will still be such. Therefore, we used the standard deviation of a hundred Monte-Carlo realizations as an estimation of the error.

We tested the accuracy of the spectra retrieved by GMCA in Model 1 by comparing their centroids, widths and normalizations to the theoretical ones (see Figure 4.5, central and right panels). The norms are almost perfectly retrieved (Figure 4.5, left and central panels), and even the slight energy shift for the smaller ones (around 5 eV) is negligible as compared to the instrument resolution, which is 150 eV (at 5.9 keV) for the

[2] https://heasarc.gsfc.nasa.gov/xanadu/xspec/

ACIS-S camera [3]. The wings are a little overestimated in the first norms (Figure 4.5, left panel), while the width σ is underestimated in the last ones (Figure 4.5, left and right panels). It may be due to the fact that in the fainter part of the Gaussian, the signal is largely dominated by the synchrotron, which makes the disentanglement harder than at the peak of the Gaussian.

We made the same comparison with the Gaussians recovered without using GMCA by fitting a power law and a Gaussian on the original spectra in `Xspec` (see Figure 4.7). The retrieved norms and centroids are a little more accurate (Figure 4.7, left panel), but quite similar to the results given after GMCA. However, the retrieved σ are not underestimated, they are still centered on the theoretical value for low ratios (Figure 4.7, right panel). Thus, GMCA introduces a bias in calculating some physical parameters in `Xspec`, but it is small compared to the 150 eV spectral resolution.

Finally, we tested the accuracy of the spectra retrieved by GMCA in our second toy model, featuring a synchrotron and a thermal emission (see Figure 4.6, top panel). The spectra are mainly well retrieved, even for low thermal emission/synchrotron ratios, but they are always overestimated at high energies. This reflects the fact that the synchrotron is contaminating the thermal emission : because of the spatial overlap between the two structures, there is a leakage from the main one into the weaker one when the number of counts is too low. This leakage impacts strongly the temperature retrieved after a fitting in `Xspec`, the necessary information being the slope at high energies. As shown in Figure 4.6, bottom panel, the overestimation of the spectra, bigger as the ratio decreases, is directly affecting the retrieved kT. However, kT is a global parameter, relying on the information contained over the full energy range, thus highly susceptible to be impacted by an overestimation at high energies. Local parameters, like N_{H} or τ, are almost perfectly estimated for thermal/synchrotron ratios as low as 0.52. For example, the theoretical N_{H} is equal to 0.5×10^{22} cm^{-2} ; for a ratio of 3.95 we retrieve $(0.490 \pm 0.001) \times 10^{22}$ cm^{-2} and for a ratio of 0.34, $(0.485 \pm 0.008) \times 10^{22}$ cm^{-2} where errors are the standard deviation on a hundred Monte-Carlo realizations. In the same way, the theoretical τ is 1×10^{10} cm^{-3} s ; for a ratio of 3.95 we retrieve $(9.13 \pm 0.05) \times 10^{9}$ cm^{-3} s, and for a ratio of 0.34, $(9.12 \pm 0.27) \times 10^{9}$ cm^{-3} s.

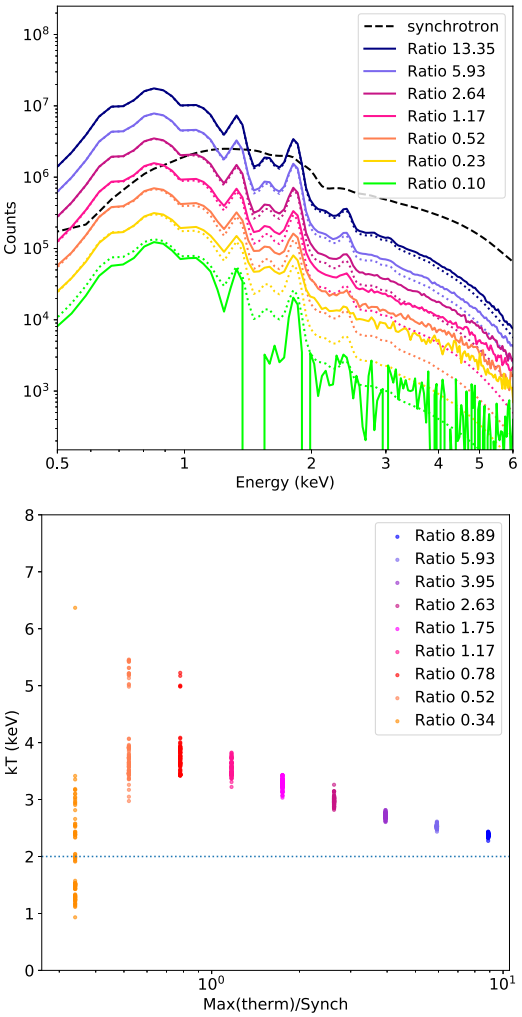

FIGURE 4.6: On top, spectra retrieved by GMCA for different ratios Thermal emission/Synchrotron with a total number of counts corresponding to a 1 Ms observation. In solid lines, the retrieved spectra. In dotted lines, the theoretical spectra. The synchrotron spectrum is displayed as an indication of the relative strengths. On the bottom, kT retrieved by `Xspec` by fitting a thermal model on the thermal emission spectra retrieved by GMCA for different ratios Fe Line/Synchrotron with a total number of counts corresponding to a 100 ks observation. For each ratios, we made a Monte-Carlo with a hundred realization, fitting in `Xspec` a thermal model on every realization associated with the error bars given by the Monte-Carlo. The theoretical kT is 2 keV and is indicated by the blue dotted line.

[3] http://cxc.harvard.edu/cal/Acis/

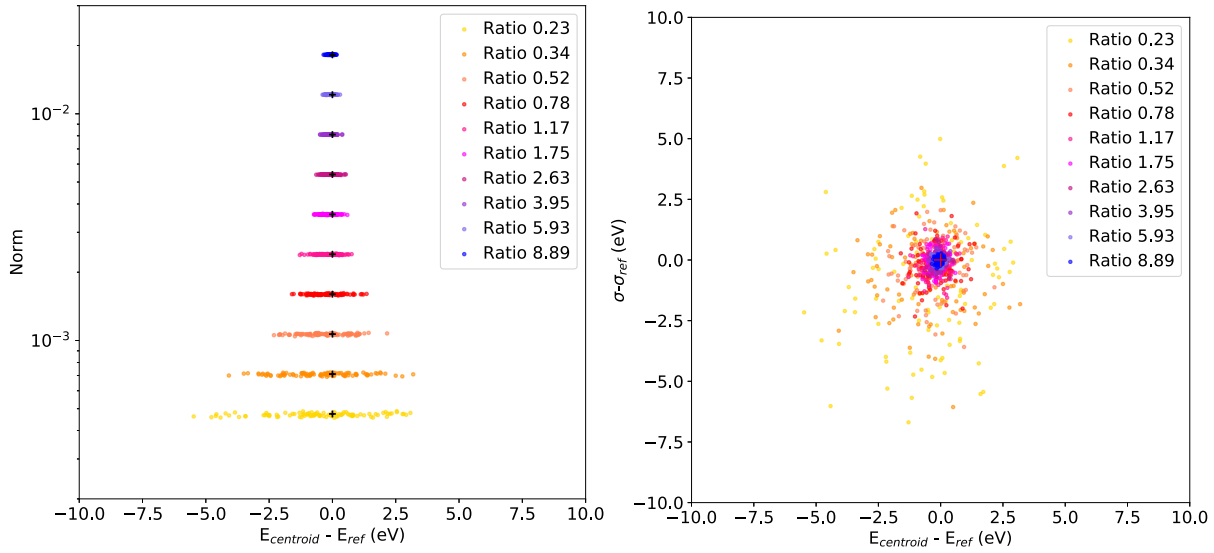

FIGURE 4.7: Parameters of the Fe K gaussian as retrieved by `Xspec` on our first toy model's total spectrum for a hundred realizations of each out of ten different Fe Line/Synchrotron ratios with a total number of counts corresponding to a 1 Ms observation. On the left, the retrieved E_c and σ. On the right, the retrieved norm and E_c. In both cases, the theoretical results are represented by black crosses.

Summary :

- The retrieved spectra and their fittings in `Xspec` are mainly accurate.
- For low Thermal/Synchrotron ratios in Model 2, the spectra are substantially overestimated, impacting their fittings in `Xspec`.
- This overestimation reflects the fact that the synchrotron is contaminating the thermal emission : because of the spatial overlap between the two structures, there is a leakage from the main one into the weaker one when the number of counts is too low.

4.4 Implementing a new inpainting step in GMCA

In this Section we will discuss the introduction of an extra step in the GMCA algorithm based on an inpainting method (see Section 2.4 for an introduction to inpainting methods using wavelets).

We previously saw that in the results given by GMCA on toy models composed of two physical sources there could be some leakage from the main component to the other one (e.g. leakage of the synchrotron component to the thermal component in Fig. 4.6). These leakages are often balanced by negative parts in the main component's image or spectrum. In order to correct that leakage, we added an extra step to GMCA.

GMCA being an iterative algorithm, our revised version retains a loop of about 150 iterations of the usual algorithm, followed by a smaller loop with a new step in which each result of the previous state is treated in a way to forbid negative values. To do so, a first method would be to define a mask where the reconstructed images take negative values, and apply those masks to the wavelet transforms of those images, S, imposing a 0 value on the negative parts before they are processed to estimate A. The results can be improved by replacing the raw masking by an inpainting, here a reconstruction of the masked parts of the image using a

wavelet transform (see Cai et al., 2008; Fadili et al., 2007a). We do this in order to constrain the algorithm to converge to a more physical solution.

Our new loop can be described thus :

- Step 1 : Estimation of S thanks to X and the previous A.
- Step 2 : Defining masks set to 0 where the reconstructed images are negative, indicating an area where strongly correlated components are overlapping, and 1 elsewhere.
- Step 3 : Inpainting of S (in wavelets) using the masks previously defined.
- Step 4 : Estimation of A for fixed S by minimizing $\|X - AS\|_F$.

As can be seen in Figure 4.8, our inpainting step corrects well the leakage from the synchrotron to the thermal emission component in our second toy model : the retrieved spectra are closer to the truth. The resulting impact on the fitting in `Xspec` is also significant, as the temperatures are now more accurately retrieved for sufficiently high Thermal emission/Synchrotron ratios (see Figure 4.8). The convergence of our new loop is not mathematically proven, but we empirically noted that the solution did not evolve significantly after a few iterations of the new step. In the science cases that we have explored, three iterations were sufficient to recover more accurate spectral results.

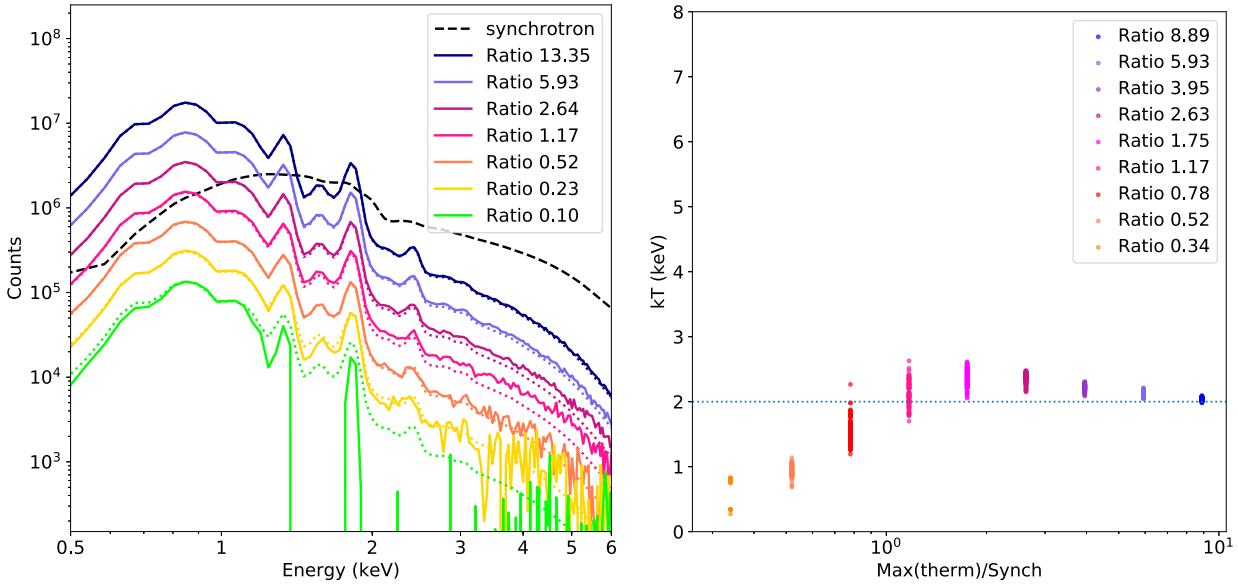

FIGURE 4.8: Same as Figure 4.6 after the inpainting step described in this Section.

The aim of this additional step is to correct the improper treatment of Poisson data in GMCA, that is supposed to work on linearily mixed data sets. It helped us get less polluted spectra while a better solution was not available, but the development of the pGMCA algorithm solved this problem in a more accurate and robust way (see Chapter 5)

Summary :

- Adding an inpainting step in GMCA helps reducing the pollution from the main component to the other one.
- This step is meant to correct the improper treatment of Poisson data in GMCA. That issue will be further addressed in Chapter 5.

4.5 GMCA applied on toy models with more than two components

We designed two more toy models featuring three sources instead of two (see Table 4.1, and Table 4.2 for flux ratios). In our third toy model, we put a synchrotron and two Gaussians centered respectively on 6.54 keV and 6.63 keV. The one at 6.63 keV has a norm equal to 0.7 times that of the other one. Here, the Gaussians are the instrumental responses to a Dirac, hence they have a smaller width than in the first toy model. This is what we would get if the first wide Gaussian truly was the sum of two thinner ones slightly shifted. As we need a more precise definition in energy, the binning is thinner than in our previous toy models (14.6 eV), but the total number of counts are of the same order.

In our fourth toy model, we put a synchrotron and two thermal emissions, one with kT equal to 0.5 keV, the other with kT equal to 2 keV. The norm of the first one is equal to 0.7 times that of the second one. For the images, we used the blue and red shifted Fe components shown in Figure 4.10. As for our first two toy models, we added to our third and fourth toy models a constant image associated with the spectrum of an instrumental noise, and we generated Poisson noise on the whole data cube. The total number of counts of the synchrotron corresponds to a 100 ks observation, and the second main component (the brightest Gaussian or thermal emission)/synchrotron ratios we tested are the same as before.

GMCA is able to disentangle properly the three sources for the highest second main component/-continuum ratios, but when the sources weaken, it only retrieves the synchrotron and a second source

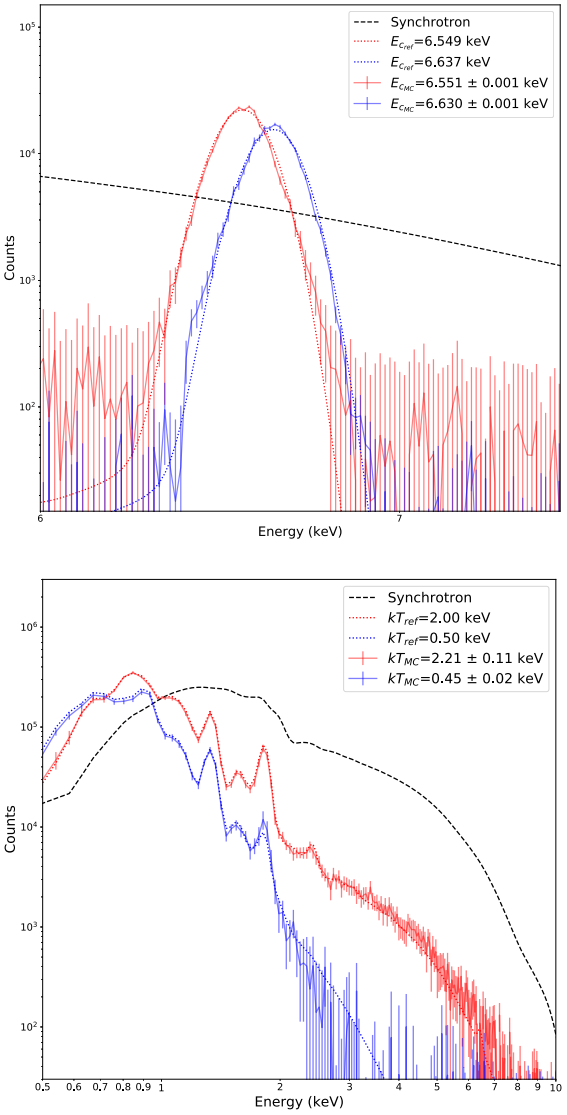

FIGURE 4.9: Spectra retrieved by GMCA in our third and fourth toy models with a total number of counts corresponding to a 100 ks observation. On the left, spectra retrieved by a GMCA with inpainting step of the two gaussians in our toy model 3, with a First line emission/Continuum ratio of 5.93 and a thinner binning (14.6 eV). On the right, the spectra retrieved with inpainting step of the two thermal emissions in our toy model 4, with a First thermal emission/Continuum ratio of 2.64. We added the error bars and the kT and E_c given by a hundred MC realizations.

that is a composite of the two Gaussians, or of the two thermal emissions. Using the inpainting step helps disentangling the three sources a little longer and improves the spectra in the thermal emission case. In Figure 4.9, we can see an example of correct disentanglement of the components in both toy models. The presented line/continuum and thermal/continuum ratios are the last ones to give correct images and correct spectra for every component.

We fitted the retrieved thermal emission spectra of our fourth toy model in `Xspec`, in order to estimate kT. We used as error bars the standard deviations of a hundred MC realization. The first thermal emission's temperature is slightly overestimated with MC error bars, but the overestimation is of the same order as with our second toy model.

Summary :

- The images and spectra retrieved by GMCA are still accurate when there are three components to disentangle, with two presenting high similarities.
- When the two similar components are not disentangled from one another, they are merged into a single component by GMCA.

4.6 GMCA applied to real data

Following the consistency and the robustness tests described above, we present here a first application of GMCA to the deep *Chandra* observations of Cassiopeia A, which was observed with the ACIS-S instrument in 2004 for a total of 980 ks (ObsID : 4634, 4635, 4636, 4637, 4638, 4639, 5196, 5319, 5320). The event lists from all observations were merged in a single data cube. The spatial and spectral binning are adapted so as to obtain a sufficient number of counts in each cube element. No background subtraction or vignetting correction has been applied to the data.

We apply GMCA to the Cassiopeia A observation between 5 and 8 keV, where the prominent features are known to be the synchrotron emission and the Fe K line complex. To allow for unexpected sources to be retrieved by the algorithm, it is recommended to decompose the data into a larger number of components than expected in a first guess. By doing this, we obtain three physically meaningful components in Cassiopeia A : continuum emission, and two Gaussian lines that appear to be slightly shifted with respect to one another, and from the Fe K average energy. The first component is undoubtedly the synchrotron emission, for which the image is coherent with our knowledge of its spatial distribution ; the corresponding spectrum can be described as a power law (Figure 4.10, upper left panel). The two other components have spectra corresponding to blue- or red-shifted Fe line emission (Figure 4.10, right panels), and the associated images show clumps typical of the spatial distribution of Fe in Cassiopeia A (see DeLaney et al., 2010a, Figure 7). If we instead require the algorithm to find only two components, it retrieves the synchrotron emission and a composite of the two Fe components. If we impose on the algorithm to find more than three components, the additional retrieved sources are simply noise. The lower left panel of Figure 4.10 shows an image of what we identify as noise in such a case.

Our method allows direct imaging of the red- and blue-shifted Fe K components with unprecedented spatial resolution. In addition, instead of estimating a mean shift in each line of sight (such as would be obtained

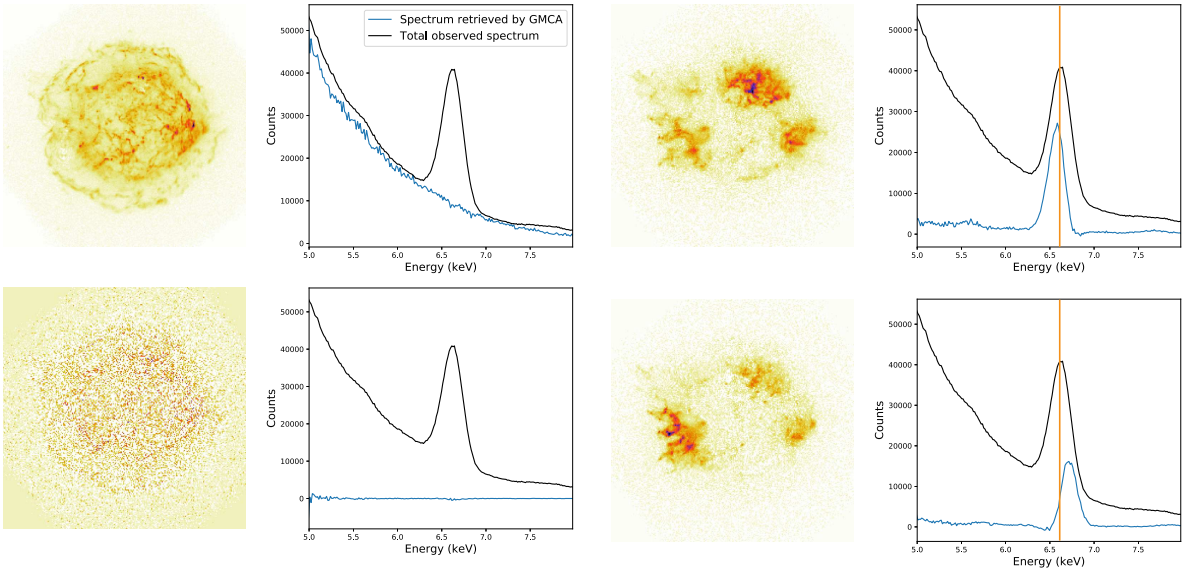

FIGURE 4.10: Images and spectra retrieved by GMCA with inpainting step in the real data from Cassiopeia A between 5 keV and 8 keV. On the upper left, the source corresponds to a synchrotron emission while the two on the right are parts of the Fe K distribution. The top one is a red-shifted part of this distribution, while the bottom one is a blue-shifted part of the distribution. The orange line corresponds to the theoretical Fe K line emission. The last image, on the lower left is the one we identify as noise. The order in which GMCA retrieved these sources is : synchrotron, red-shifted Fe K, blue-shifted Fe K, noise. We inverted the two last ones in order to present both Fe K structures one on top of the other. The color scale is in square root.

when fitting with one Gaussian is performed), our method can disentangle the red and blue-shifted components along a line of sight as shown in Figure 4.10, where both emissions co-exist in the South-East.

Summary :

- The first application of the method around the Fe K Line in the real *Chandra* observations of Cassiopeia A gives images of the red- and blue-shifted Fe K components of an unprecedented spatial resolution.
- It also gives a precise image of the synchrotron emission around 5 and 8 keV

4.7 Elements of response to the first questions raised by GMCA

This chapter was an attempt to assess the reliability of GMCA applied on X-ray data, and the first tests we made on the algorithm give us a better understanding of its behaviour regarding the number n of components to retrieve. We are thus able to give elemets of response to the two first questions raised in Section 3.6.

4.7.1 How can we know that the output results are physically significant, while there is no prior physical information needed ?

By creating toy models inspired by real X-ray observations of SNRs, our intention was to assess the accuracy of GMCA, and the results were probing. In addition to a generally great accuracy of both the retrieved images and spectra with the undelying models, it appeared that in no case GMCA retrieved images of spurious, over-interpreted structures. Furthermore, the outputs of the algorithm is of the same nature as the inputs, for they all take the form of a number of counts per bin. For that reason, a fitting with analysis tools such as `Xspec` seems appropriate to retrieve physical parameters. However, the components retrieved by GMCA are no longer Poissonian : we would therefore need errors to fit them in `Xspec`. In the case of toy model, a simple Monte-Carlo would do, but with real data the problem is not trivial, thus leaving us with the third question unanswered : how could we obtain errors or confidence ranges ? On this particular topic, see Chapter 6.

4.7.2 How can we choose the number of components to retrieve in the most accurate way ?

From a statistical viewpoint, evaluating the number of components to be retrieved boils down to a model selection problem. A criterion such as the Akaike Information Criterion (AIC) may be used to solve it. Testing for an increased number of components n is equivalent to testing a model with $n_x{*}n_y{+}n_E$ additional degrees of freedom and selecting the one with the lowest AIC.

For a given model, the AIC is defined as twice the difference between the log-likelihood and a complexity term p :

$$AIC = -2\log(L) + 2p \tag{4.1}$$

Where $p = (n_x{*}n_y{+}n_E){*}n$ is the number of degrees of freedom, and L, the log-likelihood for n components, is defined as :

$$L = AS - AS\log(X) \tag{4.2}$$

A and S being the solutions obtained by GMCA for n components. For example, in the test presented in Figure 4.11 we applied GMCA to Cassiopeia A real data between 5 and 8 keV with a number of components increasing from 1 to 7 and looked at the AIC of the different models. The images shown seem to indicate that after 3 components, no other meaningful components are retrieved, which is confirmed by the AIC.

Even if the test was satisfying in the example presented above, we cannot ensure that it will be thus with any other data set for the reason we mentioned. In practice, the main components are stable and well retrieved for different values of n, but there can be fluctuations in the remaining noisy images that would impact the statistical tests even if no actual physics could be made out of their interpretation. Also, adding a physically meaningful component presenting a coherent structure, but too faint to have a clear statistical impact, may not minimize the AIC. Hence, the AIC can be a useful figure of merit to confirm the relevance of a certain chosen n, but should not replace a human interpretation nor be directly implemented inside of the algorithm as an automatized selector for the number of components. However, it could be interesting to expllore further the possibilities offered by this criterion, or others of the same kind.

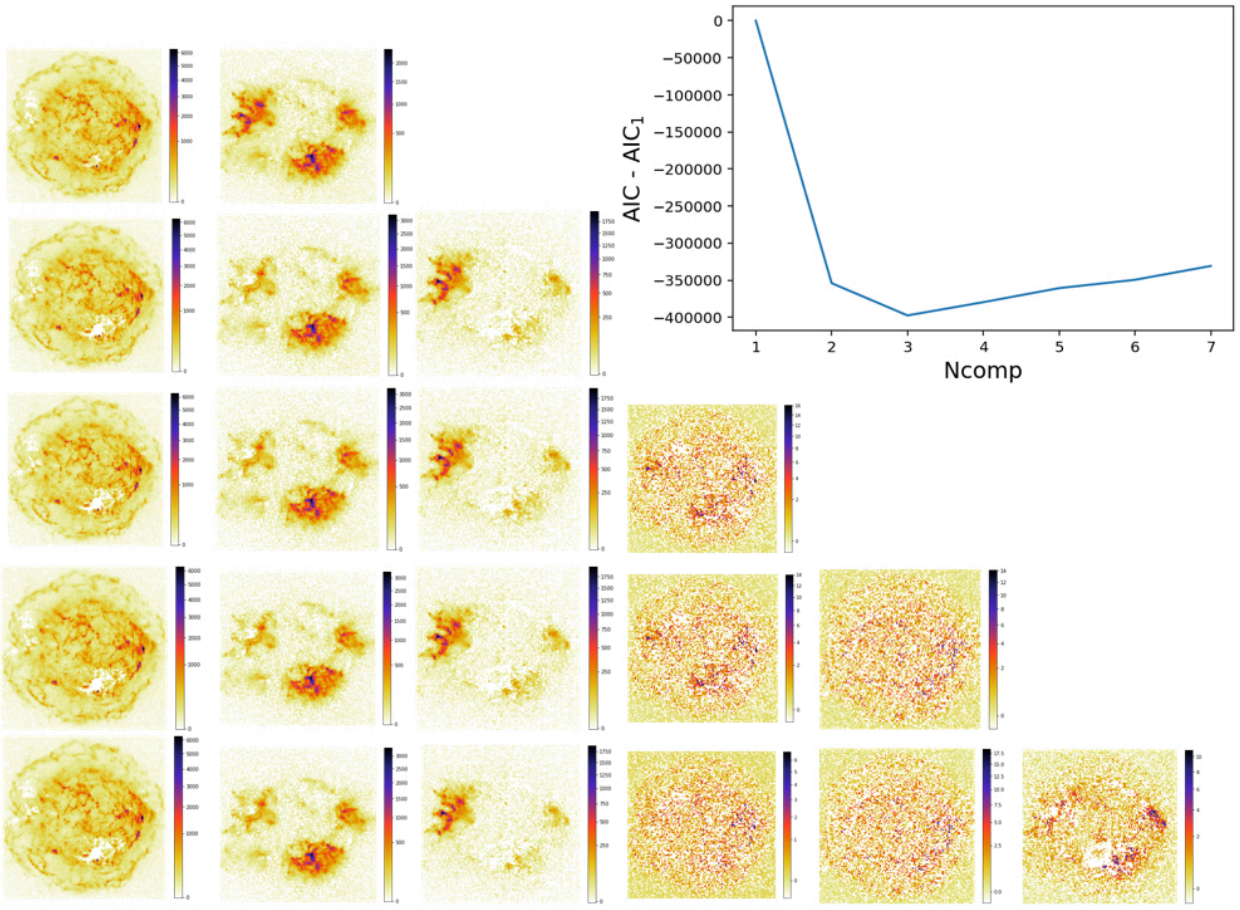

FIGURE 4.11: Components retrieved by GMCA applied on Cassiopeia A real data for different values of n. On each lines, the retrieved components corresponding to a certain n, beginning with $n = 2$ on top. On the right, the AIC of the model as a function of this number of components n. The color scale is in square root.

Summary :

- Our tests on toy models show GMCA retrieves accurate images and spectra, and no spurious, over-interpreted structures. The results of the algorithm can be trusted to infer physical results given the fact, obviously, that they will be checked and interpreted by a human.
- The Akaike Information Criterion (AIC) can be used as a figure of merit to confirm the relevance of a chosen n. However, this criterion must be used with caution, and cannot completely replace a human interpretation yet.

CHAPTER 5

PGMCA

While we were working on testing and applying the GMCA algorithm on X-ray data for the first time, its developing team, of which I am not part, but with whom I work, was elaborating a new version specifically designed to handle Poissonian data (see Bobin et al., 2020). This new algorithm, pGMCA, is also a BSS algorithm working in a similar way as the GMCA, but best suited for X-ray data. However, it is less robust and far more sensitive to the first guess. For that reason, the outputs of a simple GMCA are used as a starting point for the pGMCA, whose better handling of Poissonian data sets brings refinement to the results. Thus, the enhancement this algorithm brings to our method is a continuation of our previous work, where the improper treatment of Poissonian statistics could cause leakage from a source to another. In this Chapter we will present this new algorithm and the associated mathematical formalism.

5.1 Introduction

pGMCA is an upgraded version of GMCA handling Poisson statistics, while GMCA supposed the sources to disentangle to be linearly mixed. As for GMCA, the input of pGMCA is a data cube (E, x, y). Both algorithms are highly similar : they are BSS algorithms needing no prior physical information, the components to retrieve are supposed to be entirely defined by an image and its associated spectrum and the decomposition works iteratively by taking into account the morphological particularities of each component to disentangle. However, the only other input GMCA needs is the number n of components to retrieve, while pGMCA also needs to be given a first guess to start its iterative reconstruction of the images S and spectra A. This new algorithm is indeed less robust, and far more sensitive to the initial condition starting the iterative loop. Thus, we use the results of a simple GMCA as an input for pGMCA to initialize the reconstruction, making this new algorithm a refinement step in our method ensuring a better handling of Poisson statistics.

Summary :

- pGMCA is an upgraded version of GMCA handling Poisson statistics.
- It is highly similar to GMCA, but it is less robust. For that reason, we use the results of a simple GMCA as an input for pGMCA.

5.2 Mathematical formalism

The improper treatment of Poissonian data by GMCA was due to its supposition that the sources to disentangle are linearly mixed :

$$X = AS + N = \sum_{i=1}^{n} A_i S_i + N \tag{5.1}$$

where n is the predefined number of components, X is the observed data cube in wavelets, the A_i are vectors of size E, in our case related to the spectral information (the spectra of our mixed components), the S_i are the sources represented in wavelets, of dimension (x, y, J) and related to the spatial information (the images in wavelets of our mixed components), and N some Gaussian noise. As the Poisson law applies on the images in the direct domain, we will note S_{direct} the array containing the n images of size (x, y).

The pGMCA algorithm replaces this equation by considering the probability for an element $AS_{direct}[elem]$ of the array AS_{direct} to take the value $X[elem]$, rather than an equality. This probability follows the Poisson law :

$$\mathcal{P}(X[elem]|AS_{direct}[elem]) = \frac{e^{-AS_{direct}[elem]} AS_{direct}[elem]^{X[elem]}}{X[elem]!} \tag{5.2}$$

The $\underset{A,S}{min}\|X - AS\|_F^2$ term ensuring the adequation between AS and X in Equation 3.2 thus becomes a minimum on the Poisson anti-log likelihood $\underset{A>0, S_{direct}>0}{min} \mathcal{L}(X, AS_{direct})$. The equation solved by pGMCA is then :

$$\underset{A>0, S_{direct}>0}{min} \sum_{i=1}^{n} \lambda_i \|S_i\|_p + \mathcal{L}(X, AS_{direct}) \tag{5.3}$$

where the $\lambda_i \|S_i\|_p$ still represents a constraint on the wavelet transforms of the images represented by S_{direct} (see Section 3.4). The algorithm solves this equation in an iterative way, using the results of a GMCA as a first guess and alternatively updating A and S_{direct}.

pGMCA being the first sparse BSS method to specifically designed to handle data following a Poisson distribution, its development raised new challenges. As in the original GMCA algorithm, the regularization term makes the problem not convex. But in addition, the Poissonian nature of the data forces us to enforce the positivity of the solutions, and the Poisson anti-log likelihood not being differentiable about 0, prevents us from using a proximal gradient method for the minimization process. For that reason, a Nesterov smoothing technique (Nesterov, 2003) was used to compute a smooth approximation of $\mathcal{L}(X, AS_{direct})$ (for more details, see Bobin et al., 2020).

Summary :

- The main theoretical differences between the GMCA and pGMCA algorithms are that the equality is now a probability following a Poisson law, the term ensuring the similarity is no longer a Frobenius norm but a Poisson anti-likelihood, and there is a positivity constraint. These differences raised new challenges during the development.
- Both algorithms work iteratively.

CHAPTER 6

ESTIMATING ERRORS FROM OBSERVATIONS

The results of the GMCA and pGMCA algorithms when applied to Poissonian data sets do not preserve the Poissonian nature of the data in each retrieved component. Yet, we need error bars to infer physical parameters from fitting in softwares such as *Xspec*. The natural error bars associated to Poissonian data sets being unusable in our case, we have to find another way to estimate errors with only one realization : the observed data set.

Here is a short lexicon to simplify the understanding of this chapter :

Lexicon :

- True Model : In nature, the " reality " of a phenomenon that we imperfectly capture through observation. In simulations, the model before adding any kind of noise.
- Realization : The true model on which some non deterministic uncertainties have been added. For example, additive Gaussian noise or, in our case, Poisson noise.
- Monte-Carlo : Simulating several realizations out of a single model. In our case, each realization is a Poisson realization of our toy models.
- Observed data/Original data : A realization of the implicit natural true model. We will not debate about the existence of this true model independently from any observation, but the important point remains : we only have access to observed data. In this part we will often call this observed data " original " as it is the only data we possess before applying resampling methods.
- Resampled data set : New data sets obtained from a single original data set through a number of possible operations.
- Bootstrap/Block Bootstrap : Resampling methods, better described in Section 6.1.2.
- Kernel Density Estimator (KDE) :A non-parametric way to estimate the probability density function of a random variable. We will use it in Section 6.3 to estimate the underlying probability density of an histogram.

6.1 Introduction

The past few years have seen the introduction in astrophysics of a large number of advanced data analysis methods providing new and interesting results. Classification, PSF deconvolution, denoising, dimensionality reduction or blind source separation methods such as GMCA and pGMCA are among the most exciting and promising new tools the recent development of machine learning and other advanced statistical methods have brought to process, analyze and retrieve physical information from astrophysical signals. We can

formalize the application of these methods by writing $\Theta = O(X)$, where X is the original data and O is the non-linear analysis operator used to process the signal. Most of these methods being non-linear, there is no easy way to retrieve error bars or a confidence interval associated with the estimator Θ. Estimating errors accurately in a non-linear problem is still an open question that goes far beyond the scope of astrophysical applications, as there is no general method to get error bars from a non-linear data-driven method such as a machine learning process. This is a hot topic whose study would be essential for an appropriate use of complex data analysis methods in retrieving physical parameters, and for allowing the user to estimate the accuracy of the results.

The pGMCA algorithm being non-linear and highly sensitive to the initial conditions, it constitutes a perfect example of that kind of advanced data analysis methods for which there is still no proper way to obtain error bars. In this chapter, we will present our work on developing such a method to retrieve error bars associated to non-linear estimators on Poissonian data sets. We will mainly focus on the specific case of pGMCA applied on X-ray data sets, but our method is far more general and could be used to retrieve errors for any kind of non-linear estimators on Poissonian data sets. This method is based on the principle of the bootstrap (see Efron, 1979), but corrects the biases the bootstrap introduces when applied on Poissonian data sets (see Section 6.2), and would then be suitable for estimating the errors of non-linear estimators involving advanced statistics or machine learning tools, bringing an element of solution to the open question of the confidence intervals associated to that kind of operators (see Section 6.3). However, we will see in Section 6.5 that if it accurately corrects biases, it fails to reproduce an appropriate spread, so that the error bars retrieved do not have a physical significance. Nevertheless, this method constitutes an interesting and brand new way to assess the robustness of a non-linear algorithm around the initial conditions given by the original data, and a promising attempt at retrieving physically significant error bars.

6.1.1 Existing method to retrieve error bars on Poissonian data sets

Our aim, when searching for error bars associated to a certain estimator Θ, is to obtain the variance of $\Theta = O(X)$, where the original data X is composed of N elements. When working on a simulation, an obvious way to proceed in order to estimate the variance of Θ is to apply the considered data analysis method O on a certain number of Monte-Carlo realizations X_i and look at the standard deviation of the results $\Theta_i = O(X_i)$. The variance of the Θ_i provides a good estimation of the errors. Yet, this cannot be done with real data, as only one observation is available : the observed one. Thus, a resampling method such as the jackknife, the bootstrap or its derivatives, able to simulate several realizations out of a single one, is necessary. Ideally, the aim is to obtain through this resampling method a number of " fake " Monte-Carlo realizations centered on the original data : new data sets variating spatially and reproducing the spread of Monte-Carlo drawings with a mean equal or close to the mean of the original data.

The mechanisms at stake in jacknife or bootstrap resamplings are similar. Jacknife and bootstrap resampling methods produce n resampled sets $\tilde{X}_i$ by rearranging the N elements of X, and allow us to consider the variance of $\Theta_i = O(\tilde{X}_i)$ for i in $[\![1, n]\!]$ as an approximation for the variance of Θ. The bootstrap creates a resampling by randomly selecting N elements with replacement in X, while the jacknife method defines n boxes containing $\frac{N}{n}$ elements and creates n resamplings of size $(n-1)\frac{N}{n}$ by concatenating $n-1$ boxes.

As jacknife and bootstrap methods are close to each other, and the bootstrap and some of its derivatives are more adapted to handle correlated data sets, we will in this chapter focus on a particular method, representative of other resampling methods and theoretically suited for astrophysical applications : the block bootstrap, which is a simple bootstrap applied on randomly formed groups of events rather than on the individual events.

In the case of a Poisson process, the discrete nature of the elements composing the data set can easily be resampled with a block bootstrap method. The N discrete elements composing a Poissonian data set X will be called " events ". In high energy astrophysics for example, the events are the photons detected by the spectro-imaging instrument. The block bootstrap method can be applied on such a data set by defining blocks containing a certain number of events. The data can be of any dimension but for clarity, we will mainly show bi-dimensional data sets, i.e. images.

6.1.2 Bootstrap and block bootstrap presentations

The bootstrap is a statistical method consisting in a random sampling with replacement from a current set of data. If the initial data X is a collection of N elements, a resampling obtained through bootstrapping would be a set $\tilde{X}^{boot}$ of N events taken randomly with replacement amid the initial ones (see Figure 6.1). This method can be repeated in order to simulate as many realizations $\tilde{X}_i^{boot}$ as needed to estimate standard errors or confidence intervals. In order to save calculation time, we can choose to resample blocks of data of a fixed size instead of single events : this method is named block bootstrap. The block bootstrap is also supposed to conserve correlations more accurately, making it more appropriate for a use on astrophysical signals. In our case, the data is the set of all photons detected by an X-ray telescope during an observation, each photon being considered as a triplet (E, x, y). For Cassiopeia A as seen by *Chandra*, it represents a few hundred millions of events. The ordering variable is time, independent of (E, x, y), so defining blocks preserves the random character. There is no proper way to choose a block length a priori ; a few tests seem to indicate that a length of the order of the cube root of the total data set size is efficient with the data we used : reducing the length increases the calculation time without significantly modifying the results.

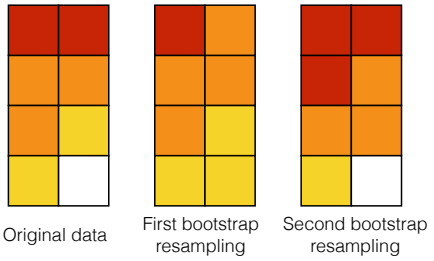

FIGURE 6.1: An example of bootstrap resamplings. Each square represents a different event, each color a different value. N events are taken randomly with replacement from the original data to create each of the two bootstrap resamplings.

The block bootstrap method produces a certain number of resampled data sets that are to be used as a way to estimate the accuracy of a given estimator by comparing its results on each data set. For the rest of our analysis, we will use a hundred resampled data sets because we established in preliminary tests there were no substantial differences between the errors obtained by looking at the standard deviations of a hundred or a thousand resamplings with our data.

6.2 Biases

The properties of the resampled data strongly depends on the nature of the original data. Biases may appear in the resampled data sets, proving a block bootstrap can fail to reproduce consistent data that could be successfully used to evaluate the accuracy of certain estimators.

6.2.1 Resampling a Poissonian data set

Poissonian data sets, of which we can find several examples among astrophysical signals, are not consistently resampled by current resampling methods such as the block bootstrap. A Poissonian data set X can be

defined as a Poisson realization of an underlying theoretical model X^*, which can be written :

$$X = \mathcal{P}(X^*)$$

where $\mathcal{P}(.)$ is an operator giving as an output a Poisson realization of a set.

A look on the histogram of a data set resampled from a Poissonian signal shows the block bootstrap fails to reproduce accurately the characteristics of the original data. Figure 6.2, top, compares the histogram of the real data X, a simple image of a square with Poisson noise, with the histograms of the resampled data sets $\tilde{X}_i^{boot}$, and highlights the fact that the latter are more similar to the histogram of a Poisson realization of the original data $\mathcal{P}(X) = \mathcal{P}(\mathcal{P}(X^*))$ than to the actual histogram of the original data $X = \mathcal{P}(X^*)$, where X^* is the underlying model of a square before adding Poisson noise. This is consistent with the fact that the block bootstrap is a random sampling with replacement, which introduces uncertainties of the same nature as a Poisson drawing.

6.2.2 Example definition

As we will focus in this study on astrophysical cases linked to our use of pGMCA, we will use as a test a simulated image of Cassiopeia A. Besides being the SNR on which we worked the most with both the GMCA and pGMCA algorithms, this source provides a variety of morphologies and dynamic range perfectly fitted to test our method. As we will need a way to assess the similarity between our new method and Monte-Carlo drawings, it is important that we know the underlying model of our Poissonian data sets. For that reason, we define our image by integrating the original *Chandra* data along the energy line, and we blur the image thus obtained to diminish the noise. We then divide it by a certain number in order to lower the statistics and consider the resulting image our underlying model. The tests are then made on Poisson realizations of this image. Even if constructed on real data, the process we applied allow us to know the underlying model of the Poisson realization we consider. For that reason, we will refer to this image as " simulated Cassiopeia A ".

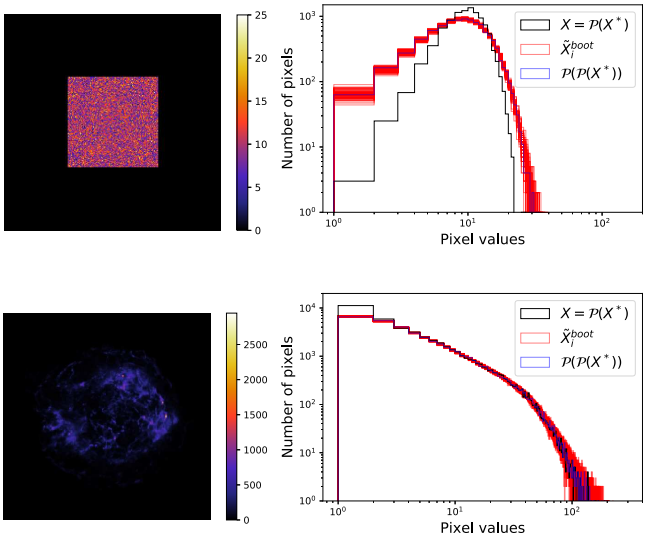

FIGURE 6.2: Data sets and their associated histogram in two cases : on top, the very simple case of a Poisson realization of the image of a square with uniform value 10 ; on the bottom, the simulated Cassiopeia A image. On the right, the black histogram correspond to the original data $X = \mathcal{P}(X^*)$. The red histograms are those of the data sets $\tilde{X}_i^{boot}$ obtained through resampling of the original data and the blue ones are the histograms of a Poisson realization of the original data $\mathcal{P}(X) = \mathcal{P}(\mathcal{P}(X^*))$. It appears that the resampled data sets have histograms highly similar to that of the original data with additional Poisson noise.

Figure 6.2, bottom, shows the comparison between the histogram of the simulated Cassiopeia A image and the histograms of the data sets resampled with a block bootstrap. We can see the resampling is, in this case too, adding Poissonian noise and gives histograms resembling $\mathcal{P}(\mathcal{P}(X^*))$ rather than $\mathcal{P}(X^*)$.

6.2.3 Morphologies of the resampled data sets

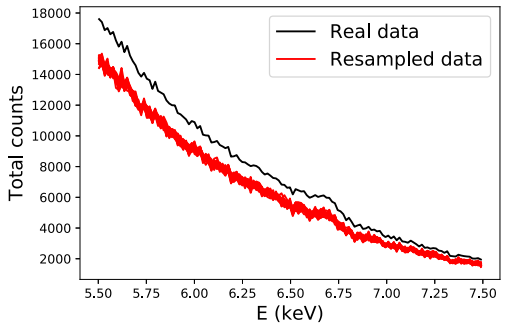

FIGURE 6.3: Spectrum of the synchrotron component retrieved by pGMCA on the 5.5-7.5 keV energy band on real data and on a set of 30 block bootstrap resamples. There is an obvious bias in the results, the resampled data spectra being consistently underestimated.

In order to get more information about the morphologies of the images and their resampled counterparts we consider their wavelet coefficients scale by scale. Wavelet coefficients contain information about the spatial features of an image at different scales, allowing us to evaluate what an improper processing of the Poisson noise means in terms of morphology for an image. Figure 6.4 shows the implications on the wavelet coefficients of the images, that are directly linked with the spatial structures of the data sets. Small scales, where Poisson noise dominates, are particularly impacted by the biased nature of the resampling on the example of the square. The resampled data sets are too different morphologically from the original data set to be used as a way to estimate error bars. On the Cassiopeia A example, there is no visible bias for most wavelet scales, but we can notice one on the first wavelet scale, that is the most sensitive to Poisson fluctuations.

The same goes with data cubes of the (E, x, y) form. The pGMCA algorithm being non-linear and its results being strongly dependent on the input data, a systematic change in the nature of the input will result in a bias between the components retrieved on the original data and those retrieved on the resampled data sets. This effect clearly appears in Figure 6.3, where in some cases the results of a pGMCA applied on the real data of Cassiopeia A between 5 and 7 keV are not comprised in the set of results obtained by applying pGMCA on the resampled data sets. This is problematic, as the aim of a block bootstrap resampling would be to provide an estimation of the variation of the pGMCA results on resampled data variating around the real data.

It results from this study that the block bootstrap method fails to reproduce the outputs of a " fake " Monte-Carlo centered on the original data, and it cannot be used in its original form to estimate the accuracy of non-linear data analysis methods such as the pGMCA algorithm. However, the idea of estimating the accuracy of pGMCA through the application of the algorithm on resampled data sets is promising, and lead us to develop a new bootstrap-like method that would constrain the nature of the resampled data sets in order to avoid biases.

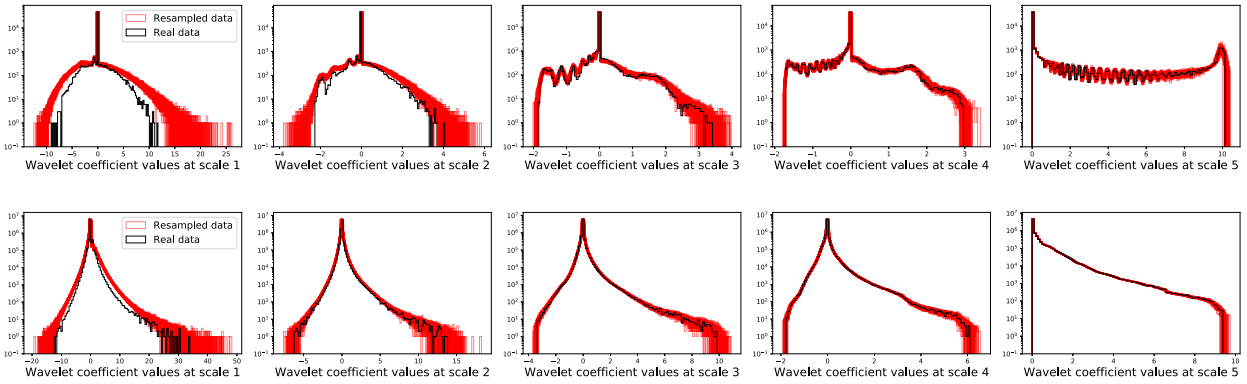

FIGURE 6.4: Histograms of the wavelet coefficient values for a five scales starlet transform. On top, the original data is the image of a square presented in Figure 6.2, top. On the bottom, the original data is the simulated Cassiopeia A image.

Summary :

- In order to retrieve error bars out of a single observed realization, we can use a resampling method that will produce resampled data sets on which we can apply our algorithm.
- The block bootstrap method is inappropriate as it introduces an additional Poisson noise, thus modifying the histogram of the data. The application of pGMCA on the resampled data sets then results in producing biases.
- The histogram is a good marker to know if an additional Poisson noise has been introduced : we have to develop a new constrained resampling method that would ensure the histogram of the resampled data sets to be similar to the original one.

6.3 A new constrained bootstrap method

As we were not able to find any solution to the bias issue in the litterature, we developed a bootstrap-like method preserving the nature of Poissonian data sets thanks to the addition of a constraint in the resampling process.

6.3.1 General principle

Bootstrap resamplings consisting in random drawings with replacement, it is natural that they fail to reproduce some characteristics of the data, among which the histogram that gets closer to the histogram of a Poisson realization of the original data than to the histogram of the actual data. The block bootstrap method is therefore unable to simulate a Monte-Carlo centered on the original data : the alteration of the histogram strongly impacts the nature of the data, hence the differences in the morphologies observed by looking at the wavelet coefficients or the differences in the results obtained by pGMCA. It is then necessary to find a new method in which we could force the histogram of the resampled data sets to be similar to that of the original data.

A natural way to do so would be to impose the histogram we want the resampled data to have before actually resampling the data. To allow this constraint to be made on the pixel distribution, we can no longer consider our events to be the individual elements of X or a block assembling a random sample of them. We should directly work on the pixels and their values, the pixels here being the basic bricks constituting our data. Just as the block bootstrap, our new method can work with data of any dimension. In the case of images, the " basic bricks " correspond to actual pixels. In the case of X-ray data cubes, they are tiny cubes of the size of a pixel along the spatial dimensions, and the size of an energy bin along the spectral dimension. The same goes for any dimension of our original data. The method can also be adapted for uni-dimensional data sets. **The key of our new method is then to work on the histogram of the data presenting the pixels' values rather than on the data itself, event by event.** Thanks to the Poissonian nature of the data set, pixels have discreet values, allowing us to work on a finite number of possible values.

We can either change the value of a pixel or exchange the value of a pixel for that of another one. The first operation simultaneously adds and subtracts 1 in the corresponding columns of the global histogram while the second operation does not produce any change in it. A good mixture of these two operations

would then allow us to obtain the histogram we want to impose in our resampled data sets, and following a Poisson probability law to select the pixels to exchange would introduce some spatial variations, in order to reproduce what a Monte-Carlo would do.

Our new constrained bootstrap method is thus composed of two steps, that are described below and illustrated in Figure 6.5 :

- Obtaining the probability density function of the random variable underlying the observed data histogram using the KDE, and randomly generating N histograms from this density function with a spread around the data mimicking that of a Monte-Carlo.
- Producing resampled data sets associated with the new histograms by changing the values of wisely chosen pixels in the original image.

During these steps, the pixels equal to zero remain equal to zero, and the non-zero pixels keep a strictly positive value. This constraint enforces the number of non-zero pixels to be constant and avoids the random emergence of non-zero pixels in the empty area of the original data. While this is not completely realistic we prefer constraining the resampled data sets in this way than getting spurious features. We could explore ways to release this constraint in the future.

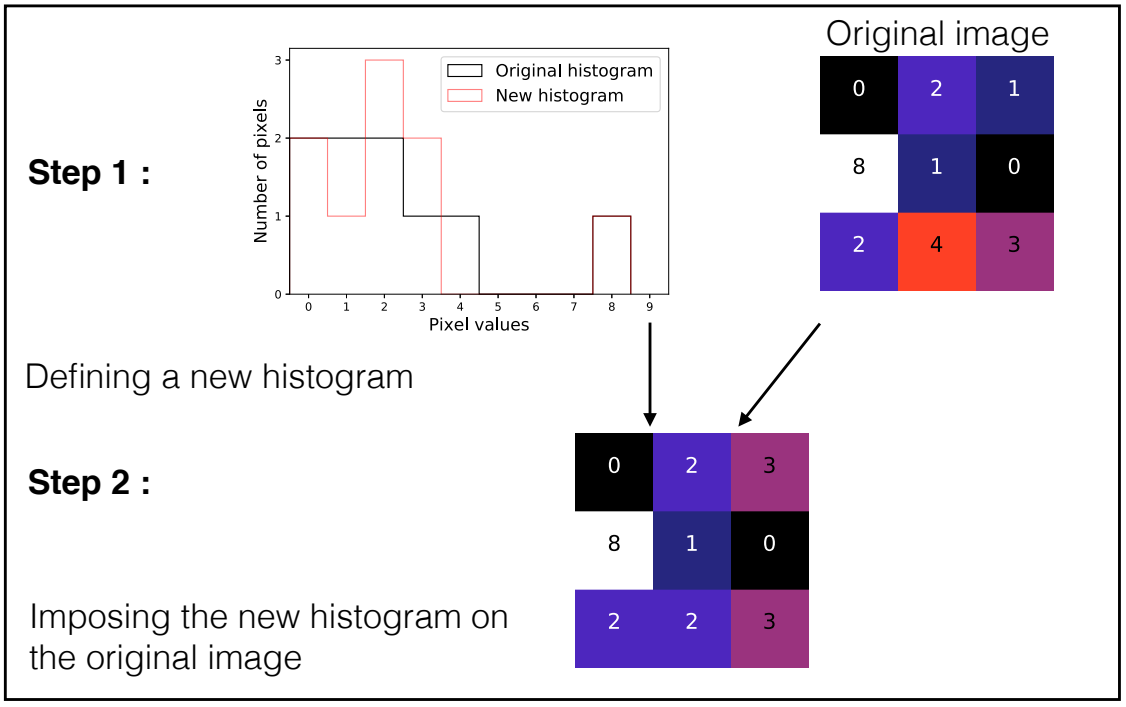

FIGURE 6.5: Scheme resuming the two steps of our new constrained bootstrap method.

6.3.2 First step : generating new histograms

The aim of this step is to generate different histograms reproducing a Monte-Carlo drawing centered on the original data. A way to do so is to estimate the probability density function underlying the original data. A Kernel Density Estimator (KDE) can do it by smoothing the original data with a chosen kernel, a non-negative function with a compact support. The KDE estimates the underlying density probability from the histogram of the original data without the zero pixels that we do not intend to modify, and we draw randomly as many values as we need following this law to get a new histogram : the number of non-zero pixels in the original data. Figure 6.6 shows the histogram of the image of a square presented in Figure 6.2 as well as its KDE and the samples drawing of a new histogram thanks to this KDE. In practice we use the KDE implementation in the Python library *scikit-learn*[1] with a linear kernel function.

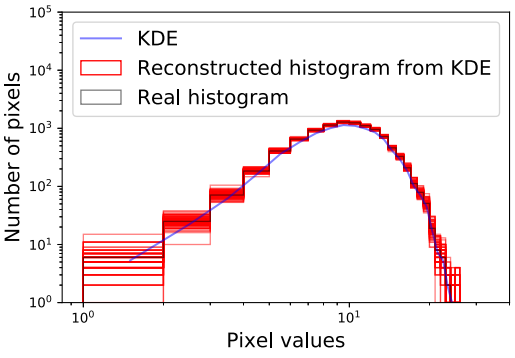

FIGURE 6.6: A hundred histograms reconstructed out of a drawing following the KDE probability distribution, compared to the real one.

One of the advantages of working on the histogram is that it is easier to obtain an accurate estimation of the underlying density function in one dimension, but the method we use to do so is not important. The KDE was chosen for its good results and its robustness but we also added an iterative corrective step to compensate fort the occasional errors in the density function estimation. If the new histogram drawn from the probability distribution deriving from the KDE is too different from the original one, typically by more than 10%, we can improve their similarity thanks to this corrective step in which the mean of a good number of histograms drawn from the KDE is compared to the original histogram. For each value, the KDE is adjusted so that a new drawing would get closer to the original histogram. This step stops when the mean of the good number of new histograms is close enough to the original. Usually, we enforce the relative difference for each value of the histogram to be inferior to five percents, and we choose this " good number " around 5000 to ensure the average of the histograms to be close to the expected value thanks to the law of large numbers.

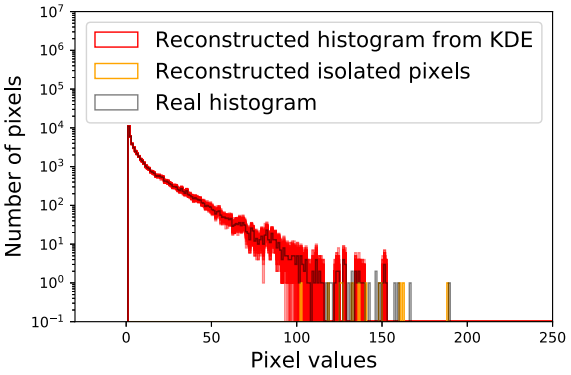

FIGURE 6.7: The image of Cassiopeia A shows a more complex histogram than that of the square containing isolated pixels. The red part of the reconstructed histogram was generated by a drawing from the KDE, and the orange part corresponding to the isolated pixels was treated independently by drawing new values from the values of the isolated pixels present in the original histogram.

Some histograms present isolated values that should not be treated in the same way. A value taken by only one pixel and that is not close to any other value in the histogram should be considered as isolated, and the KDE is not suited for isolated values. As a matter of fact, drawing from the KDE does not insure the same number of pixels to take a certain value to be the same as before, which in the case of isolated values could introduce huge biases. For example, an image in which every pixels but one have values between 0 and 10 and the last pixel takes the value 100 should give new data sets in which only one pixel takes an extreme value. Thus, we define a list of isolated values in the histogram that are not to be redefined through the KDE method and we change these values by drawing a

[1] https://scikit-learn.org/stable/modules/density.html

Poisson realization of them. This way, the number of isolated values stays constant and their spread from a new data set to the other follows a distribution close to that of a Monte-Carlo centered on the original data, as can be seen in Figure 6.7.

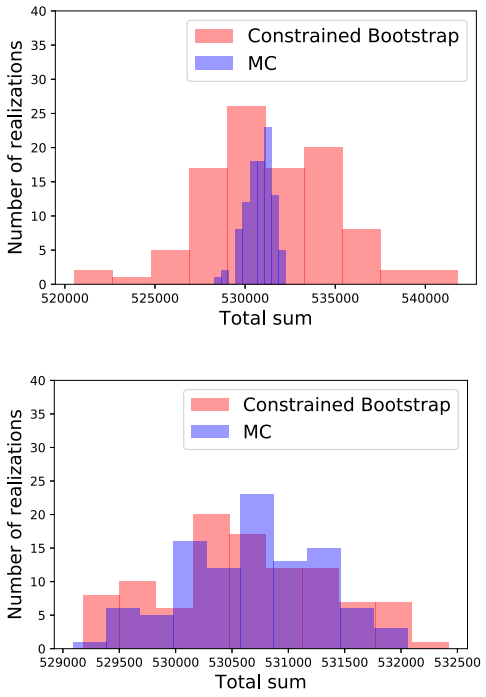

FIGURE 6.8: Comparison between the total sums of the constrained bootstrap resamplings and Monte-Carlo realizations. On top, without selection. On the bottom, with a selection.

A way to ascertain the similarity between the spread between the histograms produced thanks to the KDE and the isolated pixels step and those obtained by a Monte-Carlo would be to compare the spreads between the total of counts in both cases. Figure 6.8, top, shows that the total of counts of the hundred histograms produced thanks to the KDE have a significatively larger spread than those of the hundred histograms obtained through Monte-Carlo. For that reason, we chose to add a selection criterion enforcing the total of counts to have a similar spread to that obtained with a Monte-Carlo. As we noticed the spread of the total of counts of the hundred MC histograms was similar to that of a hundred Poisson realizations of the total of count of the original data, we draw a hundred Poisson realizations of this original total of counts and separate the numbers thus obtained into ten " boxes " of the same size, but containing more or less realizations depending on their closeness to the original value. Then, when generating new histograms from the KDE and isolated pixels step, we look at its total number of count. If this number is included between the bounds of one of the boxes, and if there has not already been as many accepted histograms associated to this box as there were numbers from the Poisson drawings in it, the histogram is accepted. Otherwise, another one is randomly drawn from the KDE and the isolated pixel step. We repeat this operation as much as needed, until we obtain a hundred new histograms whose total counts follow a distribution similar to that of a Monte-Carlo, as we can see in Figure 6.8, bottom.

6.3.3 Second step : enforcing a new histogram on the data

The new histograms we obtained in the first step of our new method contain as many non-zero pixels as before, so in the difference between a new histogram and the original one, there are as much positive and negative values, as we can see in Figure 6.9, on top. Positives correspond to values that are taken by more pixels than before ; negative to values that are taken by less. Hence, we name " positive list " the values that have to be added to the histogram and " positive list " the ones that have to be subtracted, and both lists have the same size. In the example presented in Figure 6.9, the positive list is $[2, 3]$ and the negative list is $[1, 4]$, with only one occurence of each value in both lists. We will simply take values from the positive list and impose them on pixels associated to values in the negative list. By changing the values of these pixels in this way, we ensure the new data set to have the exact same histogram we created in the first step.

However, this process can neither be deterministic nor uniformly random. We must ensure the new and the old values are close enough to be both drawn from Poisson realizations of a same underlying model. Thus, we randomly browse the positive list, and for every value in it we select the value in the negative list that it will replace. Every value in the negative list has a probability to be chosen deriving from the probability

for a Poisson realization of the value from the positive list to equal it. In our example, we will randomly browse the $[2, 3]$ positive list and draw Poisson realizations of its elements. If we begin by the element 3, its probabilities to take the values 1 or 4 are proportional to the probabilities to obtain these values through a Poisson drawing of 3. If we obtain 4, the only remaining value in the negative list would be 1, while the only remaining value in the positive list would be 2. Hence, the 2 and 3 elements in the positive list are respectively associated to 1 and 4.

We then exchange the values of pixels associated to the chosen one in the negative list for the value in the positive list and subtract the number of exchanged pixels from the number of pixels that still have to be exchanged. We do the same process as long as needed to obtain a new data set associated with the desired histogram. In our example, this process would result in a new image in which the pixel equal to 4 would be replaced by a 3 and one of the 1 pixels would be replaced by a 2. For example, New Image 1 and 2 in Figure 6.9.

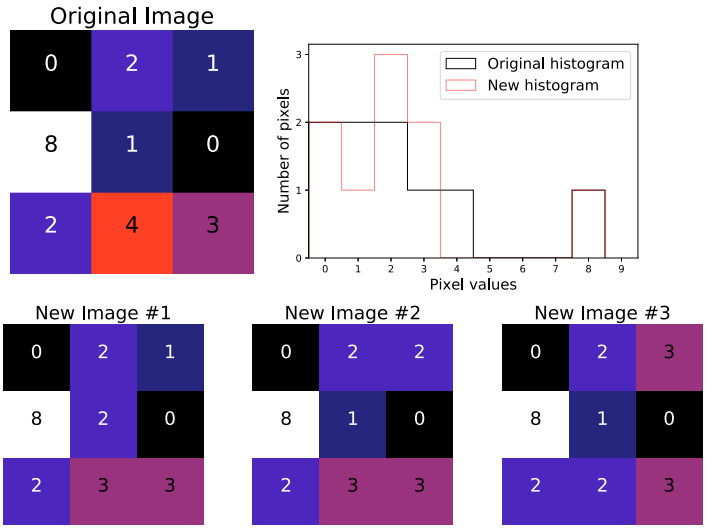

FIGURE 6.9: Illustration of the second step of our method with a simple 3x3 image. On top, the original image and its associated histogram, and the histogram we want to impose. On the bottom, three realizations of our second step resulting in new images associated to the imposed histogram. We can see that the values disappearing from the original histogram (1 and 4) are replaced by the new values (2 and 3) in a non deterministic way. Note that there are as many zeros in both histograms, which is required by our method.

Summary :

- Our new method is working on the histogram of the data rather than on the individual events in order to constraint the histograms' shapes.
- In a first step, we retrieve the probability density function of the random variable underlying the observed data histogram using the KDE, and we randomly generate N histograms from this density function with a spread around the data mimicking that of a Monte-Carlo.
- In a second step, we produce resampled data sets associated with the new histograms by imposing them on the original data in a non deterministic way : the values absent from the new histogram are replaced by those introduced by the new histogram following the probability for a Poisson drawing of the old value to be one of the new available values.

6.4 Testing our new bootstrap method

Our new constrained bootstrap resampling method needs to be tested on two main criteria : does it preserve the nature of the data, and does the spread of the distribution of the data sets successfully mimick that of a Monte-Carlo centered on the real data ?

6.4.1 Nature of the resampled data sets

The first important criterion in testing our new method is to make sure it preserves the nature of our data : its Poissonian nature, and its spatial features. As in Figures 6.2 and 6.4 we compare the histograms of the resampled data sets to that of the original data of the square and the simulated Cassiopeia A images, to make sure no additional Poisson noise has been introduced. We do the same with the histograms of wavelet coefficients at different scales, giving information about the spatial features of our data sets.

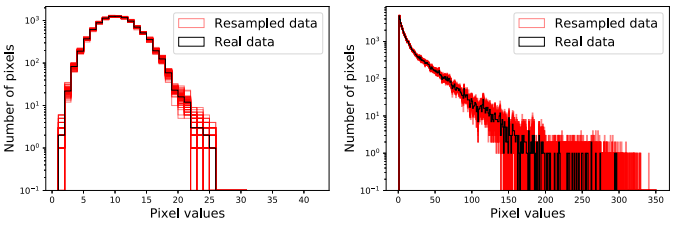

FIGURE 6.10: Histograms of the resampled data sets obtained by our new constrained bootstrap method compared with the histogram of the original data, the image of a square defined in Figure 6.2 on the left, and the simulated Cassiopeia A image on the right.

The results are shown in Figure 6.10, that highlights the similarities between the original and the simulated histograms, and Figure 6.11. In the latter, we can see a good adequacy between the original and the resampled data sets for every wavelet scales, apart from the first scale that still appears to be slightly biased, even though it is reduced. Thus, it appears that our new method preserves better the nature of the data than a block bootstrap. We can now test wether our method satisfyingly mimicks a Monte-Carlo.

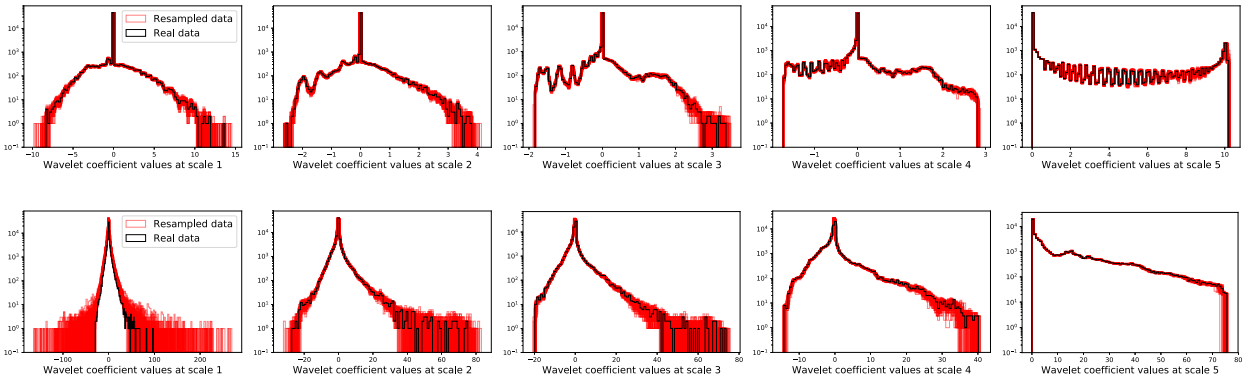

FIGURE 6.11: Histograms of the wavelet coefficient values for a five scales starlet transform of the resampled data sets and the original data. On top, the original data is the image of a square defined in 6.2. On the bottom, it is the simulated image of Cassiopeia A.

6.4.2 Comparison with Monte-Carlo

Our aim in developing a new resampling method was to be able to create resampled data sets mimicking a Monte-Carlo centered on the real data. For that reason, our second test is to compare the distribution of a hundred resampled data sets to that of a hundred Monte-Carlo realizations.

A first way to do so is to compare the spread in the distributions obtained through both methods by looking at their standard deviation. As the image of a square defined in Figure 6.2 and the simulated image of Cassiopeia A are both produced from an underlying model, we can generate Monte-Carlo realizations of both images to compare their spread to that of a hundred constrained bootstrap resamples.

Figure 6.19 shows a comparison of the resampled data sets and Monte-Carlo histograms and the standard deviation of each bin for both examples. It highlights in both cases the great adequacy between the standard deviation of the resampled data sets and that of the Monte-Carlo realizations. Figure 6.13 shows a comparison of the resampled data sets and Monte-Carlo wavelet scales coefficients and their standard deviations.

These Figures finally concur to assess that the constrained bootstrap method produces resampled data sets with a spread similar to that of a Monte-Carlo. This information, and the conclusion of Section 6.4.1 that this method preserves the nature of the original data tend to show that our new method is a good mimick of a Monte-Carlo centered on the original data, and is suited to estimate errors out of a single realization.

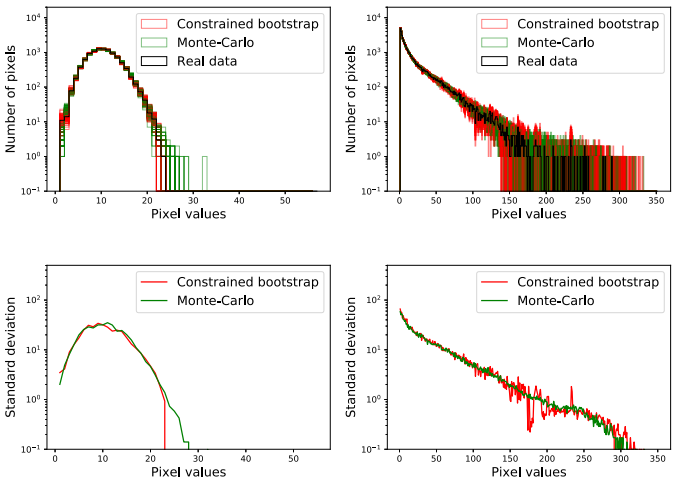

FIGURE 6.12: On the top, histograms of the original data, the resampled data sets and the Monte-Carlo realizations of both our examples. On the bottom, the standard deviations of the resampled data sets and Monte-Carlo realizations of the figure above. On the left, in the case of the image of a square defined in Figure 6.2. On the right, in the case of the simulated image of Cassiopeia A. We can see in both cases the great adequacy between the standard deviation of the resampled data sets and that of the Monte-Carlo realizations.

Summary :

- The constrained bootstrap method produces resampled data sets is far better than a block bootstrap in terms of bias : there seems to be no visible bias, apart from a small one in the first wavelet scales, that is the most sensitive to Poissonian noise.
- The spread on the histograms and wavelet coefficients of the resampled data sets appears similar to that of a Monte-Carlo.

Square image :

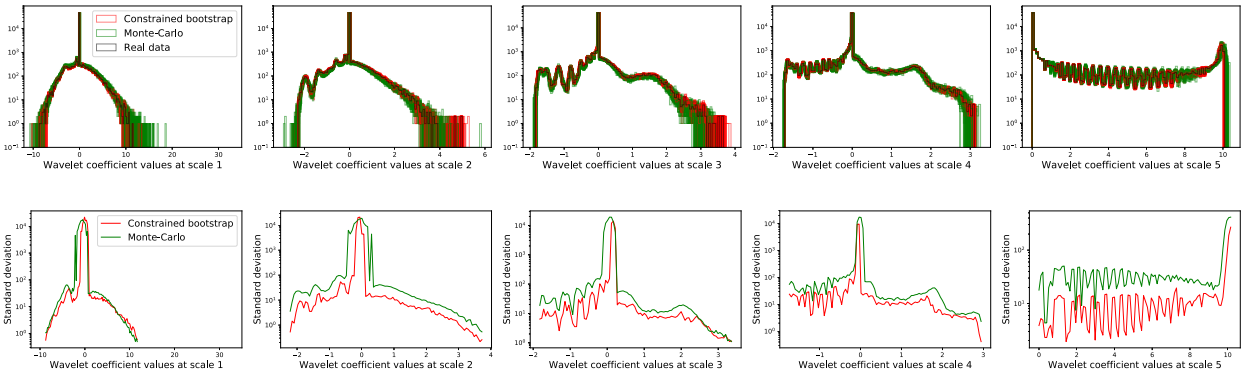

Simulated Cassiopeia A image :

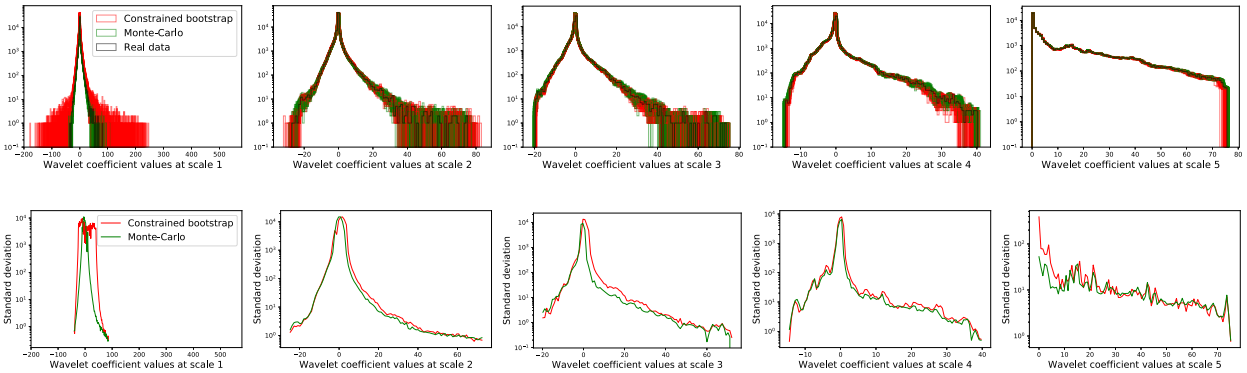

FIGURE 6.13: On the first line, histograms of the wavelet coefficient values for a five scales starlet transform of the resampled data sets, Monte-Carlo realizations and the original data of the image of a square defined in Figure 6.2. On the second line, standard deviations of the resampled data sets and Monte-Carlo realizations of the line above. On the third and fourth lines, the same is shown in the case of the simulated Cassiopeia A image.

6.5 A closer look at the spread

In order to assess the physical significance of the error bars our new constrained bootstrap method could retrieve for a given non-linear estimator, we have to compare the spread of the results with that of Monte-Carlo realizations in a more complex case than simple histograms or wavelet coefficients. As our main goal is to estimate errors for the pGMCA algorithm, we could use pGMCA as the estimator for this comparison. However, these tests would be very time consuming, so we preferred trying another estimator that will also be of use in the second part of this thesis. It is also a good way to test our method with another non-linear estimator and make sure it does not produce biases.

6.5.1 The P_2 criterion

The criterion we decided to use is the quadrupole power-ratio, or P_2. It consists in calculating the second multipole moment in a circular aperture centered on the centroid of an image, with a radius big enough to cover most of the subject of the image. Powers of the multipole expansion P_2 is then obtained by integrating this term over the circle. This method is useful to quantify the asymmetries of a quasi-circular object in an image. It will be more extensively described in Chapter 7.

The P_2 parameter is non-linear and focuses on the morphology of the image, but in a different way than pGMCA. It makes it a good test for the spread and to confirm the absence of bias in our constrained bootstrap. Once again, we use our simulated image of Cassiopeia A as the original image, but this time we take a look at the variation of the biases and the spreads depending on the mean number of counts per pixel in the original image.

Figure 6.14, top, shows the results. It appears there are no obvious biases whatever the statistics in the images are, confirming that our method produces unbiased resampled data sets. However, we can also see the spreads do not noticeably change with the mean number of counts per pixel, which should be the case if we want to mimick the spread between Monte-Carlo realizations. This example shows our method does not always produce significant spreads, so it cannot be trusted to produce physically significant error bars on any non-linear estimator on Poissonian data sets.

If we look at the differences between the values taken by a randomly chosen pixel in a hundred resampled data sets, we have an explanation : Figure 6.14, bottom, shows that most of the time, the value of the pixel in the resampled data sets does not change from the original one. For that reason, there is not enough mixing between the different data sets and the spread does not evolve in a proper way.

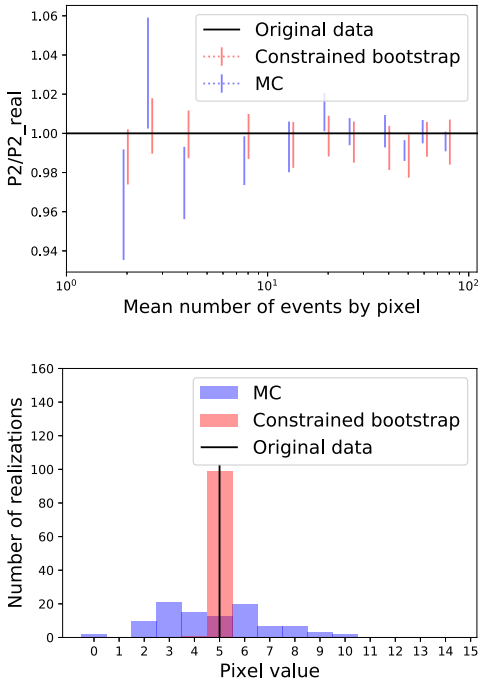

FIGURE 6.14: On top, error bars showing the spread between the 10th and the 90th percentiles of the P_2 results and normalized by the P_2 of the original data, depending on the mean number of counts per pixel in the original image. In red, the P_2 was applied on a hundred images resampled by our constrained bootstrap and, in blue, on a hundred Monte-Carlo realizations of the same underlying model as the original data. On the bottom, the spread of the values taken by a given pixel for a hundred realizations. We can see that with our constrained bootstrap, the pixel's value varies extremely rarely.

6.5.2 Adding some mixing to get a better spread

A first attempt at adding some mixing in our constrained bootstrap method was to slightly modify the second step of our method. Instead of only changing the pixels that need to be changed to obtain the new histogram defined in the first step, we change all the pixels and give them a new value probabilistically in the same way as our old second step did. It should result in a better mixing from a resampling to another, which is confirmed by Figure 6.15, right, that corrects the problem observed in Figure 6.14, bottom. However, this additional mixing makes it more probable for a given pixel to have a mean value over a hundred realizations different from its original value. For that reason, biases may appear, that we observe in Figure 6.15, left.

Figure 6.15, right, shows that our additional mixing successfully corrects the evolution of the spread as a function of the mean number of counts per pixel. However, the fact that it also adds biases makes this solution irrelevant.

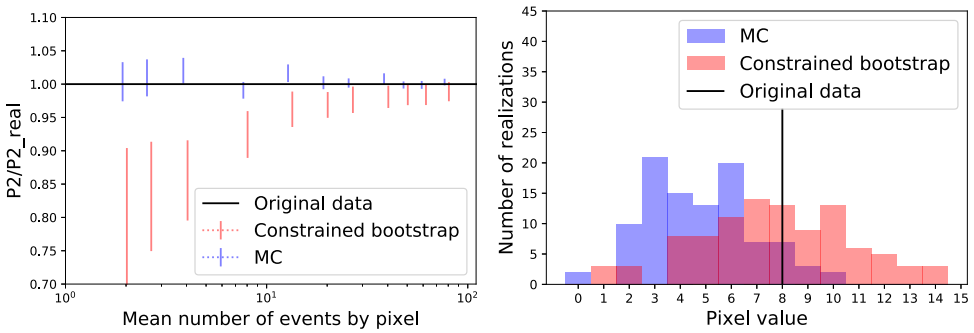

FIGURE 6.15: Same Figure as Figure 6.14, this time showing a comparison between Monte-Carlo realizations and our constrained bootstrap with more mixing in the second step.

6.5.3 Step 3

Another way to add variances to the results is to add a mixing step to our method. The second step, without our recent modification, only modified pixels associated with specific values and let a part of the data unchanged. The aim of this last step is to induce variations in the distribution of the data without modifying the histogram.

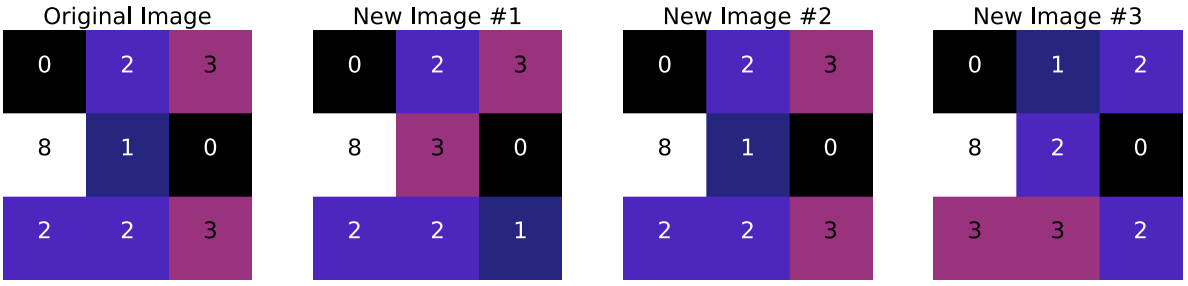

FIGURE 6.16: Illustration of the third step of our method with New Image 3 of Figure 6.9. The first image on the left is the image created in our second step in which the desired histogram was imposed. The three images on the right are three realizations of our third step. Here the histogram stays the same as the original, the pixels are just shuffled in a probabilistic way. We can notice that the zero pixels do not move, as they are not allowed to, and that the 8 pixel also stays at the same place : being substantially higher than the others, its probability to be exchanged is weak. The second new image is the same as the original : it is possible not to change anything in this step, and the smaller the image, the more likely it is to happen.

To do so, we randomly browse the list of all values in the histogram, and for every one in it we select the value in the list of available values that it will replace. In the beginning, the list of available values is the list of all values as well, that we update gradually. Every value in the available list has a probability to be chosen deriving from the probability for a Poisson realization of the initial value to equal it. In the example presented in Figure 6.16, the list of values and the list of available values are both equal to $[1, 2, 3, 8]$ in the beginning. We will browse this list and successively exchange the pixels associated with each value with pixels associated with another value. For example, if we begin by 2, the probability for the new value to be any of the available values 1, 2, 3 or 8 is proportional to the probability to obtain this value through a Poisson drawing of 2. This way, the values close to 2 are the most probables, while 8 is highly improbable to reach : the main features of the image will be preserved, but spatial variations will be created.

We then exchange as many as possible of the pixels associated with the original value with those of the new one, and we take off the new value from the list of available values when all its associated pixels have been exchanged. If necessary, we draw another value from this updated list to exchange the remaining pixels associated with the old values. In our example, let us say we drew the value 1. There are three 2 pixels to replace and only one pixel equal to 1. So we attribute the value 2 to the 1 pixel, we update the list of available values to $[2, 3, 8]$ and draw a new value. If this time we draw 3, we exchange the two remaining 2 pixels with the two 3 pixels. The list of values to exchange is then updated to $[1, 3, 8]$, the 2 pixels having been placed elsewhere already, and the list of available values becomes $[2, 8]$ as the places of 1 and 3 pixels have already been chosen.

We proceed in this way for every value in the histogram, thus inducing a local variation in the pixels' values that causes the spatial distribution to change without modifying the main features of the data. Our probabilistic exchange of values indeed makes it very unlikely to affect highly contrasted structures while tiny variations in poorly contrasted places are to be observed. Our example could end up producing New Image 3 of Figure 6.16. By construction, the zero pixels have not moved and, thanks to our probabilistic selection process, the main feature, here the 8 pixel, has not been affected. Only pixels taking values between 1 and 3 have changed, thus introducing spatial variations.

In order to avoid extreme drawings that would have a bad influence on the whole new data set, we can apply this third step on subsets of it. For example, we can separate our original image in a collection of squares and apply this last step on every one of them independently. The same goes with a data cube, that can be separated in smaller cubes.

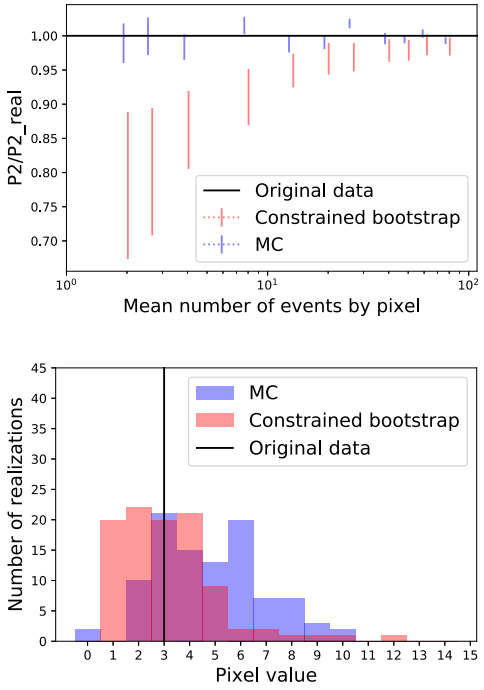

FIGURE 6.17: Same Figure as Figure 6.14, this time showing a comparison between Monte-Carlo realizations and our constrained bootstrap with a third step.

However, Figure 6.17 shows the same issue as Figure 6.14 : even if the variances evolve as desired, biases are introduced by this new step. For that reason, it cannot be used as such.

6.5.4 Compromise between bias and variance

Our desperate attempts to obtain consistent variances and unbiased results at the same time have put us in a classic but upsetting position for a statistician : finding some compromise between biases and inconsistent variances.

We tried and succeeded in alleviating the effects of our modified second step or that of our third step, either by applying the mixing on a given fraction of the total number of pixels or by imposing more strictly the mean value of each pixel on a hundred realizations. In every cases, it diminished both the biases and the evolution of the spread depending on the mean number of counts per pixel. However, whatever the solution we chose and the parameters we could play with, the results were still biased, and the spread unsatisfactory. As an example, Figure 6.18 shows the biases and spreads obtained for one of our most successful attempts.

It was obtained by considering more pixels as isolated in our first step, adding mixing in the second step but constraining the probabilities used to change the pixels' values. We will not expand on this as this solution was not retained.

As a matter of fact, instead of introducing a slightly better spread at the expense of small biases, we decided to give up the idea of obtaining a physically significant spread, at least for the moment, in order to concentrate on obtaining unbiased results. As we will see in the next Section, this solution, even though disappointing, can still be useful for estimating error bars of a non-linear estimator. Thus, we keep our new constrained bootstrap method as presented in Section 6.3, with its two original steps.

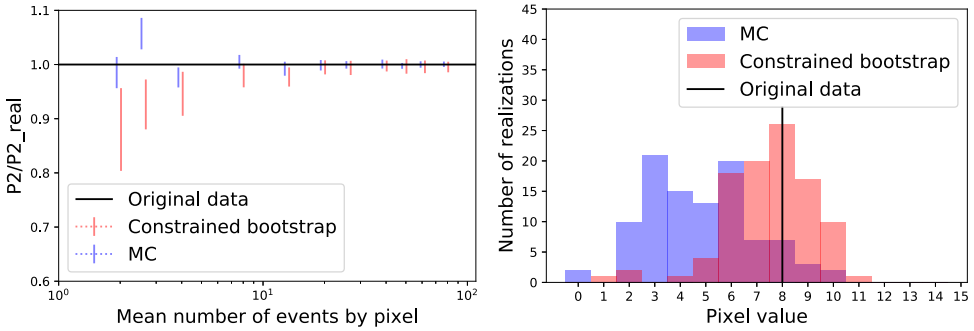

FIGURE 6.18: Same Figure as Figure 6.14, this time showing a comparison between Monte-Carlo realizations and our constrained bootstrap with more mixing in the second step.

Summary :

- Applying our new constrained bootstrap method to estimate error bars of the P_2 estimator has shown that in this case the method is not biased, but has a spread inconsistent with that of a Monte-Carlo.
- Adding some mixing in the method improves the spread, but increases the biases. For our use of this method, it is better to favour the absence of biases, so we do not modify the constrained bootstrap method and accept, for now, the inconsistent spread it produces.

6.6 Application to pGMCA

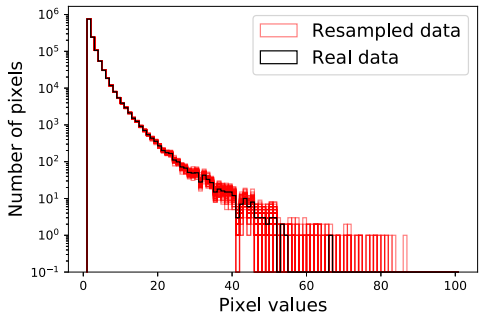

FIGURE 6.19: Histograms of the resampled data sets and the original data, the Cassiopeia A real data cube between 5.5 and 7.5 keV.

Now that our new constrained bootstrap method has been proven able to produce unbiased resamplings surrounding the original data without modifying its nature, we can generate resampled data sets from the real data from Cassiopeia A and apply the pGMCA algorithm on them.

Figure 6.19 presents the histograms of the real data cube of Cassiopeia A as seen by *Chandra* between 5.5 and 7.5 keV and the resampled data sets obtained thanks to our method. Figure 6.20 shows the wavelet scales coefficients of the original and resampled data sets. It appears the resampled data sets are not biased, or marginally. Figure 6.21 confirms it by showing the results of a pGMCA applied on the real and the resampled data sets. Unlike Figure 6.3, we now cannot spot any bias in the spectra retrieved by the algorithm. Our method proposes an unbiased way to estimate error bars on Poissonian data sets, well suited for pGMCA.

However, as stated in Section 6.5, the spreads produced are inconsistent. For that reason, the error bars retrieved by our constrained bootstrap method do not have a physical significance. Nevertheless, they constitute an interesting way to assess the robustness of a given estimator. The different resamplings explore initial conditions slightly different from the original data, thus evaluating the dependence of our results on the initial conditions.

This new constrained bootstrap method is a first and promising attempt at retrieving error bars for non-linear estimators on Poissonian data sets, a problem that is often not trivial. In non-linear processes, errors frequently cannot be propagated correctly, so the calculation of sensitive parameters and the estimation of errors after an extensive use of an advanced data analysis tool could benefit from this method. We will work in the future on a way to constraint the variance of the results to be more closely related to that of a set of Monte-Carlo realizations in order to ensure the physical significance of the obtained error bars. In a second time, we could also imagine developing this constrained bootstrap method to other types of data, thus providing a more general way to retrieve error bars in non-linear problems. The main difficulty in this development would be the discrete nature of the data that is supposed when working on the histograms, and that is already ensured by the Poissonian nature of the data sets. However, a wisely chosen way to discretize the data could surely solve this problem.

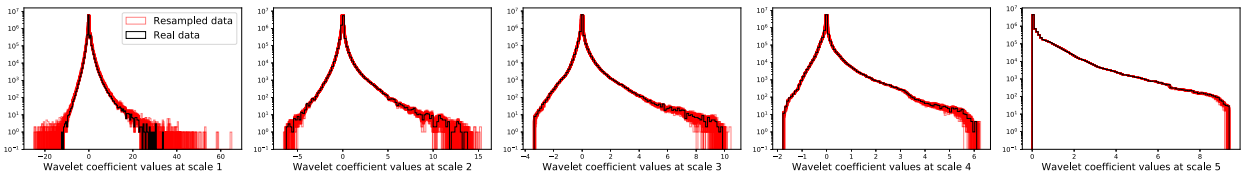

FIGURE 6.20: Histograms of the wavelet coefficient values for a five scales starlet transform of the resampled data sets and the original data, the Cassiopeia A real data cube between 5.5 and 7.5 keV.

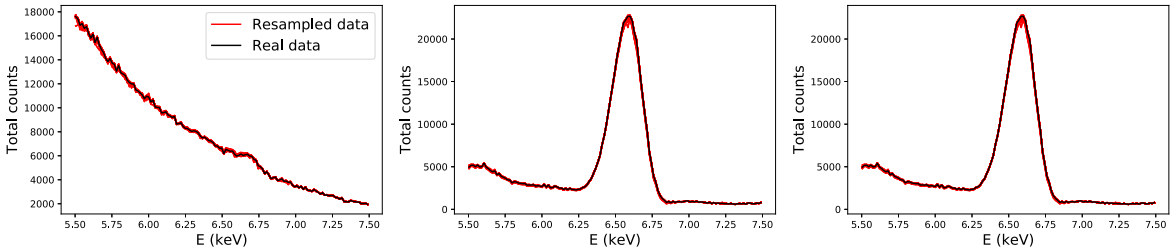

FIGURE 6.21: Spectrum of the synchrotron, red- and blue-shifted Fe structures retrieved by pGMCA on the 5.5-7.5 keV energy band on real data and on a set of 100 constrained bootstrap resamples. The bias we observed in Figure 6.3 between the real Cassiopeia A data and its block bootstrap resamples no longer exists with our new constrained bootstrap method.

Summary :

- Our new constrained bootstrap method is well adapted to retrieve unbiased error bars for a non-linear algorithm such as pGMCA applied on Poissonian data sets.
- The variances being inconsistent, the method does not produce physically significant error bars, but can help assessing the robustness of a non-linear algorithm around given initial conditions.
- Our new constrained bootstrap method is a first and promising attempt at retrieving error bars for non-linear estimators on Poissonian data sets, a problem that is often not trivial. We will try in future works to find new solutions to the problem of variances.

Part II

Applications

CHAPTER 7

ASYMMETRIES IN THE EJECTA DISTRIBUTION OF CASSIOPEIA A

Now that we have introduced our BSS method, we can finally use it for physical applications. Here, we will investigate further the asymmetries of the line emissions in Cassiopeia A, that we already noticed when applying GMCA around the Fe K line emission in Section 4.6. This chapter presents the study published in Picquenot et al. (2021).

7.1 Introduction

Cassiopeia A is among the most studied astronomical objects in X-rays and arguably the best-studied SNRs. Investigation of the distribution of metals on sub-parsec scales is possible because it is the youngest core-collapse SNR in the Milky Way (about 340 years old ; Thorstensen et al., 2001), its X-ray emission is dominated by the ejecta metals (Hwang & Laming, 2012), and it is relatively close (3.4 kpc ; Fesen et al., 2006). Cassiopeia A benefits from extensive observations (about 3 Ms in total by *Chandra*), making it an ideal laboratory to probe simulation predictions regarding the distribution of ejecta metals.

In the last few years, 3D simulations of core-collapse supernovae have begun to produce testable predictions of supernovae explosion and compact object properties in models using the neutrino-driven mechanism (see reviews by Janka et al., 2016; Müller, 2016). In particular, explosion-generated ejecta asymmetries (Wongwathanarat et al., 2013; Summa et al., 2018; Janka, 2017) and neutron star kick velocities (Thorstensen et al., 2001) appear to be key elements in core-collapse supernovae simulations that Cassiopeia A's data can constrain. Although the asymmetries of the surrounding medium swept up by the forward shock also have a clear impact that is difficult to decorrelate from the effects of asymmetries in the explosion, Orlando et al. (2016) has explored the evolution of the asymmetries in Cassiopeia A thanks to simulations beginning from the immediate aftermath of the supernova and presenting the 3D interactions of the remnant with the interstellar medium. Similar simulations presenting the evolution of a Type Ia SNR over a period spanning from one year after the explosion to several centuries afterwards have been made by Ferrand et al. (2019), showing that asymmetries present in the original supernova can still be observed after centuries. The same may go with the core-collapse SNR Cassiopeia A, and a better knowledge of its 3D morphology could lead to a better understanding of the explosion mechanisms, by providing a way to test the simulations.

An accurate mapping of the different elements' distribution, the quantification of their relative asymmetries, and their relation to the neutron star motion would for example allow us to probe the simulation predictions that heavier elements are ejected more asymmetrically and more directly opposed to neutron star motion than lighter elements (Wongwathanarat et al., 2013; Janka, 2017; Gessner & Janka, 2018; Müller et al., 2019). On this topic, this Chapter can be seen as a follow-up to Holland-Ashford et al. (2020), the first study to quantitatively compare the relative asymmetries of different elements within Cassiopeia A, but that suffered from difficulty separating and limiting contamination in the elements' distribution. Moreover, in that analysis, the separation of the blue- and red-shifted parts of these distributions was not possible.

Here, we intend to fix these issues by using pGMCA to retrieve accurate maps for each element's distribution, allowing us to investigate further their individual and relative physical properties. The new images thus obtained suffer from less contamination by other components, including the synchrotron emission, that is more efficiently removed. It also offers the opportunity to separate the blue- and red-shifted parts of the elements' distribution, thereby facilitating a 3D mapping of the X-ray emitting metals and a comparison of their relative asymmetries. Specifically, pGMCA is able to disentangle detailed maps of a red- and a blue-shifted parts in the distributions of Si, S, Ca, Ar and Fe, thus providing new and crucial information about the 3D morphology of Cassiopeia A.

Summary :

- Cassiopeia A is the youngest core-collapse SNR in the Milky Way. It is also very bright and widely studied, making it a perfect laboratory to probe simulation predictions regarding the distribution of ejecta metals.
- Recent simulations have shown some asymmetries present in the initial explosion can still be detected after centuries in the SNR. A better knowledge of the asymmetries in Cassiopeia A could help understand the explosion mechanisms.
- In particular, an accurate mapping of the different elements' distribution could help probing the simulation predictions that heavier elements are ejected more asymmetrically and more directly opposed to neutron star motion than lighter elements.

7.2 Method

Here we will describe our method to retrieve images with pGMCA, quantify their asymmetries and obtain error bars thanks to our constrained bootstrap.

7.2.1 Nature of the data

For our study, we used *Chandra* observations of the Cassiopeia A SNR, which was observed with the ACIS-S instrument in 2004 for a total of 980 ks (ObsID : 4634, 4635, 4636, 4637, 4638, 4639, 5196, 5319, 5320). We used only the 2004 dataset to avoid the need to correct for proper motion across epochs. The event lists from all observations were merged in a single data cube. The spatial (of 2 arcsec) and spectral binning (of 14.6 eV) were adapted so as to obtain a sufficient number of counts in each cube element. No background subtraction or vignetting correction has been applied to the data.

7.2.2 Image Extraction

For component separation, we used pGMCA, that is more suited for Poissonian data sets : in GMCA, the noise is supposed to be Gaussian. Even with that biased assumption, the results were proven to be reliable, as could be seen in Figure 4.10. However, a proper treatment of the noise is still relevant : it increases

the consistency of the spectral morphologies of the retrieved components and makes the algorithm able to disentangle components with a fainter contrast.

The algorithm was applied to the Cassiopeia A *Chandra* observations by creating data cubes for each energy band around O, Fe L, Mg, Si, S, Ar, Ca and Fe K (see Figure 7.1). These energy bands were chosen to be large enough to have the leverage to allow the synchrotron continuum to be correctly retrieved and narrow enough to avoid contamination by other line emissions. pGMCA being a fast-running algorithm, the final energy bands were chosen after tests to find the best candidates for both criteria. For each band, the initial number of components n was 3 : the synchrotron emission and the blue- and red-shifted parts of the line emission. We then tested for 4 and 5 components to ensure extra components were not merged into our components of interest. We also tested with 2 components to verify our assumption on the presence of blue- and red-shifted parts was not imposing the apparition of a spurious component. For each emission line, we then chose n as the best candidate to retrieve the most seemingly meaningful components without spurious images.

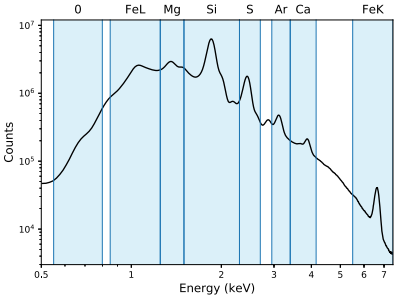

FIGURE 7.1: Spectrum of Cassiopeia A obtained from the combination of the deep *Chandra* 2004 observations. The BSS algorithm was applied in each individual energy band represented by the shaded regions.

For each analysis, the algorithm returns a tuple of n images and associated spectra. And for each analysis, the algorithm was able to retrieve a component that we identify as the synchrotron emission (a power-law spectrum and filamentary spatial distribution, see Chapter 8 for similar images) and multiple additional thermal components with strong line features. We were able to identify two associated images with shifted spectra from the theoretical emission line energy for all these line features except O, Fe L and Mg.

7.2.3 Quantification of Asymmetries

Once obtained the images of blue- and red-shifted parts for every major emission line in Cassiopeia A, a quantitative way to analyze and compare their asymmetries is to use the power-ratio method (PRM). This method was developed by Buote & Tsai (1995) and previously employed for use on SNRs (Lopez et al., 2009; Lopez et al., 2009, 2011). It consists of calculating multipole moments in a circular aperture positioned on the centroid of the image, with a radius that encloses the whole supernova remnant. Powers of the multipole expansion P_m are then obtained by integrating the mth term over the circle. To normalize the powers with respect to flux, they are divided by P_0, thus forming the power ratios P_m/P_0. For a more detailed description of the method, see Lopez et al. (2009).

P_2/P_0 and P_3/P_0 convey complementary information about the asymmetries in an image. The first term is the quadrupole power-ratio and quantifies the ellipticity/elongation of an extended source, while the second term is the octupole power-ratio and is a measure of mirror asymmetry. Hence, both are to be compared simultaneously to ascertain the asymmetries in different images.

Here, as we want to compare asymmetries in the blue- and red-shifted part of the elements' distribution, the method is slightly modified. In a first step, we calculate the P_2/P_0 and P_3/P_0 ratios of each element's total distribution by using the sum of the blue- and red-shifted maps as an image. Its centroid is then an approximation of the center-of-emission of the considered element. Then, we calculate the power ratios of the blue- and red-shifted images separately using the same center-of-emission. Ultimately, we normalize the power ratios thus obtained by the power ratio of the total element's distribution :

$$P_i/P_{0\ \textit{(shifted / total)}} = \frac{P_i/P_{0\ \textit{(red or blue image)}}}{P_i/P_{0\ \textit{(total image)}}} \tag{7.1}$$

Where $i = 2$ or 3 and $P_i/P_{0\ \text{(red or blue image)}}$ is calculated using the centroid of the total image. That way, we can compare the relative asymmetries of the blue- and red-shifted parts of different elements, without the comparison being biased by the original asymmetries of the whole distribution.

7.2.4 Error bars

We applied pGMCA on a hundred resamplings obtained thanks to the constrained bootstrap introduced in Chapter 6 for each emission line, and plotted the different spectra we retrieved around the ones obtained on real data. As stated in Chapter 6, the spread between the resamplings has no physical sgnificance, but helps evaluating the robustness of the algorithm around a given set of original conditions. The blue-shifted part of the Ca line emission, a very weak component, was not retrieved for every resamplings. In this case, we created more resamplings in order to obtain a hundred correctly retrieved components. The faintest components are the ones showing the largest spread, as can be seen in Figure 7.3 and Figure 7.4, highlighting the difficulty for the algorithm to retrieve them in a consistent way on a hundred slightly different resamplings.

To obtain the error bars for the PRM plot of the asymmetries, we applied the PRM to the hundred images retrieved by pGMCA on the resamplings. Then, in each direction we plotted error bars representing the interval between the 10^{th} and the 90^{th} percentile and crossing at the median. We also plotted the PRM applied on real data. Although our new constrained bootstrap method ensures the Poissonian nature of the data to be preserved in the resampled data sets, we see that the results of pGMCA on real data are sometimes not in the 10^{th}-90^{th} percentile zone, thus suggesting there may still be some biases. It happens mostly with the weakest components, showing once more the difficulty for pGMCA to retrieve them consistently out of different data sets presenting slightly different initial conditions. However, even when the results on real data are not exactly in the 10^{th}-90^{th} percentile zone, the adequacy between the results on real and resampled data sets is still good, and the relative positioning for each line is the same, whether we consider the results on the original data or on the resampled data sets.

Summary :

- We used the 1 Ms *Chandra* observation of Cassiopeia A.
- We applied pGMCA on energy bands around O, Fe L, Mg, Si, S, Ar, Ca and Fe K. For Si, S, Ar, Ca and Fe K we retrieved two images associated to spectra slightly red- or blue-shifted.
- We used the power-ratio method to quantify the images asymmetries. P_2/P_0 quantifies the ellipticity/elongation of an extended source, while P_3/P_0 is a measure of mirror asymmetry.
- To obtain the error bars for the PRM plot of the asymmetries, we applied the PRM to the hundred images retrieved by pGMCA on the constrained bootstrap resamplings. Then, in each direction we plotted error bars representing the interval between the 10^{th} and the 90^{th} percentile and crossing at the median.

7.3 Results

Here we present the images and spectra obtained by pGMCA, the PRM plots and the fitting of the retrieved spectra in `Xspec`. We also discuss our interpretation of the shifted components as blue- and red-shifted parts of the elements' distribution.

7.3.1 Images retrieved by pGMCA

By applying the pGMCA algorithm on the energy bands surrounding eight emission lines shown in Figure 7.1, we were able to retrieve maps of their spatial distribution associated with spectra, successfully disentangled from the synchrotron emission or other unwanted components. The O, Fe L and Mg lines were only retrieved as single features each associated with a spectrum, whereas Si, S, Ar, Ca and Fe K were retrieved as two different images associated with spectra we interpret as being the same emission line slightly red- or blue-shifted. Figure 7.2 shows the total images for all eight line emissions, obtained by summing the blue- and red-shifted parts when necessary. It also indicates the centroid of each image that is adopted in the PRM. Figure 7.3 shows the red- and blue-shifted parts of five line emissions, together with their associated spectra, while Figure 7.4 presents the images of O, Fe L and Mg together with their respective spectra.

	Red-shifted part	Blue-shifted part
Si	0.60	0.40
S	0.61	0.39
Ar	0.63	0.37
Ca	0.80	0.20
Fe K	0.70	0.30

TABLE 7.1: Fractions of the counts in the total image that belong to the red-shifted or the blue-shifted parts, for each line.

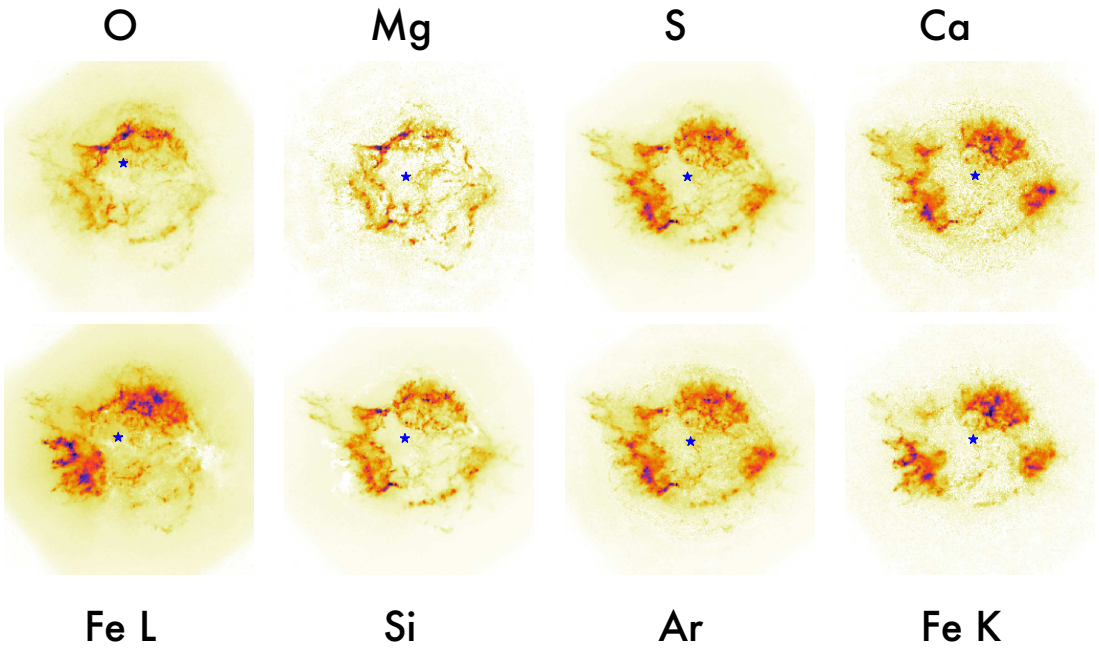

FIGURE 7.2: Total images of the different line emissions' spatial structure as retrieved by pGMCA. The blue dot represents the image centroid adopted in the PRM analysis. The color scale is in square root.

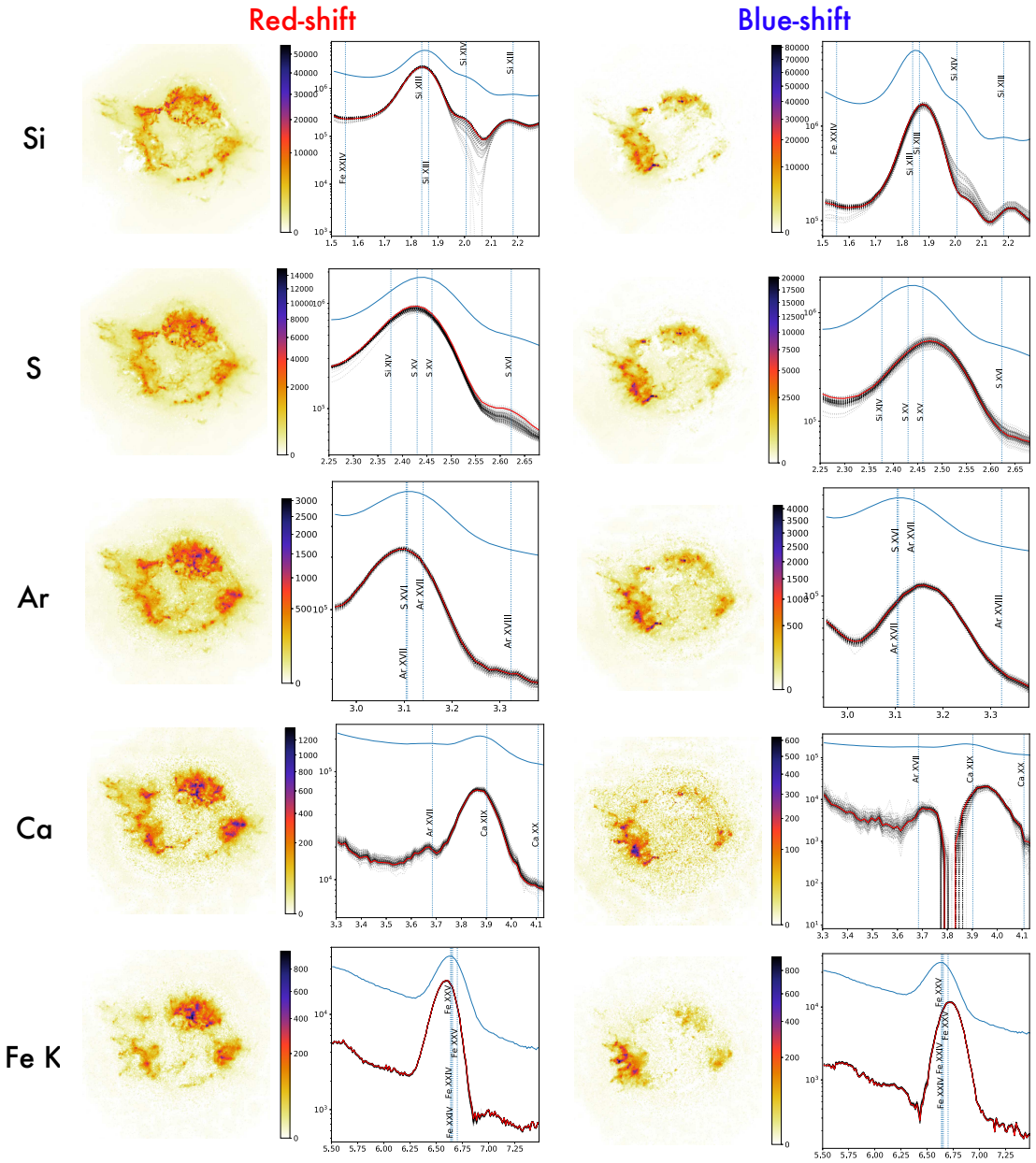

FIGURE 7.3: Red- and blue-shifted parts of the Si, S, Ar, Ca and Fe line emission spatial structures and their associated spectrum as found by pGMCA. The spectra in red correspond to the application of the algorithm on real data, while the dotted gray spectra correspond to the application on a hundred constrained bootstrap resamplings. The dotted lines represent the energy of the brightest emission lines for a non-equilibrium ionization plasma at a temperature of 1.5 keV and ionization timescale of $log(\tau) = 11.3$ cm^{-3} s produced using the atomic database for X-ray plasma spectral modeling AtomDB[1]. These parameters are the mean value of the distribution shown in Figure 2 of Hwang & Laming (2012). The color scale is in square root.

7.3.2 Discussion on the retrieved images

The fact that our algorithm fails to separate a blue-shifted from a red-shifted part in the O, Mg, and Fe L images is not surprising. At 1 keV, we infer that a radial speed of 4000 km s^{-1} would lead to a ΔE of about 13 eV, which is below the spectral bin size of our data.

We see in Figure 7.2 that while the O and Mg images are highly similar, they are both noticeably different from the images of the other line emissions. Both the O and Mg images exhibit similar morphology to the optical images of O II and O III from Hubble (Fesen et al., 2001; Patnaude & Fesen, 2014). The intermediate mass elements (heavier than Si) share interesting properties : their spatial distributions appear similar in Figure 7.2, and the division into red- and blue-shifted parts as found by pGMCA allows us to investigate their three-dimensional morphology. We also notice that the maps of Si and Ar are similar to the Ar II in infrared (DeLaney et al., 2010b).

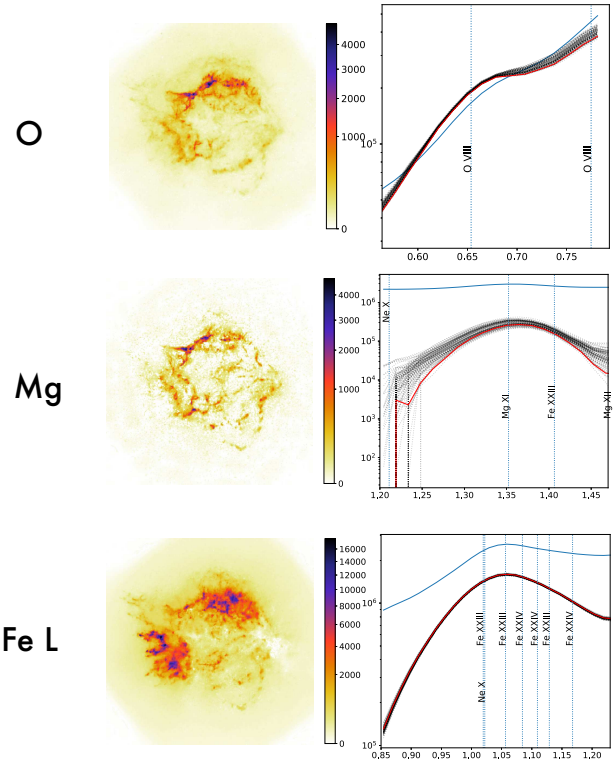

FIGURE 7.4: Images of the O, Mg, and Fe L line emission spatial structures and their associated spectrum as found by pGMCA. The spectra in red correspond to the application of the algorithm on real data, while the dotted gray spectra correspond to the application on a hundred constrained bootstrap resamplings. The color scale is in square root.

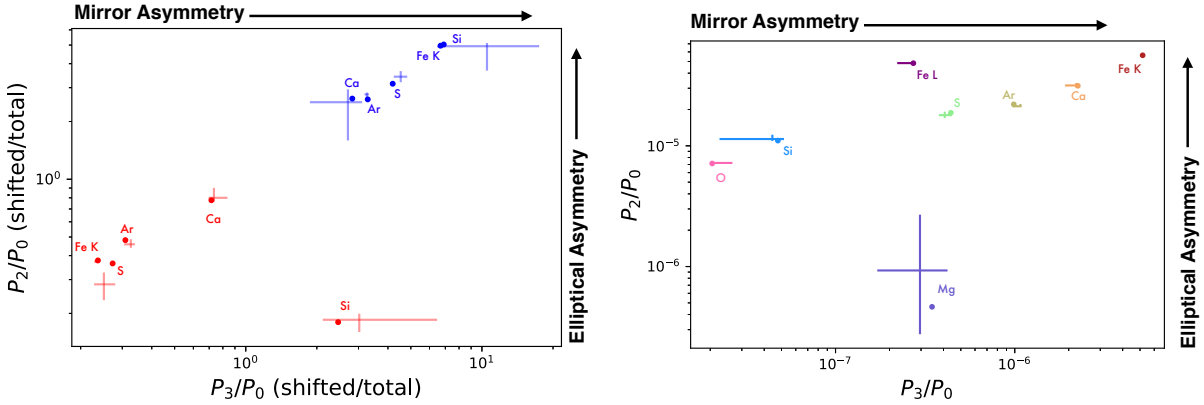

FIGURE 7.5: The quadrupole power-ratios P_2/P_0 versus the octupole power-ratios P_3/P_0 of the images retrieved by pGMCA. On the left, the total images of Figure 7.2 ; on the right, the red- and blue-shifted images of Figure 7.3, normalized with the quadrupole and octupole power-ratios of the total images. The dots figure the results given by the images obtained with real data, and the crosses the 10^{th} and 90^{th} percentiles obtained with pGMCA on a hundred constrained bootstrap resamplings, with the center of the cross being the median.

[1] www.atomdb.org

7.3.3 PRM plots

Here we present the plots described in Section 7.2.3. Figure 7.5, left, presents the quadrupole power-ratios P_2/P_0 versus the octupole power-ratios P_3/P_0 of the total images from Figure 7.2. Figure 7.5, right, shows the quadrupole power-ratios versus the octupole power-ratios of the red- and blue-shifted images presented in Figure 7.5 normalized with the quadrupole and octupole power-ratios of the total images (Figure 7.2) as defined in Equation 7.2.3.

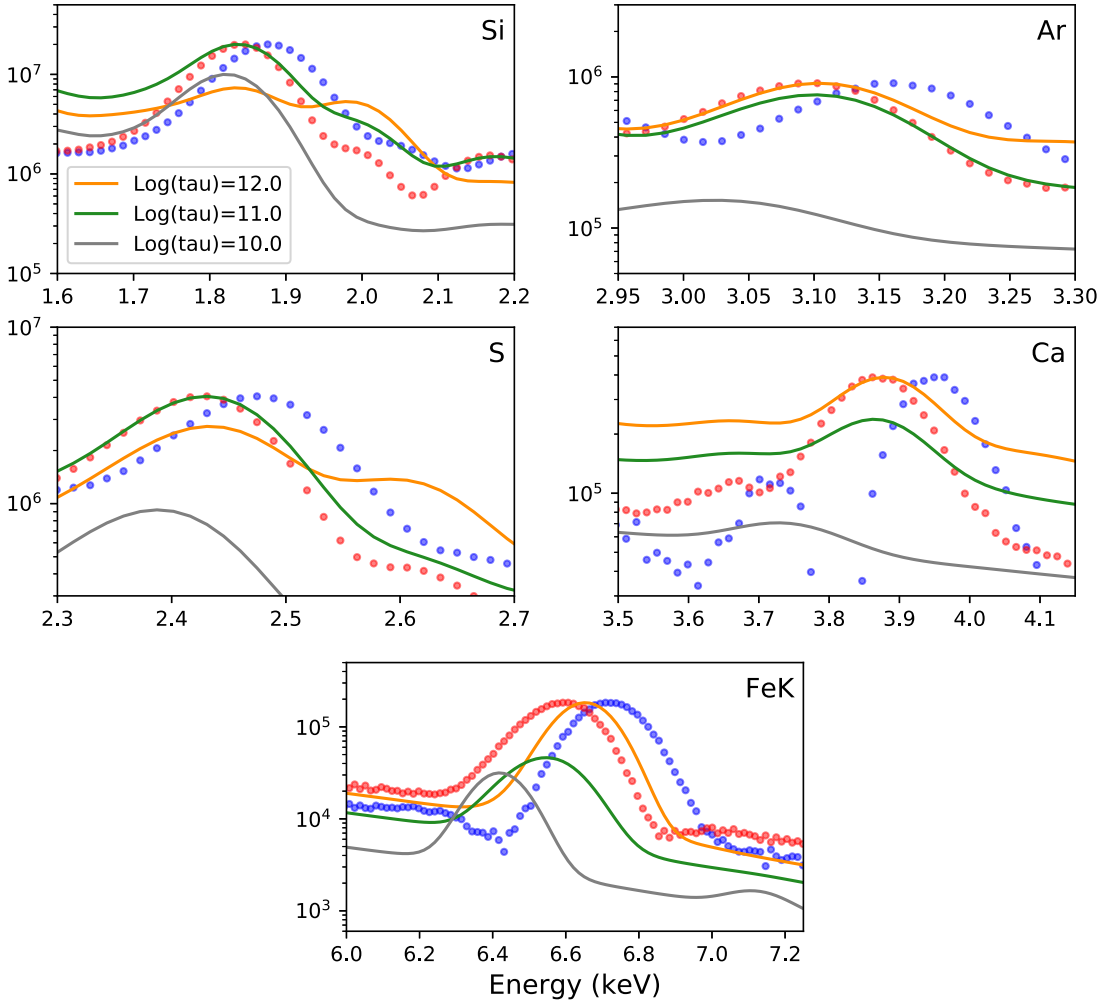

FIGURE 7.6: Comparison of our red/blue spectra versus *pshock* Xspec models with different ionization timescales.

7.3.4 Velocity and ionization impact on line centroid

The centroid energy of emission lines can be shifted for different reasons such as Doppler effect or evolution of the ionization timescale. In Figure 7.6 we compare the spectral model *pshock* at different ionization timescales with the spectra that we identified as red red- and blue-shifted in Figure 7.3. The temperature of the model was fixed to 2 keV based on the temperature map of Figure 1 of Hwang & Laming (2012). The effective area and redistribution matrix from observation ObsID : 4634 were used. We can see that as the ionization time scale τ increases the line centroid, which is a blend of multiple lines, shifts to higher

energies. This is most visible in the Fe K region where a large number of lines exist. We note that the spectral component that we identified as blue-shifted is well beyond any ionization state shown here and reinforces the idea that this component is dominated by velocity effect. The situation is less clear for the red-shifted component where the shift in energy is not as strong. We also do not precisely know which reference line it can be compared to.

It is interesting to note that for the purpose of measuring a velocity effect while minimizing the confusion with ionization effects, the Ar and Ca lines provide the best tools. As a matter of fact, for $\tau > 10^{11}$ cm^{-3} s, the centroid of the main Ar and Ca lines shows no evolution given the CCD energy resolution.

7.3.5 Discussion on the retrieved spectra

As stated before, it is the spectra retrieved together with the aforementioned images that allow us to identify them as " blue- " or " red-shifted " components. Here we will expand on our reasons to support these assertions.

The spectra in Figure 7.3 are superimposed with the theoretical positions of the main emission lines in the energy range. In the case of Si, the three lines in the spectra corresponding to Si XIII and Si XIV features that are shifted together from one side to another of the theoretical positions. The previous Section shows that this shifting is not primarily due to an ionization effect, as the ratio Si XIII/Si XIV is roughly equal in both cases. The same goes with S, where two lines corresponding to S XV and S XVI are shifted together while keeping a similar ratio.

The Ar, Ca and Fe K cases are single lines shifted around the theoretical position of the line emission, making the " blue- " and " red-shifted " identifications straightforward. Figure 7.3 also shows that the Si emission is dominated by Si XIII, the S by S XV, the Ar by Ar XVII (Ar XVII has a much higher intensity than S XVII at 1.5 kev), the Ca by Ca XIX and the Fe K by Fe XXV (Fe XXV has a much higher intensity than Fe XXIV).

A word on the Ca blue-shifted emission : this component is very weak and in a region where there is a lot of spatial overlap, making it difficult for the algorithm to retrieve. For that reason, the retrieved spectrum has a poorer quality than the others, and it was imperfectly found on some of our constrained bootstrap resamplings. Consequently, we were compelled to run the algorithm on more than a hundred resamplings and to select the accurate ones to obtain a significant envelop around the spectrum obtained on the original data.

7.3.6 Spectral analysis

Using the spectral components retrieved for each data subset shown in Figure 7.3, we carried out a spectral fitting assuming a residual continuum plus line emission in *Xspec* (*power-law* + *gauss* model). In this analysis, the errors for each spectral data point are derived from the constraint bootstrap method presented in Chapter 6. This method eliminates a bias, critical to pGMCA, associated with the classical bootstrap method but underestimates the true statistical error. Therefore no statistical errors on the line centroids are listed in the Table as in addition systematic errors associated to ACIS energy calibration are likely to be the dominant source of uncertainty.

The resulting line centroid and equivalent velocity shifts are shown in Table 7.2. To transform the shift in energy into a velocity shift, a rest energy is needed. The ACIS CCD spectral resolution does not resolve the line complex and cannot easily disentangle between velocity and ionization effects. However, given

the range of ionization observed in Cas A ($10^{11} - 10^{12}$ cm^{-3} s, see Figure 2 of Hwang & Laming, 2012), there is little effect of ionization on the dominant line for Si, S, Ar and Ca as discussed in more details in Section 7.3.4. The rest energy line was chosen as the brightest line for a non-equilibrium ionization plasma for a 1.5 keV temperature and $log(\tau) = 11.3$ cm^{-3} s, the mean values observed in Figure 2 of Hwang & Laming (2012).

For the specific case of the Si line, a very large asymmetry in the red/blue velocities is observed. This could be due to a possible energy calibration issues near the Si line as shown by DeLaney et al. (2010a) in a comparison of ACIS and HETG line centroids, resulting in a systematic blue-shift effect in ACIS data. The Si XIII* line in Table 7.2 uses a corrected rest line energy to illustrate systematic uncertainties associated with calibration issues.

For the Fe K complex of lines we rely on the analysis of DeLaney et al. (2010a) who derived an average rest line energy (1.8615 Å, 6.6605 keV) by fitting a spherical expansion model to their 3D ejecta model. Note that with this spectral analysis, what we measure here is the radial velocity that is the flux weighted over the entire image of the associated component. Therefore we are not probing the velocity at small angular scale but the bulk velocity of the entire component.

With the caveats listed above we notice an asymmetry in the velocities where ejecta seem to have a higher velocity towards us (blue-shifted) than away from us, even in the case of Si XIII after calibration corrections.

The large uncertainties associated with the energy calibration and the choice of rest energy has little impact on the delta between the red- and blue-shifted centroids and hence on the ΔV. We note that we observe only little variations in ΔV as a function of element mass with an average value of 6000 km s^{-1}.

Line	E_{rest} keV	E_{red} keV	E_{blue} keV	ΔV km/s	V_{red} km/s	V_{blue} km/s
Si XIII	1.8650	1.860	1.896	5787	804	4983
Si XIII*	1.8730	1.860	1.896	5762	2081	3681
S XV	2.4606	2.439	2.489	6092	2632	3460
Ar XVII	3.1396	3.110	3.180	6684	2826	3858
Ca XIX	3.9024	3.880	3.967	6684	1721	4963
Fe complex	6.6605	6.599	6.726	5716	2768	2948

TABLE 7.2: Spectral fitting on individual lines and resulting velocities. Si and Fe line rest energy are taken from DeLaney et al. (2010a). The Si XIII* uses a different rest energy, the one needed to match the ACIS and HETG Si velocities discussed in DeLaney et al. (2010a), to illustrate possible ACIS calibration issues.

Summary :

- The shifting of the spectra relatively to the theoretical positions are not primarily due to ionization effects : the components retrieved by pGMCA indeed present a red- and a blue-shifted parts.
- The velocities of the bllue-shifted components seem greater than the red-shifted ones, but it could be due to calibration issues.

7.4 Physical Interpretation

7.4.1 PRM plots

Figure 7.5, left, shows that the distribution of heavier elements is generally more elliptical and more mirror asymmetric than that of lighter elements in Cassiopeia A : O, Si, S, Ar, Ca, and Fe emission all exhibit successively higher levels of both measures of asymmetry. This result is consistent with the recent observational study of Cassiopeia A by Holland-Ashford et al. (2020), suggesting that the pGMCA method accurately extracts information from X-ray data cubes without the complicated and time-consuming step of extracting spectra from hundreds or thousands of small regions and analyzing them individually.

Similar to the results of Holland-Ashford et al. (2020) and Hwang & Laming (2012), Mg emission does not follow the exact same trend as the other elements : it has roughly an order of magnitude lower elliptical asymmetry (P_2/P_0) than the other elements. In contrast to Holland-Ashford et al. (2020) and Hwang & Laming (2012), our Mg image (as shown in Figure 7.4) presents a morphology highly different from that of the Fe L ; we believe that pGMCA was able to retrieve the Mg spatial distribution with little continuum or Fe contamination.

Figure 7.5 presents the relative elliptical and mirror asymmetries of the blue- and red-shifted ejecta emission compared to the total ejecta images (Figure 7.2). A value of " 1 " indicates that the velocity-shifted ejecta has equivalent levels of asymmetry as the full bandpass emission. In the cases where we can clearly disentangle the red- and blue-shifted emission (i.e. Si, S, Ar, Ca, and Fe K, described in previous paragraphs), we see that the red-shifted ejecta emission is less asymmetric than the blue-shifted emission. This holds true both for elliptical asymmetry P_2/P_0 and mirror asymmetry P_3/P_0. Thus, we could physically describe the red-shifted ejecta distribution as a broad, relatively symmetric plume whereas the blue-shifted ejecta would be more similar to a dense knot. This interpretation matches with the observation that most of the X-ray emission is from the red-shifted emission as we can also see in the flux ratios shown in Table 7.1 and in the images of Fig. 7.3, suggesting that there was more mass ejected away from the observer, neutron star, and blue-shifted ejecta knot. We note that there is not a direct correlation between ejecta mass and X-ray emission due to the position of the reverse shock, the plasma temperature and ionization timescale, but the indication that most of the X-ray emission is red-shifted is consistent with our knowledge of the ^{44}Ti distribution (see Sect. 7.4.4 for a more detailed discussion).
Furthermore, in all cases, the red-shifted ejecta emission is more circularly symmetric than the total images, and the blue-shifted ejecta is more elliptical/elongated than the total images. Moreover, the red-shifted ejecta is more mirror symmetric than the blue-shifted ejecta, though both the red-shifted and blue-shifted Si are more mirror asymmetric than the total image. The latter result may suggest that the red-shifted and blue-shifted Si images' asymmetries sum together such that the total Si image appears more mirror symmetric than the actual distribution of the Si.

7.4.2 Three-dimensional distribution of heavy elements

Figure 7.7 shows the centroids of the blue- and red-shifted parts of each line emission relative to the center-of-explosion of Cassiopeia A, giving information about the bulk three-dimensional distribution of each component. We note that the red-shifted ejecta is all moving in a similar direction, as is the blue-shifted ejecta, all with bulk displacement. We will see in Section 7.4.4 that this is consistent with previous works on Cassiopeia A investigating the ^{44}Ti distribution with *NuSTAR* data.

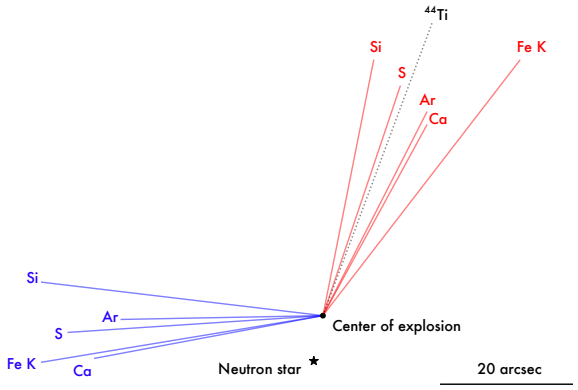

FIGURE 7.7: Centroids of the blue- and red-shifted parts of each line emission and their distance from the center of explosion of Cassiopeia A. For reference, we added the direction of motion of the ^{44}Ti in black, as shown in Figure 13 of Grefenstette et al. (2016). Only the direction of the black vector is relevant, as its norm is arbitrary.

We note that the blue-shifted ejecta is clearly moving in a different direction than the red-shifted ejecta, but not directly opposite. Figure 7.8 shows more clearly the angles between the blue- and red-shifted parts of each elements, and it appears they are all comprised between $90°$ and $140°$. This finding provides evidence against a jet/counter-jet explosion mechanism being responsible for the explosion and resulting expansion of ejecta in Cassiopeia A. We note a trend where heavier elements exhibit increasingly larger opening angles than lighter elements, which can give insights on asymmetry generation in the core of the supernovae close to the proto-neutron star. This is consistent with recent simulations (see Wongwathanarat et al. 2013, 2017; Janka 2017) predictions that asymmetric explosion processes result in the heaviest ejecta synthesized closest to the core exhibiting the strongest levels of asymmetry.

7.4.3 Neutron star velocity

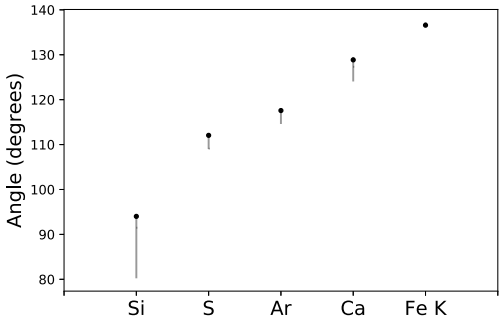

FIGURE 7.8: Angles between the directions of the red- and blue-shifted centers of emission from the center of explosion for each element.

The neutron star in Cassiopeia A is located SE of the explosion site, moving at a velocity of $\sim$340 km s^{-1} SE in the plane of the sky (Thorstensen et al., 2001). Figure 7.7 is consistent with past findings, and supports the theory that neutron stars are kicked opposite the bulk motion of ejecta. We find that the redshifted ejecta is moving almost directly opposite the neutron star motion, and we find that the bulk emission is from redshifted ejecta (See Table 7.1). This correlation provides evidence for the theory that neutron stars are kicked opposite the direction of bulk ejecta motion, which is consistent with the conservation of momentum with the ejecta (Wongwathanarat et al., 2013; Müller, 2016; Bruenn et al., 2016; Janka, 2017). Specifically, observations have provided evidence for the " gravitational tug-boat mechanism " of generating neutron star kicks asymmetries proposed by Wongwathanarat et al. (2013); Janka (2017), where the neutron star is gravitationally accelerated by the slower moving ejecta clumps, opposite the bulk ejecta motion.

It is impossible to calculate the neutron star line-of-sight motion by examining the neutron star alone, as its spectra contains no lines to be doppler-shifted. However, limits on its 3D motion can be placed by assuming it moves opposite the bulk of ejecta and examining the bulk 3D motion of ejecta. Grefenstette et al. (2017) studied ^{44}Ti emission in Cassiopeia A and found out that the bulk ^{44}Ti emission was tilted 58° into the plane of the sky away from the observer, implying that the neutron star is moving 58° out of the plane of the sky toward the observer. This finding is supported by 3D simulations of IIb progenitor by Wongwathanarat et al. (2017); Jerkstrand et al. (2020) which conclude that the neutron star is moving out of the plane of the sky with an angle of $\sim 30°$. The results of this Chapter support the hypothesis that, if the neutron star is moving away from the bulk of ejecta motion, the neutron star is moving towards us. Furthermore, we can tentatively conclude that the neutron star was accelerated toward the slower-moving blue-shifted ejecta, which further supports the gravitational tugboat mechanism. Furthermore, we could tentatively conclude that the NS was accelerated toward the slower-moving blue-shifted ejecta, which would further support the gravitational tugboat mechanism. The strong levels of asymmetry exhibited by the blue-shifted emission combined with the lower flux would imply that the blue-shifted ejecta is split into relatively small ejecta clumps, one of which would possibly be the source of the neutron star's gravitational acceleration. However, the velocities determined in Table 7.2 contradict this hypothesis, as the blue-shifted clumps seem to move faster.

7.4.4 Comparison with ^{44}Ti

^{44}Ti is a product of Si burning and is thought to be synthesized in closed proximity with iron. The ^{44}Ti spatial distribution has been studied via its radioactive decay with the NuSTAR telescope and revealed that most of the material is red-shifted and in appearance does not seem to follow the Fe-K X-ray emission (Grefenstette et al., 2014; Grefenstette et al., 2016). In our study we have found that 70% of the Fe K X-ray emission (see Table 7.1) is red-shifted and that the mean direction of the Fe K red-shifted emission shown in Figure 7.7 is compatible with that of the ^{44}Ti as determined in Grefenstette et al. (2016) Figure 13. Yet, we can see the mean ^{44}Ti direction is not perfectly aligned with the mean red-shifted Fe K direction. This may be caused by the fact that what we see in X-rays is material heated by the reverse shock, which if asymmetric will offset the Fe K X-ray emission spatial distribution.

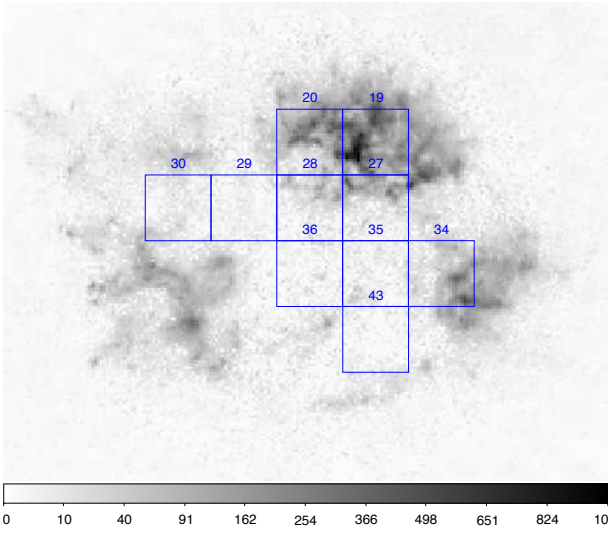

FIGURE 7.9: Image of the Fe K red-shifted component overlaid with the extraction regions used for the ^{44}Ti *NuSTAR* study of Grefenstette et al. (2017). The regions 19 and 20 which dominate our image in terms of flux have respective velocities moving away from the observer of 2300 ± 1400 and 3200 ± 500 km s^{-1}.

In Figure 7.9, we overlay the spectral extraction regions of Grefenstette et al. (2016) with our red-shifted component image. The regions 19 and 20 which dominate our Fe K red-shifted component image have respective velocities of 2300 ± 1400 and 3200 ± 500 km s^{-1}, values that are compatible with our measured value of $\sim$2800 km s^{-1} shown in Table 7.2.

Concerning our Fe K blue-shifted component map, its X-ray emission is fainter and located mostly in the South-East of the source (see Figure 7.3). This X-ray emission is spatially coincident with a hotspot in the NuSTAR map corresponding to region 46 in Figure 2 of Grefenstette et al. (2016).

Note that blue-shifted ^{44}Ti emission is harder to detect for NuSTAR than a red-shifted one as it is intrinsically fainter and in addition, any emission that is blue-shifted induces the displacement of the 78 keV beyond NuSTAR effective area, therefore loosing one of the two decay lines for the detection.

Summary :

- **Morphological Asymmetries :** An extensive study of the asymmetries shows the distribution of heavier elements is generally more elliptical and mirror asymmetric in Cassiopeia A, which is consistent with simulation predictions. For the elements we were able to separate into a red- and a blue-shifted parts, it appears that the red-shifted ejecta is less asymmetric than the blue-shifted one. The red-shifted ejecta can then be described as a broad, relatively symmetric plume, while the blue-shifted ejecta can be seen as a dense knot. This is consistent with the fact that most of the emission is red-shifted, hence implying there was more mass ejected away from the observer.
- **Three-dimensional Distribution :** The mean directions of the red- and blue- shifted parts of each elements are clearly not diametrically opposed, disfavouring the idea of a jet/counter-jet explosion mechanism. The angles between the red- and blue-shifted parts becoming wider as the elements get heavier, we get an insight on the asymmetries closer to the core and the proto-neutron star.
- **Neutron star Velocity :** The neutron star is moving directly opposite the direction of the red-shifted parts of the heavier elements, supporting the idea of a " gravitational tug-boat mechanism " generating neutron star kicks asymmetries. Our findings also support the idea that the neutron star is moving away from the bulk of ejecta motion, which is mainly red-shifted, hence towards us. However, we find the blue-shifted clumps to be faster than the red-shifted ones, which is not fully consistent with the gravitational tug-boat mechanism.
- **Comparison with ^{44}Ti :** Our findings are consistent with the *NuSTAR* data of ^{44}Ti. Its direction is similar to that of the red-shifted Fe K emission, but a slight difference could be explained by the fact that parts of the Fe K heated by the reverse shock are not visible in the *NuSTAR* data.

CHAPTER 8

ENERGY DEPENDENCY OF SYNCHROTRON X-RAY RIMS

The previous application of our method only focused on the line emissions retrieved in the *Chandra* data of Cassiopeia A. However, the continuous emission images and spectra we can retrieve from the same data also contain plenty of useful information that would be worth investigating. In this chapter, we will explore some aspects of the synchrotron emission of Cassiopeia A, that the detailed and clean images obtained by pGMCA allow us to study with more accuracy than ever, in particular at low energies.

8.1 Thin X-ray rims in the synchrotron emission

The synchrotron emission has been briefly presented in Section 1.3.1 : electrons accelerated in the forward shocks of young supernova remnants can radiate electromagnetic energy over the entire spectrum. It is mostly seen in radio wavelengths, but can also be seen in X-rays thanks to the fast (> 1000 km.s^{-1}) shocks of young SNRs. In some cases, the X-ray brightness fades downstream and produces a bright shell-like structure of rims and filaments.

8.1.1 Two main models

A better knowledge of the synchrotron rims could help constrain the downstream magnetic field and structure. However, the mechanisms at stakes to explain the formation of these rims are not perfectly known : there are two main models as well as models ranging between these two that could account for the existence of thin rims structures in the synchrotron emission in X-rays (see Tran et al., 2015).

The first main model, nicknamed " loss-limited model " assumes the thickness of the synchrotron filaments in X-rays to be caused by the energetic loss of high energy electrons. An electron is supposed to travel only a certain distance before its energy drops enough so that its radiation cannot be seen in X-rays anymore. This distance is determined both by the advection (bulk motion of plasma) and the diffusion mechanisms (random motion of electrons at small scales), which makes it dependent on energy (see Ressler et al., 2014). More specifically, the rims produced according to this model are supposed to be narrower at higher energies. However, this model requires a strong magnetic field amplification to successfully account for the formation of thin rims.

The second model, or " damped model ", proposes an alternative to the presence of a strong field amplification by considering the thin rims could reflect magnetic field variations : the magnetic field could be damped downstream of the shock and prevent electrons from radiating efficiently, thus reducing synchrotron flux at all wavelengths. A damped mechanism is supposed to produce energy-independent rims, making the evolution of their width in relation to the energy an interesting discriminating factor between the two models. However, both mechanisms can possibly coexist, making this criterion harder to interpret.

Tran et al. (2015), Figure 2, proposes a range of radio and X-ray rim profiles showing the influences of both the magnetic field and the damping length. It highlights the similarity between the effects of a strong magnetic field and a small damping length on lowering the dependence in energy of the rim widths, proving difficult to probe a model with no further information on the magnetic field. In the same paper, a moderate narrowing of the rim widths were found in Tycho's SNR. They were nonetheless insufficient to constraint the model. Ressler et al. (2014) came to the same conclusion concerning SN 1006.

Lastly, the filament profiles in X-rays are supposed to be sharper upstream of the forward shock, in the direction where the magnetic field is lower. Conversely, the profiles are supposed to be softer downstream. The same goes with the reversed shock.

8.1.2 Thin X-ray rims in Casiopeia A

Once again, we will use the bright and well-studied SNR Cassiopeia A to address this subject. Araya et al. (2010) investigated some properties of the synchrotron rims visible in the 1 Ms *Chandra* observation of Cassiopeia A, including a comparison between the linear profiles of some filaments in the 0.3-2.0 keV, 3.0-6.0 keV and $6.0 - 10.0$ keV energy bands. They only found a slight difference in the widths between the 0.3-2.0 keV and the 3.0-6.0 keV images, but none between the 3.0-6.0 keV and the 6.0-10.0 keV images, as shown in the Table 1 of their paper. They also found the outer regions of the forward shock to be sharper than the inner ones, but did not investigate the reverse shock as their images were too contaminated by the ejecta.

This is not in contradiction with the dependency in energy found in Tycho's SNR by Tran et al. (2015), that was qualified as " moderate ". However, we may expect the use of finer images than those exploited by Araya et al. (2010) to help finding a slight narrowing at higher energies, or on the contrary assert with more confidence that there is none. pGMCA is perfectly suited for producing clear, detailed and unpolluted images of the synchrotron at different energies ; its ability to get rid of the ejecta contamination will also allow us to explore the reverse shock in a new way.

Summary :

- In some SNRs, the synchrotron emission presents filamentary structures in X-rays, which is a sign of acceleration of the electrons at the forward shock.
- There are two main models to explain the presence of filaments in the synchrotron. In one of them, the filament profiles are supposed to narrow at higher energy while the other model does not propose any dependency in energy. Thus, the key observable is the dependency in energy of the rim widths. However, both mechanisms can coexist, making it difficult to pick one out.
- A moderate dependency in energy of the filament widths has been detected in Tycho, and only a very small one in Cassiopeia A. pGMCA is the perfect tool to produce accurate images for an in-depth study of the filament widths in Cassiopeia A at different energies. In particular, it can allow us to study this effect near the reverse shock by eliminating the ejecta contamination.

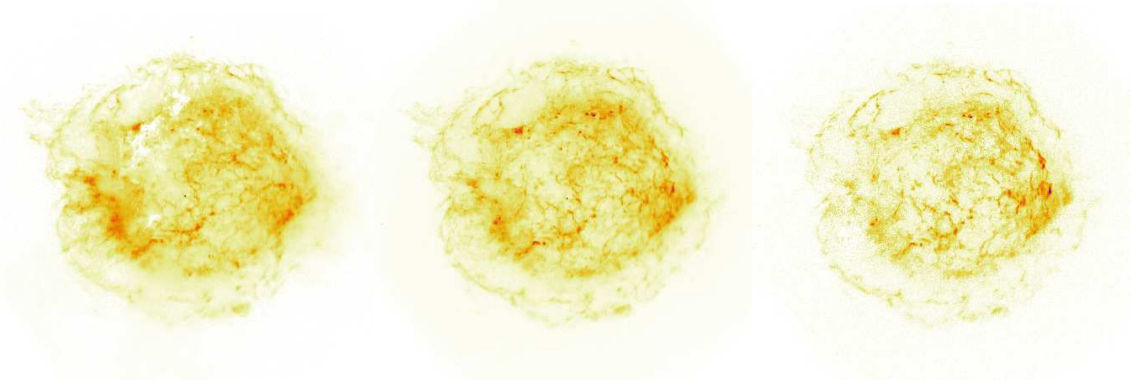

FIGURE 8.1: Images of the synchrotron retrieved by pGMCA on three energy bands. From left to right : between 0.4 and 1.7 keV, between 2.5 and 4 keV and between 5 and 8 keV. The color scale is in square root.

8.2 Using pGMCA to probe the filament widths in Cassiopeia A

As stated in Section 7.1, Cassiopeia A is the perfect extended source to showcase the possibilities of pGMCA, offering high statistics and strongly overlapping components the algorithm is well suited to disentangle. Here, we will use it to obtain three images of the synchrotron at different bandwidths, from which we will derive the linear profiles of some wisely chosen synchrotron rims.

8.2.1 Images definition

We use the same *Chandra* data of Cassiopeia A as in Section 7.2.1. Here, the spatial bin size is the native *Chandra* bin size of 0.5 arcseconds, in order to produce as detailed images as possible. To keep a good number of counts in every pixels and as we are not interested in the spectra, we chose a spectral bin size of 58.4 eV.

We applied pGMCA on three bandwidths : between 0.4 and 1.7 keV, between 2.5 and 4 keV and between 5 and 8 keV. We chose these bandwidths on different criteria : large enough for pGMCA to work properly, not too large in order not to affect a possible dependency in energy of the filament widths, and we tried as much as possible to avoid having too many line emissions in the same bandwidths. This last criterion could not be fulfilled at lower energies, and some pollution from other emissions can be seen in the first image displayed in Figure 8.1. The two other images seem clear and unpolluted, even with a square root color scale. They probably constitute the most detailed and accurate maps of the synchrotron in X-rays in Cassiopeia A to this day, especially at low energy.

8.2.2 The filament linear profiles at the forward shock

In order to compare the widths of some synchrotron rims at different energies, we defined boxes surrounding small regions crossing a filament at the forward shock. The boxes are shown in Figure 8.2, and the linear profiles obtained perpendicularly to the rims are presented in Figure 8.3.

In every boxes but in box 6, where the 0.4-1.7 keV filament is slightly tighter, the profiles show that the 5-8 keV filament is narrower than the 2.5-4 keV one, that is itself narrower than the 0.4-1.7 keV one. In boxes 2, 4 and 5, the 0.4-1.7 keV and 2.5-4 keV filaments are similar, while the 5-8 keV one is noticeably tighter. In

boxes 1 and 4 there is a visible difference between the widths of the filaments at every energy ranges, and in box 7 the 2.5-4 keV and 5-8 keV filaments have similar widths while the 0.4-1.7 keV one is noticeably larger.

Here, it appears clearly that there is a noticeable narrowing of the filaments between lower and higher energies. Our results are more explicit than those of Araya et al. (2010), Table 1, and we find this dependency to be also visible between 2.5-4 keV and 5-8 keV, not only at lower energies.

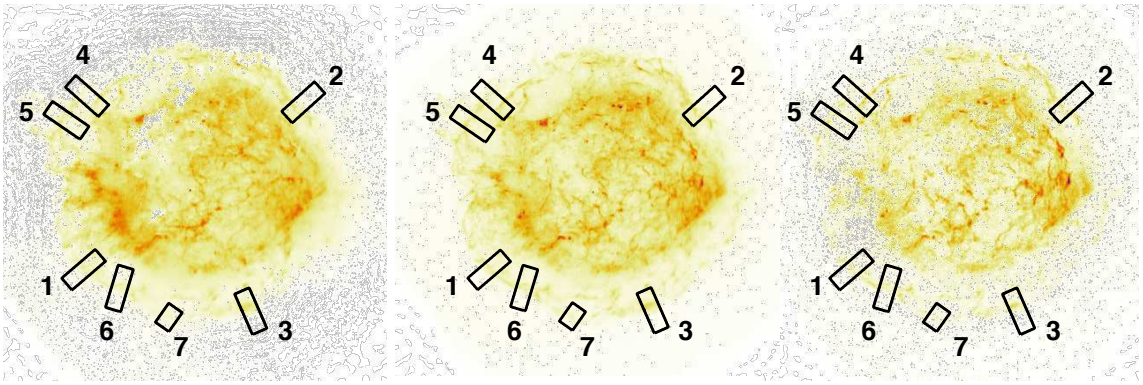

FIGURE 8.2: Boxes used to define the linear profiles at the forward shock presented on the images of the synchrotron retrieved by pGMCA on three energy bands. From left to right : between 0.4 and 1.7 keV, between 2.5 and 4 keV and between 5 and 8 keV. The color scale is in square root.

As for the sharpening of the rims upstream, the profiles in boxes 1, 2, 4 and 5 show a common trend that is consistent with our expectations, while boxes 6 and 7 show almost symmetrical profiles in every energy ranges and box 3 presents the contrary : a softening of the profile upstream.

8.2.3 The filament linear profiles at the reverse shock

We apply the same method as previously at the reverse shock. The boxes are shown in Figure 8.4, and the linear profiles obtained perpendiculary to the rims are presented in Figure 8.5.

In every boxes, the profiles show that the 5-8 keV filament is narrower than the 2.5-4 keV one, that is itself narrower than the 0.4-1.7 keV one. Here, there is a common trend for the 0.4-1.7 keV filament to be clearly larger than the others, while the 2.5-4 keV and 5-8 keV filaments have more similar widths. The 5-8 keV filaments still appear noticeably larger than the other 2.5-4 keV ones.

As for the sharpening of the rims upstream, the profiles in boxes 3 and 5 are consistent with our expectations, while box 2 shows an almost symmetrical profile in every energy ranges and boxes 1 and 4 present the contrary : a softering of the profile upstream. The filaments we considered part of the reverse shock being in a dense region, some boxes probably surround more than one filament, troubling this study. The contamination still visible in the 0.4-1.7 keV image may also play a role, as the busy 0.4-1.7 keV profiles suggest.

Once again, it appears clearly that there is a noticeable narrowing of the filaments between lower and higer energies. This is a substantial result as we could not find in the litterature any other study of that kind regarding the reverse shock rims of Cassiopeia A.

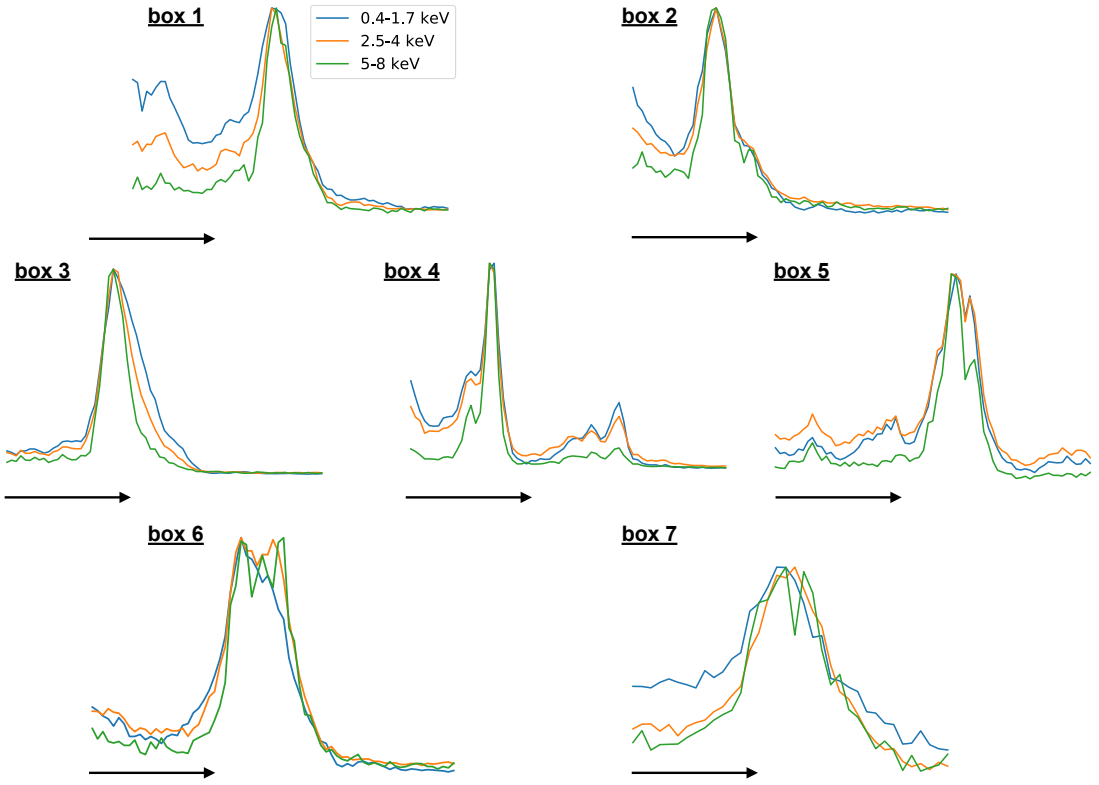

FIGURE 8.3: Linear profiles at the forward shock along the boxes presented in Figure 8.2. The profiles are normalized so that the peaks coincide. The arrows show the direction of the forward shock.

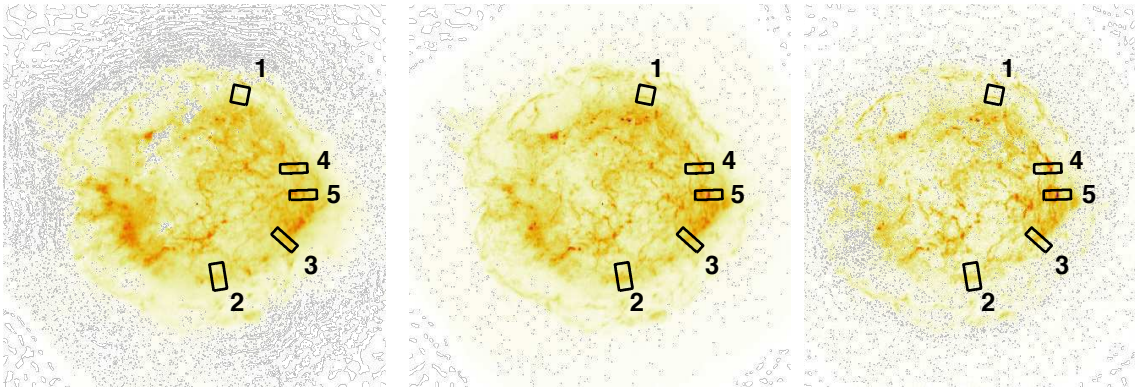

FIGURE 8.4: Boxes used to define the linear profiles at the forward shock presented on the images of the synchrotron retrieved by pGMCA on three energy bands. From left to right : between 0.4 and 1.7 keV, between 2.5 and 4 keV and between 5 and 8 keV. The color scale is in square root.

8.2.4 Unidentified filament linear profiles

Lastly, we looked at some filaments whose positions could not allow us to label clearly. A line-of-sight effect may be at stake, and these filaments could either be attached to the forward or to the reverse shock. The boxes are shown in Figure 8.6, and the linear profiles obtained perpendiculary to the rim are presented in Figure 8.7.

The profiles are almost perfectly symmetric and show a clear dependence in energy.

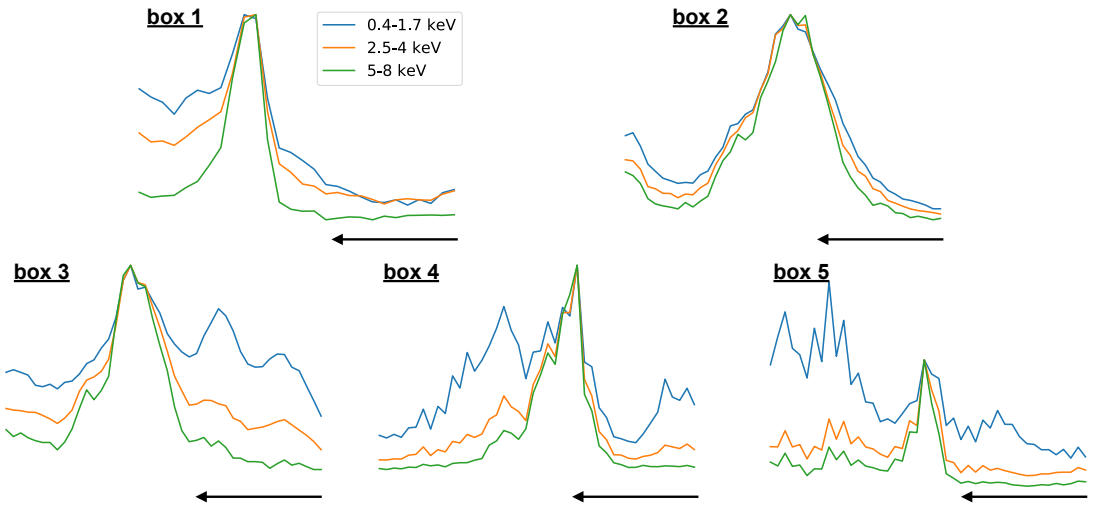

FIGURE 8.5: Linear profiles at the reverse shock along the boxes presented in Figure 8.4. The profiles are normalized so that the peaks coincide. The arrows show the direction of the reverse shock.

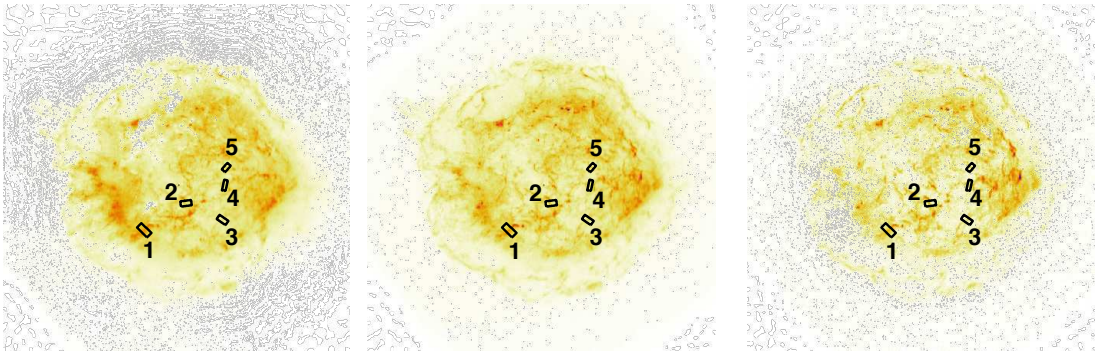

FIGURE 8.6: Boxes used to define unidentifed linear profiles presented on the images of the synchrotron retrieved by pGMCA on three energy bands. From left to right : between 0.4 and 1.7 keV, between 2.5 and 4 keV and between 5 and 8 keV. The color scale is in square root.

8.2.5 Future studies

Further investigations could be conducted to retrieve as much information as possible from the clear and detailed maps obtained by pGMCA. Our linear profiles could for example be used more quantitatively by fitting a decreasing exponential model in order to estimate their widths and compare the results to the predictions given by the current models. It would probably give us information about the magnetic field's strength. A comparison with radio data could also be lead.

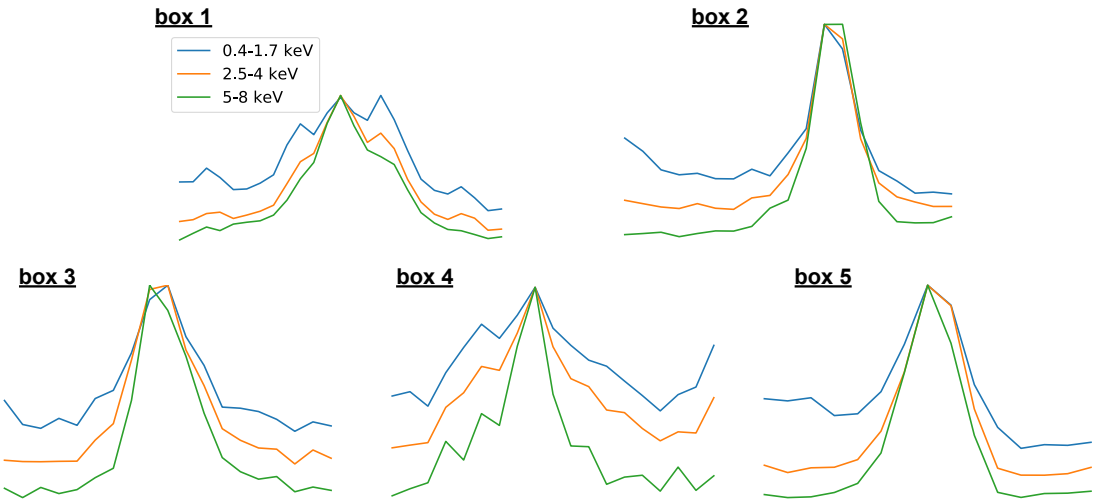

FIGURE 8.7: Unidentified linear profiles along the boxes presented in Figure 8.6. The profiles are normalized so that the peaks coincide.

Summary :

- Our study shows clearly that there is a noticeable narrowing of the synchrotron rims between lower and higer energies. We find that this this effect is also visible between 2.5-4 keV and 5-8 keV, not only at lower energies.
- This narrowing can be seen both at the forward shock and at the reverse shock.
- There is a common trend for a majority of profiles to sharpen upstream, but a non negligible part of our examples were not as conclusive.
- In future studies, fitting the linear profiles with theoretical models would allow us to compare our observations to the predictions.

CHAPTER 9

AN APPLICATION TO THE PERSEUS GALAXY CLUSTER

The two previous chapters have shown examples of applications of pGMCA to the Cassiopeia A supernova remnant. The same method could be applied on other supernova remnants to produce a similar kind of studies, or to investigate other astrophysical objects where component separation is needed to obtain either an accurate image or spectrum of a given source. However, we must emphasize the fact that high statistics are needed for a proper use of the algorithm : bright objects and deep observations are to be favoured for an extensive investigation using pGMCA.

In this chapter, we will briefly present a possible application of pGMCA on an extended source of a different kind : the Perseus galaxy cluster, both bright and extensively observed, is the perfect candidate.

9.1 Perseus in X-rays

The Perseus galaxy cluster is located in the Perseus constellation, and is the brightest cluster in the sky when seen in X-rays. The main feature observed in X-rays is a hot gas in which some giant cavities appear (see Figure 9.1). These cavities are actually bubbles of relativistic plasma that appear as holes in X-rays as they push away the hot gas. Yet, they can be observed in radiowaves and, for that reason, are known as " radio bubbles ".

The fact that the emitting hot gas is not cooling is due to heat generated by turbulent motions. That turbulence is thought to be caused by the interactions between the radio bubbles and the surrounding gas (Zhuravleva et al., 2014).

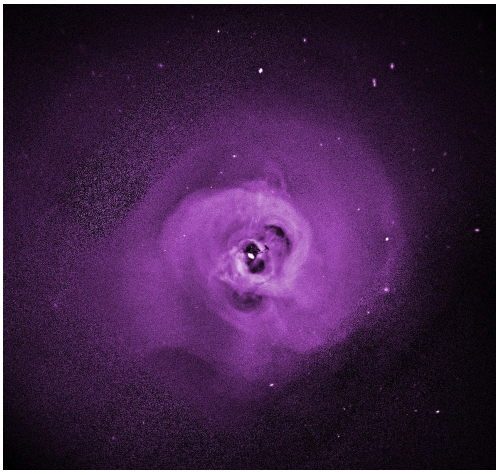

FIGURE 9.1: The Perseus galaxy cluster in X-rays, as seen by *Chandra*. The bright point source in the middle is the central black hole.

9.1.1 Filamentary structures in the Hα emission of Perseus

The Hα emission of Perseus presents complex structures for which we will search an X-ray counterpart. It shows a network of filaments similar to a mist of cold molecular clouds with warm ionized skins (see Figure 9.2). While the reservoir of gas from which the filaments form is very likely the rapidly cooling ambient intracluster medium (Peterson & Fabian, 2006), the processes that drive the filaments' ionization state, regulate their star formation rate, and sculpt their morphology has remained a persistent mystery.

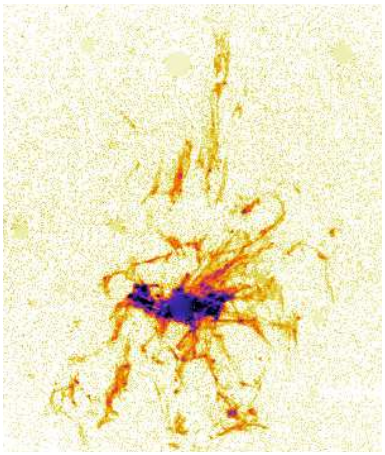

FIGURE 9.2: Hα emission of Perseus. From Conselice et al. (2001).

Some filaments are apparently draped around the rims of the radio bubbles. Yet, while uplift is certain to be a driver of some filaments morphology, other filaments are clearly infalling towards the galaxy's core, or sewed to the hot gas by magnetic fields that act as threads (Fabian et al., 2008). A soft X-ray counterpart has been detected for some filaments, which could originate from charge exchange, from the outer layers of a continuous thermal gradient in the gas forming the outer layers of cold clouds, or from both effects combined (Fabian et al., 2011; Walker et al., 2015). Understanding this soft excess may be the key to unveil the origin, and perhaps even the fate, of the filaments in cool core galaxy clusters.

9.1.2 X-ray counterpart

The X-ray counterpart of the optical filaments that was partially detected by Fabian et al. (2006) shows a structure appearing in the cold gas mass map (0.5 keV map ; Figure 12). However, this map is an indirect image resulting from a multi-temperature model fit in more than a hundred individual cells. This results in a noisy map, hampering any detailed morphological comparison. Concerning the spectral constraints, only a vague temperature estimate is possible (0.5 or 1 keV maps) and no abundances can be measured.

In Sanders & Fabian (2007), some spectral constraints are provided only in the Northern part of the filaments, outside of the core. It is assumed that each component of the multi-temperature model has the same metallicity as they cannot measure them independently. This assumption prevents a detailed measure of the metallicity of a faint cold component embedded in a hot gas.

Another analysis by Walker et al. (2015) directly extracted X-ray spectra in few portions of the filaments. In addition to degeneracy between components, focusing on small regions drastically reduces the statistics in the spectra.

The X-ray studies listed above provided either indirect imaging or spectral studies of small portions of the filaments. However, none of them could extract a detailed map of X-ray counterpart to the filamentary structures visible in the Hα emission, that would allow an in-depth investigation of the temperature, the abundances and the metallicity.

Summary :

- The Perseus galaxy cluster is the brightest cluster in X-rays and allows for deep morphological studies.
- Some filamentary structures are seen in its Hα emission. Finding an X-ray counterpart to these structures could help understanding their morphology and formation.
- None of the partial X-ray counterparts detected so far are detailed enough to allow an in-depth investigation of the temperature, the abundances and the metallicity.

9.2 Application of pGMCA

Previous studies of the X-ray counterpart of the filamentary structures seen in the Hα emission all suffer from the poor quality of the extraction from the other components. Perseus being bright and well-observed in X-rays, it constitutes a perfect target to apply our method, that will once more prove its efficiency in extracting components from entangled data sets in X-rays.

9.2.1 Results

We used the deep archival Perseus observations (1 Ms) and searched for three components with the pGMCA algorithm. Here, we masked the central black hole by inpainting it (see Section 2.4 about inpainting methods). The spectral bin size is of 43.8 eV and the spatial one is of 4 arcseconds. The results are shown in Figure 9.3. The main component is the hot gas ($\sim$ 6 keV), which looks very similar to the input dataset. The other components reveal a spiraling pattern potentially associated with a sloshing cold front and the X-ray counterpart of the optical filament, clearly disentangled for the first time and presenting an astounding morphological similarity to the filaments in Hα.

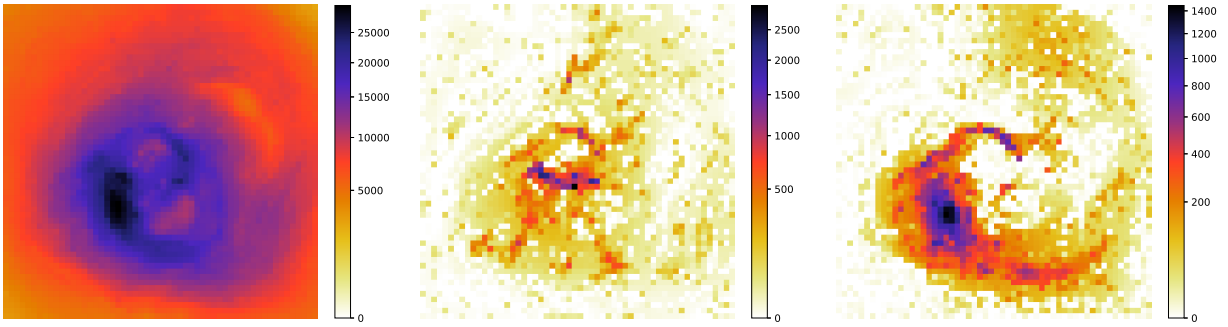

FIGURE 9.3: Images of the three components retrieved by pGMCA in Perseus. The color scale is in square root.

9.2.2 Future studies

A sudden and unsuspected event made us cancel an exchange at CfA, Boston in Spring 2020, during which we had planned to carry on with specialists of the subject our investigation of Perseus, and exploit to their full potential the images retrieved by pGMCA. This ambitious project has been postponed, and here we will settle for the description of what we intended to do.

Firstly, we planned to carry out a detailed morphological comparison between the filaments in X-rays and in the Hα emission. As the images at our disposal are clear and endowed with a lot of details, this comparison should not cause any difficulty. For example, by defining boxes as in Section 8.2.2, we could compare the widths of the filaments at different places.

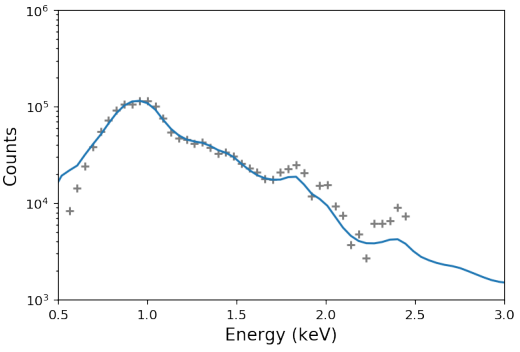

FIGURE 9.4: Spectrum of the filament component retrieved by pGMCA. An absorbed *apec* model (kT = 1keV, abundance= 0.1) is overlaid (no fit were performed). The N_H and the red-shift were taken to litterature values (Fabian et al., 2006).

Then, we intended to constrain the temperature and abundances via a spectral modeling of the X-ray spectrum of the filaments. This point is not trivial, due to the high contrast factor between the filamentary component and the others. The spectrum retrieved with the standard GMCA technique is full of discontinuities, zeros or negative values and is not suitable for a model fitting, proving the difficulty of the disentanglement (see Figure 9.4). The spectrum retrieved by pGMCA is better looking but its robustness is still to be evaluated. In particular no viable information seems to be retrieved above 2 keV, likely due to the increasing contrast with the hot component. A new development of the GMCA algorithm is planned, that will include the possibility to take into account some physical information in the separation by using a learning method. Hence, the spectrum will be forced to be of a certain kind, defined by the user, like a thermal model (see Chapter 10). A comparison of our current results with what could be obtained thanks to this future development would help us consistently study the X-ray spectrum of the filaments. However, with those caveats in mind, the spectrum shown in Figure 9.4 seems to favour a 1 keV plasma with low metallicities (0.1-0.2 solar value). This measurement, if confirmed, would suggest that the gas in the filaments is typical gas from the intra-cluster medium and does not come from highly enriched regions in the core of the cluster.

Summary :

- The application of pGMCA on the Perseus galaxy cluster gave us three images. The main component is the hot gas, and the other components reveal a spiraling pattern potentially associated with a sloshing cold front and the X-ray counterpart of the optical filament, clearly disentangled for the first time and presenting an astounding morphological similarity to the filaments in Hα.
- In future studies, we will carry out a detailed morphological comparison between the filaments in X-rays and in the Hα emission. We will also constrain the temperature and abundances via a spectral modeling of the X-ray spectrum of the filaments, but this point is more problematic. A useful new development of GMCA will be described in Chapter 10, that could help us here.

CHAPTER 10

CONCLUSION AND PERSPECTIVES

The end is nigh, the deed is done ; hear ye, hear ye reader of mine, for it is almost over... As would Tycho say, in his harsh and profound voice : “ Now is the time to conclude ! ”

In a final surge of rational thinking, we decided to split this very last chapter into two parts regarding our conclusions and perspectives, that will themselves be subdivided into a methodology and an application subparts. Enjoy yer last read, for it will last long no more !

10.1 Conclusion

Our main objective in this thesis was to explore new ways to analyze X-ray data by exploiting their multi-dimensional aspect jointly. We focused on new BSS methods needing no prior physical information, the GMCA and pGMCA algorithms, and introduced them to the high energy astrophysics field. We started with a proper introduction of the method and the underlying mathematical principles, then we tested it on toy models and explored a way to retrieve error bars, a general question and a particularly hot topic in data analysis nowadays. Finally, we presented three examples of physical applications in X-ray astrophysics.

10.1.1 Methodology

Presentation of the method :

In this thesis, we introduced to the physical analysis of extended sources in X-ray astronomy a BSS method, the GMCA algorithm and its derivative for Poissonian data sets, pGMCA. GMCA being available online to anybody who would like to use it, we thought it important to provide explanations regarding its mathematical principles suited for non-specialists. For that reason, we introduced the starlets, a particular kind of bi-dimensional wavelengths needed for this method, and the main ideas of the algorithms in a way that we hope was precise enough, understandable and not too technical. We hope that part of our work will be of use to any potential user of GMCA willing to grasp a bit of the mechanisms of the algorithm, and not simply use it as a “ black box ”.

Method performances :

Naturally, we also wanted to test GMCA and benchmark its performances in separating mixed components on toy models inspired by real X-ray observations of SNRs. We found that the images and spectra retrieved by the algorithm were faithful to the originals, but that the improper treatment of the Poissonian nature of the data caused a leakage from the brightest components to the weaker ones. This problem was partially solved by an inpainting step we added in the algorithm.

Our tests were promising, and showed that GMCA was more efficient to disentangle components from a (E, x, y) data set than any method previously used in SNR-related papers. We must however emphasize on the fact that a high number of observed photons is needed for a proper use of the algorithm. From our tests, we could say a few million counts are necessary, but this is highly data-dependent : data sets presenting overlapping, completely entangled components will require more statistics than data sets presenting already distinct components. Also, the number of components to retrieve is chosen by the user, and no automatized method can yet favorably replace that decision. In a more general way, we encourage users to try different parameters, energy ranges and numbers of components. As the algorithm is fast-running, this should not be a problem, and a human eye is still essential to assess the physical relevance of the components retrieved by the blind algorithm.

A new version of GMCA developed during our thesis, the pGMCA algorithm, refined the treatment of Poisson noise. pGMCA increased the accuracy of the results and diminished the leakage from brightest components to weaker ones. For these reasons, we used pGMCA in our applications of the method on real data from *Chandra*.

Estimation of error bars :

Lastly, we looked into the matter of error bars. Estimating errors accurately for non-linear algorithms such as GMCA, pGMCA, or any machine learning process is still an open question that goes far beyond the scope of astrophysical applications. This is a hot topic whose study would be essential for an appropriate use of complex data analysis methods in retrieving physical parameters, and for allowing the user to estimate the accuracy of the results. We have showed that using a bootstrap method to produce resamplings of a given data set could be a good way to estimate errors, but classical bootstrap methods such as the block bootstrap introduce biases by introducing additional noise : they are equivalent to a Poisson realization of a Poisson realization of the theoretical underlying model, rather than being equivalent to a Poisson realization of the model.

Hence, we developed a constrained bootstrap method that does not change the Poissonian nature of the data. Our method has little to no biases, but the spreads obtained are unsatisfying, as they are not similar to that of Monte-Carlo realizations. Thus, our method cannot be used to assess physically significant error bars ; yet, it constitutes an interesting way to assess the robustness of a given estimator. The different resamplings explore initial conditions slightly different from the original data, thus evaluating the dependency of our results on the initial conditions. It is also a promising attempt at retrieving error bars for non-linear estimators on Poissonian data sets, and we may be able in future works to improve the spread we obtain.

10.1.2 Applications

Asymmetries in Cassiopeia A :

Our first application was an extensive study of the asymmetries in the line emissions of the SNR Cassiopeia A. We used pGMCA to retrieve maps of the distributions of O, Fe L, Mg, Si, S, Ar, Ca and Fe K, and the power-ratio method to quantify their asymmetries. For Si, S, Ar, Ca and Fe K, the pGMCA algorithm retrieved two components associated with spectra slightly red- or blue-shifted from the theoretical position, giving insights on the three-dimensional morphology of Cassiopeia A.

We found that the distribution of heavier elements is generally more elliptical and mirror asymmetric in Cassiopeia A, which is consistent with simulation predictions. For the elements we were able to separate

into a red- and a blue-shifted parts, it appears that the red-shifted ejecta is less asymmetric than the blue-shifted one. The red-shifted ejecta can then be described as a broad, relatively symmetric plume, while the blue-shifted ejecta can be seen as a dense knot. This is consistent with the fact that most of the emission is red-shifted, hence implying there was more mass ejected away from the observer.

The mean directions of the red- and blue- shifted parts of each elements are clearly not diametrically opposed, disfavouring the idea of a jet/counter-jet explosion mechanism. The angles between the red- and blue-shifted parts becoming wider as the elements get heavier, we get an insight on the asymmetries closer to the core and the proto-neutron star.

The neutron star is moving directly opposite the direction of the red-shifted parts of the heavier elements, supporting the idea of a " gravitational tug-boat mechanism " generating neutron star kicks asymmetries. Our findings also support the idea that the neutron star is moving away from the bulk of ejecta motion, which is mainly red-shifted, hence towards us.

Our findings are consistent with the *NuSTAR* data of ^{44}Ti. Its direction is similar to that of the red-shifted Fe K emission, but a slight difference could be explained by the fact that parts of Fe K indirectly traced by *NuSTAR* has not been heated by the reverse shock yet. In addition, the reverse shock can be asymmetric.

Energy dependency of synchrotron X-ray rims :

In some supernova remnants, the synchrotron emission presents filamentary structures in X-rays, which is a sign of acceleration of the electrons at the forward shock. There are two main models to explain their presence in the synchrotron. In one of them, the filament profiles are supposed to narrow at higher energy while the other model does not propose any dependency in energy. Thus, the key observable is the dependency in energy of the rim widths. However, both mechanisms can coexist, making it difficult to pick one out.

Our second application of the method was on the synchrotron filaments that can be seen in Cassiopeia A. Thanks to pGMCA, we retrieved images of the synchrotron emission between three different energy bands : 0.3-2.0 keV, 3.0-6.0 keV and $6.0 - 10.0$ keV. We were then able to compare the widths of some selected filaments, and found out that there is a noticeable narrowing of the synchrotron rims between lower and higher energies. We could observe this effect both at the forward shock and, for the first time, at the reverse shock. In future studies, we could fit the linear profiles with decreasing exponentials to obtain more quantitative results and compare our observations to the predictions given by current models.

An application to the Perseus galaxy cluster :

Our last application was on the Perseus galaxy cluster. An X-ray counterpart to the filaments visible in the Hα emission has long been searched to help understanding their morphology and formation. Thanks to pGMCA, we were able to retrieve a beautiful image of this X-ray counterpart, clearly disentangled for the first time and presenting an astounding morphological similarity to the Hα emission. We also retrieved a spiraling pattern potentially associated with a sloshing cold front. In future studies, we could carry out a detailed morphological comparison between the filaments in X-rays and in the Hα emission. We could also constrain the temperature and abundances via a spectral modeling of the X-ray spectrum of the filaments.

10.2 Perspectives

Here we will present a few possibilities our thesis has opened for future works. Some concern improvements or new developments of the method, others present ideas of physical applications. Parts of these ideas are very straightforward and only require time, but some would need more research to come into being.

10.2.1 Methodology

Introduction of machine learning to take advantage of prior physical information :

As was stated in Section 9.2.2, a new development of the GMCA algorithm is planned that would allow to use prior physical information about the spectral shape of some components. The total blindness of GMCA and pGMCA regarding physics can be seen as an advantage as these algorithms are not constrained in any way by an incomplete knowledge of the components to retrieve, and allow unexpected features to appear ; but in some cases, we have such a good knowledge of the theoretical spectral shape of the component we are searching for that it would be a shame to completely miss the information. For example, when searching for line emissions or thermal components, being able to search for a specific kind of spectral shape without having to give a precise temperature or energy line to the algorithm as in GMCA's semi-blind mode, would considerably help it retrieve and disentangle faint components. That possibility could be implemented in the algorithm by making it use a metric learnt from a population of spectra of a given model.

Better spectral binning :

We have insisted throughout the thesis on the necessity to use GMCA and pGMCA on sources with good statistics to exploit these algorithms to their full potential. But even within a same source, the statistics evolve drastically depending on the energy band we consider : Cassiopeia A is more than 130 times brighter between 0.5 and 2 keV than between 6 and 7.5 keV. As we mainly focused on rather narrow energy sub-bands, this problem did not affect us. But when searching for continuum emissions on the whole energy band, this difference in statistics can have a negative impact on the reliability of the results at high energies, as components are dominated by low energy information. An intelligent binning technique that would impose spectral bin sizes containing similar numbers of counts throughout the whole energy band could be a solution. There exists plenty of those, and Figure 10.1 presents an example of that kind of rebinning technique applied on Cassiopeia A's spectrum. This adaptative binning method illustrated uses the Bayesian block method implemented in astropy[1]. It computes the optimal segmentation of data using the algorithm described in Scargle et al. (2013). The main goal of the method is to identify and characterize local variability in time series but the authors state that the method can also be applied to other forms of sequential data. Spectra are sequential data and we decided to explore the use of such a method to carry out an adaptative rebinning to increase the statistics in spectral segments having identical properties. The method performs a segmentation analysis to find change points where the signal's statistical properties are constant in the segments between these points. While this is well suited for time-series of bursting or pulsation sources, the typical X-ray spectrum usually follows a decreasing power-law and hence there are little *flat* spectral region. However between emission lines at 2 keV, 3.5 keV and 4-6 keV a large number of segments with little variation have been identified by the method and binned together while preserving a fine binning in the emission lines which is the kind of binning we were looking for. This method represents a step forward in comparison with the standard binning method used in X-rays which simply tries to reach a given signal-to-noise ratio in each segment disregarding the spectral variability inside the segment. In the future we will try to adapt

[1] https://docs.astropy.org/en/stable/api/astropy.stats.bayesian_blocks.html

the method for power-law decreasing spectra and estimate what the increased statistics gained by rebinning brings in term of sensitivity to GMCA.

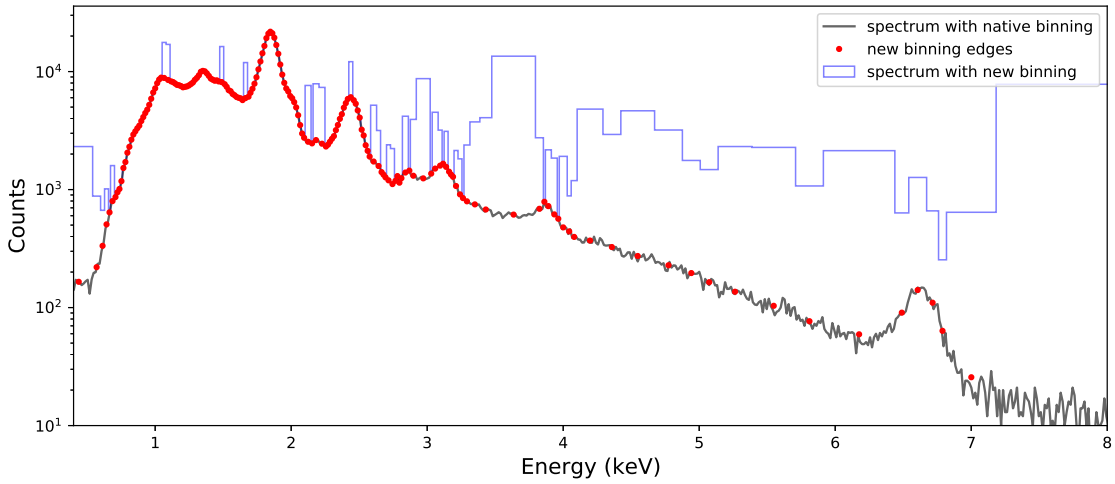

FIGURE 10.1: Example of bayesian block rebinning applied on a 5 ks observation of Cassiopeia A. The contrast between higher and lower energies is of a factor 10 after rebinning, versus almost 1000 before.

Inhomogeneous observations :

We did not encounter this problem when working on Cassiopeia A, but some extended sources do not benefit from homogeneous observations : the exposure time is not the same in every spatial regions of the data sets. An update of pGMCA would be necessary to handle this mosaic of observations properly.

Better error bars :

As stated in Sections 6.5.4 and 6.6 and in the Conclusion, our constrained bootstrap method fails to reproduce a satisfying spread that would allow us to retrieve physically significant error bars. The numerous attempts we made at correcting this issue were not completely fruitless, but we decided to preserve the unbiased nature of our resampling method rather than compromise between bias and variance.

Another approach to develop a new unbiased resampling method would consist in minimizing a cost function evaluating the distance between the distribution law of the resampled data set and that of the original data. The constraint would be more flexible than imposing an histogram, and the spread would possibly be more consistent. However, this idea raises the problem of the means to properly estimate possibly different laws, and how we could modify the resampled data sets to successfully minimize the cost function.

Evolving PSF :

The GMCA and pGMCA algorithms could be of use for other types of data sharing the same (E, x, y) form than X-rays. For example, the gamma-ray observations from *CTA* or *Fermi-LAT* could benefit from these algorithms, but their use would raise the problem of the PSF : almost constant in *Chandra* and *XMM-Newton*, the PSF strongly evolves with energy in *CTA* or *Fermi-LAT*. A new development of the algorithms could help taking this issue into account. This was already achieved in the past for *Planck* data, but not yet implemented for high energy applications.

Other kind of data :

Lastly, we can imagine using GMCA on data sets of a different form than (E, x, y). A first possibility would be to use it on transient sources of the (t, x, y) type, where a time dimension would replace the energy, but

Target name	SNR Type	Chandra	XMM	Synchrotron
Tycho	Ia	1.2 Ms	320 ks	Y
Kepler	Ia	970 ks	too small	Y
SN 1006	Ia	740 ks	700 ks	Y
G1.9+0.3	Ia	1.7 Ms	too small	Y
CasA	CC	2 Ms	too small	Y
RXJ 1713	CC	too large	700 ks	Y
G292.0+1.8	CC	900 ks	150 ks	
G11.2-0.3	CC	480 ks	170 ks	
N132D	CC	900 ks	1.3 Ms	
W49B	CC	270 ks	240 ks	
SgrA East	CC	2.5 Ms	2.5 Ms	

TABLE 10.1: List of archival *Chandra* and *XMM-Newton* public observations of SNRs that have deep exposures. SNRs with bright synchrotron emission are indicated.

the options are numerous. The algorithm only needs " two types of dimensions " to iteratively correct one thanks to the information gained with the other. In X-rays, these dimensions were the spectral E and the spatial (x, y) on which the wavelet transforms were applied, but the same mechanisms could work with only two dimensions or on more than three.

Given the specificities of the data sets we consider, other transforms than the starlets could be of use. For example, we tried applying a wavelet transform on the spectral dimension rather than on the images. The results were not really interesting, but may be more satisfying in a case were the components have more spectral than spatial contrasts. Applying wavelet transforms on both the spectral and the spatial dimensions could also be an option, that has only been briefly explored yet with GMCA.

10.2.2 Applications

Synchrotron rims and Perseus cluster :

As previously stated, further studies could more quantitatively use the beautiful images retrieved by pGMCA in the Chapters 8 and 9 to test the predictions of current models and retrieve physical information about the magnetic field in Cassiopeia A and the formation of filaments in Perseus.

Other objects :

Our method could be applied as such to other X-ray observations. For now, more than ten objects benefit from exposure above 250 ks, making them great candidates to benefit from the capacities of GMCA or pGMCA (see Table 10.1).

Other kinds of data :

Once the necessary updates successfully included in the algorithms, GMCA or pGMCA could be used on other types of data. Promising examples would be gamma-ray data sets or transient sources, for which the time dimension would replace the energy.

Classification :

When applied on a significant number of SNRs, similarities may appear in the components retrieved by GMCA or pGMCA. The same study we made about the asymmetries in Cassiopeia A could be applied on other remnants, possibly leading to a classification regarding the asymmetries similar to that of Lopez et al. (2010).

Classification between a superior number of sources could benefit from our method applied on other data types. For example, Williamson et al. (2019) proposed a classification method based on the light curves using machine learning, and allowing a continuous classification of the supernovae that was less rigid than the historical one. The spectra were not considered in the direct domain, but once transformed with wavelets in order to highlight some specific features. Maybe a blind source separation algorithm such as GMCA could be of use to retrieve characteristics that would be helpful for a classification of this kind ?

Athena :

With future generation instruments with high spectral resolution such as *Athena* and its X-ray Integral Field Unit (X-IFU ; 2.5 eV requirement of energy resolution), it will become impossible, because of the huge number of energy channels, to carry out a pixel by pixel model fitting. Line emission maps will also be difficult to retrieve around narrow energy ranges as the bulk velocity and the turbulence will shift and blur the emission lines, that will then consist of a forest of nearby lines. Therefore, using new techniques such as the GMCA or pGMCA algorithms would be helpful to investigate the spatial distribution of physical components and map physical parameters such as red-shift, temperature, abundances, etc. This kind of new analysis tools will be crucial to maximize the scientific return of *Athena* and fully exploit the capacity of calorimeters cameras in general.

That's all Folks !

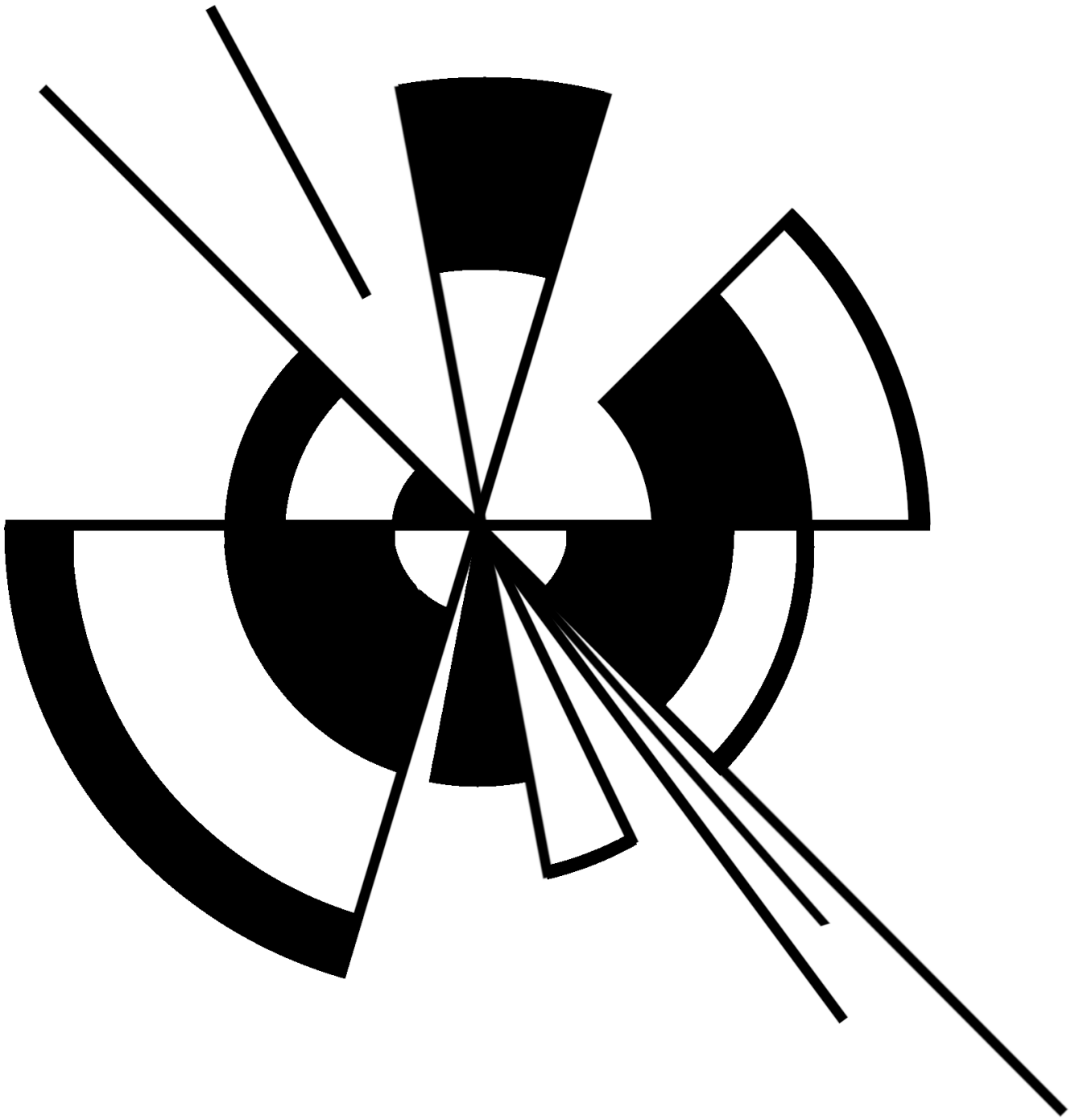

BIBLIOGRAPHY

Araya, M., Lomiashvili, D., Chang, C., Lyutikov, M., & Cui, W. 2010, The Astrophysical Journal, 714, 396

Barret, D., Decourchelle, A., Fabian, A., et al. 2020, Astronomische Nachrichten, 341, 224

Bobin, J., Hamzaoui, I. E., Picquenot, A., & Acero, F. 2020, IEEE Transactions on Image Processing, 29, 9429

Bobin, J., Rapin, J., Larue, A., & Starck, J.-L. 2015, IEEE Transactions on Signal Processing, 63, 1199

Bobin, J., Sureau, F., & Starck, J.-L. 2016, , 591, A50

Bruenn, S. W., Lentz, E. J., Hix, W. R., et al. 2016, , 818, 123

Buote, D. A. & Tsai, J. C. 1995, , 452, 522

Cai, J.-F., Chan, R. H., & Shen, Z. 2008, Applied and Computational Harmonic Analysis, 24, 131 , special Issue on Mathematical Imaging – Part II

Caprioli, D. & Spitkovsky, A. 2014a, , 783, 91

Caprioli, D. & Spitkovsky, A. 2014b, , 794, 46

Comon, P. 1994, Signal Processing, 36, 287 , higher Order Statistics

Comon, P. & Jutten, C. 2010

Conselice, C. J., Gallagher, John S., I., & Wyse, R. F. G. 2001, , 122, 2281

DeLaney, T., Rudnick, L., Stage, M. D., et al. 2010a, , 725, 2038

DeLaney, T., Rudnick, L., Stage, M. D., et al. 2010b, , 725, 2038

Dwarkadas, V. V. 2007, , 667, 226

Efron, B. 1979, Volume 7, Number 1, 1-26

Fabian, A. C., Johnstone, R. M., Sanders, J. S., et al. 2008, , 454, 968

Fabian, A. C., Sanders, J. S., Allen, S. W., et al. 2011, , 418, 2154

Fabian, A. C., Sanders, J. S., Taylor, G. B., et al. 2006, , 366, 417

Fadili, J., Starck, J.-L., & Murtagh, F. 2007a, The Computer Journal, Oxford University Press (UK), pp.64

Fadili, J. M., Starck, J.-L., & Murtagh, F. 2007b, The Computer Journal, 52, 64

Ferrand, G., Warren, D. C., Ono, M., et al. 2019, The Astrophysical Journal, 877, 136

Fesen, R. A., Hammell, M. C., Morse, J., et al. 2006, The Astrophysical Journal, 645, 283

Fesen, R. A., Morse, J. A., Chevalier, R. A., et al. 2001, , 122, 2644

Gessner, A. & Janka, H.-T. 2018, The Astrophysical Journal, 865, 61

Grefenstette, B. W., Fryer, C. L., Harrison, F. A., et al. 2016, The Astrophysical Journal, 834, 19

Grefenstette, B. W., Fryer, C. L., Harrison, F. A., et al. 2017, , 834, 19

Grefenstette, B. W., Harrison, F. A., Boggs, S. E., et al. 2014, , 506, 339

Holland-Ashford, T., Lopez, L. A., & Auchettl, K. 2020, , 889, 144

Hwang, U. & Laming, J. M. 2012, , 746, 130

Janka, H.-T. 2012, Annual Review of Nuclear and Particle Science, 62, 407–451

Janka, H.-T. 2017, , 837, 84

Janka, H.-T., Melson, T., & Summa, A. 2016, Annual Review of Nuclear and Particle Science, 66, 341

Jerkstrand, A., Wongwathanarat, A., Janka, H. T., et al. 2020, arXiv e-prints, arXiv:2003.05156

Lopez, L. A., Ramirez-Ruiz, E., Badenes, C., et al. 2010, in AAS/High Energy Astrophysics Division #11, AAS/High Energy Astrophysics Division, 24.06

Lopez, L. A., Ramirez-Ruiz, E., Badenes, C., et al. 2009, , 706, L106

Lopez, L. A., Ramirez-Ruiz, E., Huppenkothen, D., Badenes, C., & Pooley, D. A. 2011, , 732, 114

Lopez, L. A., Ramirez-Ruiz, E., Pooley, D. A., & Jeltema, T. E. 2009, The Astrophysical Journal, 691, 875

Mallat, S. 2008, A Wavelet Tour of Signal Processing, Third Edition: The Sparse Way, 3rd edn. (USA: Academic Press, Inc.)

Müller, B. 2016, Publications of the Astronomical Society of Australia, 33, e048

Müller, B., Tauris, T. M., Heger, A., et al. 2019, Monthly Notices of the Royal Astronomical Society, 484, 3307–3324

Nesterov, Y. 2003, Universit catholique de Louvain, Center for Operations Research and Econometrics (CORE), CORE Discussion Papers, 103

Orlando, S., Miceli, M., Pumo, M. L., & Bocchino, F. 2016, , 822, 22

Patnaude, D. J. & Fesen, R. A. 2014, The Astrophysical Journal, 789, 138

Peterson, J. R. & Fabian, A. C. 2006, , 427, 1

Picquenot, A., Acero, F., Bobin, J., et al. 2019, , 627, A139

Picquenot, A., Acero, F., Holland-Ashford, T., Lopez, L. A., & Bobin, J. 2021, Astronomy Astrophysics, 646, A82

Poludnenko, A. Y., Gardiner, T. A., & Oran, E. S. 2011, , 107, 054501

Ptuskin, V., Zirakashvili, V., & Seo, E.-S. 2010, , 718, 31

Ressler, S. M., Katsuda, S., Reynolds, S. P., et al. 2014, The Astrophysical Journal, 790, 85

Röpke, F. K. 2017, Combustion in Thermonuclear Supernova Explosions, ed. A. W. Alsabti & P. Murdin (Cham: Springer International Publishing), 1185–1209

Sanders, J. S. & Fabian, A. C. 2007, , 381, 1381

Scargle, J. D., Norris, J. P., Jackson, B., & Chiang, J. 2013, The Astrophysical Journal, 764, 167

Seitenzahl, I. R., Ciaraldi-Schoolmann, F., Röpke, F. K., et al. 2013, , 429, 1156

Shen, L., Xu, Y., & Zeng, X. 2016, Applied and Computational Harmonic Analysis, 41, 26 , sparse Representations with Applications in Imaging Science, Data Analysis and Beyond

Starck, J.-L., Fadili, J., & Murtagh, F. 2007, IEEE Transactions on Image Processing, 16, 297

Starck, J.-L., Murtagh, F., & Fadili, J. 2015, Sparse Image and Signal Processing: Wavelets and Related Geometric Multiscale Analysis, 2nd edn. (Cambridge University Press)

Starck, J.-L., Murtagh, F. D., & Bijaoui, A. 1998, Image Processing and Data Analysis: The Multiscale Approach (Cambridge University Press)

Summa, A., Janka, H.-T., Melson, T., & Marek, A. 2018, , 852, 28

Tatischeff, V. 2003, EAS Publications Series, 7, 79

Thorstensen, J. R., Fesen, R. A., & van den Bergh, S. 2001, , 122, 297

Tran, A., Williams, B. J., Petre, R., Ressler, S. M., & Reynolds, S. P. 2015, The Astrophysical Journal, 812, 101

Walker, S. A., Kosec, P., Fabian, A. C., & Sanders, J. S. 2015, , 453, 2480

Wang, Z., Bovik, A., Sheikh, H., & Simoncelli, E. 2004, IEEE Transactions on Image Processing

Wheeler, J. C. & Harkness, R. P. 1990, Reports on Progress in Physics, 53, 1467

Williamson, M., Modjaz, M., & Bianco, F. B. 2019, , 880, L22

Wongwathanarat, A., Janka, H.-T., & Müller, E. 2013, , 552, A126

Wongwathanarat, A., Janka, H.-T., Müller, E., Pllumbi, E., & Wanajo, S. 2017, , 842, 13

Zel'dovich, Y. B., Librovich, V. B., Makhviladze, G. M., & Sivashinskil, G. I. 1970, Journal of Applied Mechanics and Technical Physics, 11, 264

Zhuravleva, I., Churazov, E., Schekochihin, A. A., et al. 2014, Nature, 515, 85–87

Zibulevsky, M. & Pearlmutter, B. 2001, Neural computation, 13, 863

université PARIS-SACLAY

ÉCOLE DOCTORALE
Physique et ingénierie : électrons, photons, sciences du vivant (EOBE)

Titre: Introduction et application d'une nouvelle méthode de séparation de source à l'analyse de sources étendues en astronomie X

Mots clés: Vestiges de supernova, algorithme de séparation de source, astronomie en rayons X/gamma, asymétries, synchrotron

Résumé: Certaines sources étendues, telles que les vestiges de supernovae, présentent en rayons X une remarquable diversité de morphologie que les téléscopes de spectro-imagerie actuels parviennent à détecter avec un exceptionnel niveau de précision. Cependant, les outils d'analyse actuellement utilisés dans l'étude des phénomènes astrophysiques à haute énergie peinent à exploiter pleinement le potentiel de ces données : les méthodes d'analyse standard se concentrent sur l'information spectrale sans exploiter la multiplicité des morphologies ni les corrélations existant entre les dimensions spatiales et spectrales ; pour cette raison, leurs capacités sont souvent limitées, et les mesures de paramètres physiques peuvent être largement contaminées par d'autres composantes. Dans cette thèse, nous explorerons une nouvelle méthode de séparation de source exploitant pleinement les informations spatiales et spectrales contenues dans les données X, et leur corrélation. Nous commencerons par présenter son fonctionnement et les principes mathématiques sur lesquels il repose, puis nous étudierons ses performances sur des modèles de vestiges de supernovae. Nous nous pencherons ensuite sur la vaste question de la quantification des erreurs, domaine encore largement inexploré dans le milieu bouillonnant de l'analyse de données. Enfin, nous appliquerons notre méthode à l'étude de trois problèmes physiques : les asymétries dans la distribution des éléments lourds du vestige Cassiopeia A, les structures filamentaires dans l'émission synchrotron du même vestige, et la contrepartie X des structures filamentaires visibles en optique dans l'amas de galaxies Perseus.

Title: Introduction and application of a new blind source separation method for extended sources in X-ray astronomy

Keywords: Supernova remnants, blind source separation method, X-ray/gamma-ray astronomy, asymmetries, synchrotron

Abstract: Some extended sources, among which we find the supernovae remnants, present an outstanding diversity of morphologies that the current generation of spectro-imaging telescopes can detect with an unprecedented level of details. However, the data analysis tools currently in use in the high energy astrophysics community fail to take full advantage of these data : most of them only focus on the spectral information without using the many spatial specificities or the correlation between the spectral and spatial dimensions. For that reason, the physical parameters that are retrieved are often widely contaminated by other components. In this thesis, we will explore a new blind source separation method exploiting fully both spatial and spectral information with X-ray data, and their correlations. We will begin with an exposition of the mathematical concepts on which the algorithm rely, and particularly on the wavelet transforms. Then, we will benchmark its performances on supernovae remnants models, and we will investigate the vast question of the error bars on non-linear estimators, still largely unanswered yet essential for data analysis and machine learning methods. Finally, we will apply our method to the study of three physical problems : the asymmetries in the heavy elements distribution in the supernova remnant Cassiopeia A, the filamentary structures in the synchrotron of the same remnant and the X-ray counterpart to optical filamentary structures in the Perseus galaxy cluster.

Université Paris-Saclay
Espace Technologique / Immeuble Discovery
Route de l'Orme aux Merisiers RD 128 / 91190 Saint-Aubin, France